EVALUATION OF THE TRANSFERABILITY OF A GENERIC ALGORITHM FOR OBJECT ORIENTED LANDSLIDE MAPPING AND PATTERN ANALYSIS FOR THE 2010 HAITI EARTHQUAKE

TUMUHAIRWE SARAH
March, 2011

SUPERVISORS:
Dr. N. Kerle
Dr. C.J. van Westen

EVALUATION OF THE TRANSFERABILITY OF A GENERIC ALGORITHM FOR OBJECT ORIENTED LANDSLIDE MAPPING AND PATTERN ANALYSIS FOR THE 2010 HAITI EARTHQUAKE

TUMUHAIRWE SARAH
Enschede, the Netherlands, March 2011

Thesis submitted to the Faculty of Geo-Information Science and Earth Observation of the University of Twente in partial fulfilment of the requirements for the degree of Master of Science in Geo-information Science and Earth Observation.
Specialization: Applied Earth Sciences (Geo-Hazards)

SUPERVISORS:
Dr. N. Kerle
Dr. C.J. van Westen

THESIS ASSESSMENT BOARD:
Prof. Dr. V.G. Victor Jetten (Chairman)
Dr. E.A. Addink (External Examiner, Department of Physical Geography, Utrecht University)

ABSTRACT

In a study by Martha et al. [1], the use of a combination of spectral, shape and contextual information for Object-based landslide detection was studied. An algorithm was developed for the Himalayas' Madhyamaheshwar sub-catchment with 5.8 m multispectral data from Resourcesat-1 and a 10m DEM generated from 2.5m Cartosat-1 data. However, it was not clear whether this algorithm was transferable to other data types and in other areas. The aim of this study was to test the transferability of this user-defined algorithm to the Haiti area with different data types and to provide an insight into the distribution and the main causative factors for the 2010 Haiti earthquake-induced landslides. The transferability test was performed on two study sites located along Haiti's Momanche River with data combinations of Geoeye & Aster DEM, Geoeye & Lidar DEM, Google Earth aerial photos & Aster DEM and Google Earth aerial photos & Lidar DEM. Google Earth data was deemed interesting to use because it is free, has no multispectral information, and contains mosaic and compression artefacts. The distribution and main causative factors were determined by Weights of Evidence modelling method.

The adopted algorithm, without modifications did not work efficiently for the Haiti area with Geoeye & Lidar data. It resulted in 7.3% producer and 5.7% consumer accuracies. This was attributed to lack of robustness of this algorithm as all thresholds were user-defined rather than data-driven. The results show, however, that the methodological set up of the adopted algorithm is transferable to other areas and datasets, provided adaptations are made to suit the specific dataset and area. The used slope derivative from lower 30m resolution Aster DEM significantly reduced the consumer accuracy of all the outputs recorded with the lowest accuracy at 45.39%. With single scale user-defined thresholding, Geoeye & Lidar DEM gave the best balance of producer and consumer accuracies of 66.43 and 79.20% for training site and 70.11 and 69.62% for the validation site. Google Earth aerial photo & Lidar DEM on the other hand gave 56.30 and 69.95% producer and consumer accuracies for the training site. This also highlighted the potential of use of Google Earth aerial photos for automated landslide detection. Map outputs from Google Earth aerial photos were characterised by a salt and pepper effect and this was attributed to the high spatial resolution and object size used in the chessboard segmentation. The entire methodology was observed to be irreproducible, laborious, subjective, and time consuming as the selection of object features, parameters and thresholds was based on a trial and error basis. A standardised approach proposed by Martha et al. (in review) [3] that involves segment optimisation by Plateau Objective Function and data-driven thresholding by K-means cluster analysis was adopted for Geoeye & Lidar data. It gave producer and consumer accuracies of 67.63 and 62.99% for training site and 69.16 and 67.97% for the validation site. In comparison to this approach, the user-defined approach gave relatively better consumer accuracies. Landslides dominated in areas within 1km and mostly South rather than North of the Enriquillo Plantain fault, slopes of 30-70^{o} and areas characterised by cracked and porous Middle to Upper Eocene limestone. All other factors considered in the analysis showed no significant contribution to the pattern of the landslides. The output landslide susceptibility map indicates highest susceptibility in the areas surrounding the Enriquillo Plantain fault.

Keywords: Earthquake-induced landslides, Frequency-Area analysis, Pattern analysis, Weights of Evidence modelling, Object oriented analysis, algorithm transferability

ACKNOWLEDGEMENTS

Special thanks to the Lord for leading and protecting me, for the good health and hope in his word that has sustained me.
My sincere gratitude and heartfelt thanks go to ITC UNU-DGIM, for the sponsorship to undertake my M.Sc. here at ITC. Thank you for the provision. I am grateful for without your funding, I would not have undertaken this study.
Special thanks go to my supervisors, Dr. Norman Kerle and Dr. Cees van Westen for the untiring guidance, advise, encouragement, knowledge, and supervision. You were truly my mentors. Thank you.
To my course director Drs. Tom Loran and the entire staff of Applied Earth Sciences Department, thank you for making my study at ITC fruitful. Thank you for the knowledge, direction, listening ear and the willingness to help at all times.
To the PhD students, who have shown interest in this work Mr. André Stumpf, Mr. Tolga Gorum, Mr. Tapas Martha and Ms. Xuanmei Fan, thank you for the individual contributions you made towards the success of this study.
I also take this opportunity to thank Assoc. Prof. Frank Kansiime; the director of the Institute of Environment and Natural Resources, Makerere University (MUIENR) for your timely advice. I am really grateful.
Special thanks to Mr. Mfitumukiza David, Dr. Byamukama Denis and Mr. Natumanya Ezra for your encouragement throughout my study period.
To all my family members, am glad I have people to count on in whatever situation. You are all a true blessing to me.
To my good friends, Ellen, Frieta, Pricilla, John, Julius, Fred, Wycliffe, Paula, Emma, Ofwono, Henry, Susan, Walter, Carol, Zippora thanks for the joy you brought into my life during our short stay together in Enschede. You will forever be loved and remembered.
All my classmates thank you for the laughter, company and help you rendered to me. I will forever remember you. Thank you.
To the ITC Fellowship, thank you for the word of life and encouragement. It was such a wonderful experience fellowshipping with you. May God use you, be with you, keep you and make you multiply in everything.

TABLE OF CONTENTS

LIST OF FIGURES

LIST OF TABLES

LIST OF ABBREVIATIONS AND ACRONYMS

OOA	Object Oriented Analysis
USGS	United States Geological Survey
DEM	Digital Elevation Model
LIDAR	Light Detection and Ranging
ASTER:	Advanced Space borne Thermal Emission Radiometer
SRTM	Shuttle Radar Topography Mission
WoE	Weights of Evidence
UTM	Universal Transverse Mercator
KM	Kilo meters
M^2	Meters squared
MM/Y	Millimetres per year
N	North
NE	North East
E	East
SE	South East
S	South
SW	South West
W	West
NW	North West
N2	North2
NDVI	Normalized Difference Vegetation Index
Max.diff	Maximum Difference
Pdf	Probability Density Function
POF	Plateau Objective Function
ANN	Artificial Neural Networks
GPS	Global Positioning System

1. INTRODUCTION

This chapter describes the general overview of the study. It consists of the background of the study where a description of the Haiti earthquake, earthquake-induced landslides and the adopted algorithm used in this study is given. It further explains the source of motivation to do this study, the problem to be addressed and specifies the objectives to be addressed which are further broken down into specific research questions. It highlights the relevance of the study and ends with the description of set up of this entire thesis.

1.1. Background

Landslides are one of the most wide spread natural hazards and have a number of causes and effects. Crustal movements along faults give rise to earthquakes and in turn initiate landslides. Earthquakes are considered one of the major causes of landslides in addition to many other static factors [4-7]. Slope failures can also be attributed to liquefaction which is due to stronger shaking from earthquake amplification [8]. These may cause damage to roads, bridges or houses if they occur rapidly. They can even lead to loss of life. These movements are classified into slow and fast types, into creep slides and flows [9-10].

The landslides that were induced by the 12th January 2010 earthquake of Haiti were studied in this study. According to USGS (2010), the Haiti earthquake occurred at 21:53:10 UTC, 25km WSW of Port-Au-Prince on a blind thrust fault associated with the Enriquillo Plantain Garden Fault System. This earthquake had a magnitude of Mw 7.0 and a focal depth of 13 km at 18.457°N, 72.533°W. It took place at a plate boundary of the North American and the Caribbean plates. This boundary region is characterised by left-lateral strike slip motion and compression with the Caribbean plate moving eastward relative to the North American plate at approximately 20mm/y slip rate [11].

Mass Movements (MM) during earthquakes poses a serious threat both to humans and their property in most mountainous areas. According to official estimates after the Haiti earthquake, it was estimated that 222,570 people were killed, 300,000 injured, 1.3 million displaced, 97,294 houses destroyed and 188,383 damaged in Port-au-Prince area and in much of southern Haiti [11]. With the focal depth of 13km, this earthquake was classified as a shallow earthquake. In a preliminary study, a total number of 1864 landslides were identified [12].

In the present concept, landslide susceptibility describes how prone an area is to slope failures. A landslide susceptibility map thus depicts areas likely to have landslides in the future by correlating some of the principal factors that contribute to land sliding with the past distribution of slope failures [13]. An earthquake-induced susceptibility map attempts to indicate how an area is susceptible to earthquake-induced landslides. The first step of any landslide susceptibility analysis is the creation of a landslide inventory map showing the locations and outlines of landslides and in the case of more detailed maps, also the classification of landslides types. The second step is the preparation of a landslide susceptibility map [5]. A landslide susceptibility map attempts to reproduce landslide susceptibility for a certain event and has no predictive power to any other possible event in the near future unless this occurs in the same location with the same characteristics.

Due to the rugged terrain in many parts of the world, many areas are inaccessible for detailed data collection. Satellite imagery offers many options for the examination of mass movements in such environments, especially in developing nations in which resources are scarce and levels of environmental information very limited [14].

To create landslide inventory maps, digital stereo image interpretation and Object Oriented Analysis (OOA) can be used. Stereo image interpretation consists of creation of stereograph images using computer systems and specialized software. To be able to view real 3D, specialized glasses are used [15].

Traditionally, recognition and classification of landslides has been done by fieldwork and manual image interpretation. However, in cases of need for quick information for decision making and areas characterized by hilly and mountainous terrain, this tool is limited [1]. Remote sensing technology has proven to be a very handy and the best tool for landslide inventory generation. This technology is developing by the day with increasing image detail [16-17]. This, coupled with increased computer and programming skills and knowledge, has led to the development of new techniques like Object Oriented Analysis (OOA), also known as Object-based Image Analysis (OBIA) or Geographic Object-Based Image Analysis (GEOBIA), which enable faster detection of landslides. It is a semi-automatic way of image interpretation that identifies landslides by use of expert knowledge to develop algorithms based on landslides' unique spectral, spatial, and morphometric properties [1, 18]. Object-oriented methods have become more popular compared to traditional pixel-based methods and are a source of timely information for post disaster decision making.

In a study by Martha et al. [1], the application of shape, spectral and contextual information for landslide detection was studied. The algorithm was tested with 5.8m multispectral data from Resourcesat-1 and a 10m Digital Terrain Model (DTM) generated from 2.5m Cartosat-1 imagery. Initially, segmentation of a multispectral image was done followed by identification of landslide candidates. False positives were then distinguished from real landslides by combining spectral information together with shape and morphometric characteristics. The features identified as real landslides were then classified based on material type and movement as debris slides, debris flows and rock slides, using adjacency and morphometric criteria. Later on, they were classified based on failure mechanism using terrain curvature. This method was tested on a separate catchment in northern India and is said to have had a total of five landslide types detected by this method with 76.4% recognition and 69.1% classification accuracies [1].

In this study, the transferability of this algorithm has been tested on imagery characterized by multispectral, color and higher detailed information. This was to understand the effect of both imagery and Digital Elevation Model (DEM) data characteristics like band information, color and spatial resolution. The Resourcesat-1 multispectral satellite and Cartosat-1 DEM data mentioned were replaced by the Geoeye or Google Earth aerial photos and Lidar or Aster DEM respectively. Google Earth data were considered interesting to use because they are free, lack multispectral information, are easily accessible with a high spatial resolution and are characterized by compression artifacts. It was used to determine its applicability and the effect of presence of color for semi-automated landslide detection.

Creation of efficient and transferable algorithms is often undermined by subjectivity of operators in selection of thresholds, scale factors and variations in sizes of both landslides and their false positives. Martha et al. (in review) [3] proposed a new approach to objectively select thresholds by k-means analysis and identification of different sized objects by multiple scale parameters derived from the spatial autocorrelation and intrasegment variance analysis. This study tested the applicability of this new approach to Haiti for creation of landslide inventories.

Landslide inventories created from stereo image interpretation are often used for validation of the inventories from OOA and in bivariate statistical analysis. Bivariate statistical analysis, deals with the correlation of occurrence of mass movements and one independent variable (causative factor). Each factor map is combined with the landslide distribution map, and weighting values based on landslide densities are calculated for each parameter class [19].

1.2. Problem statement

Landslides are natural hazards that pose a threat to both human beings and their properties. In search of more land for human settlement and agriculture, people have settled in landslide prone areas, exposing themselves to landslide hazards. This has continuously led to deaths and loss of valuable property [20-21]. Beyond the tragic loss of life, important civil infrastructure such as buildings, dams, and bridges may be destroyed and critical lifeline systems such as power grids, water and gas lines interrupted. The Haiti earthquake, for example, affected approximately 15% of the national population and the damage totals were approximately $7.8 billion, which is more than 120% of Haiti's 2009 gross domestic product. In a number of cases, landslides damaged the essential facilities. In some cases, buildings collapsed into drainage channels and blocked them. In other cases, garbage and debris filled the channels [22]. Due to the immense impact of such events, there is a need for knowledge of earthquake and earthquake-induced landslide patterns. Large earthquake events require a critical review of current seismic design guidelines and development of new approaches. The study of past events and characterizing historical events can greatly contribute towards the development of new earthquake resistant design guidelines [6]. As the geological uniformity law states 'the past is a key to the future'.

Except for field surveys and expert-based explanations of why the Haiti earthquake-induced landslides took place where they did, no extensive statistical analysis of the pattern of the Haiti earthquake-induced landslides has been carried out. This information is important for planning, disaster mitigation and reconstruction efforts. It should be put into consideration as a basic tool for land-use planning, especially in mountain areas [19]. To minimize the loss of lives and damage to property, factors causing unstable slope conditions should be understood so that we can determine landslide susceptibility with high accuracy and reliability [23].

Although 50% of Haiti is under agriculture, only 10% is the amount of land that is considered suitable for agriculture. This means that 40% of agriculture occurs in non-recommended areas and these are mainly steep slopes [24]. Cultivation of steep slopes makes the soil more susceptible to landslides because this, in combination with occurrence of an earthquake, leads to an unavoidable occurrence of landslides as it makes the slopes extremely weak [25-26]. Up on occurrence of landslides in such areas OOA, compared to stereo image interpretation, provides a quicker way to map the landslides.

Manual mapping of event-based landslides is time consuming and often labour intensive, requiring a lot of people for quick interpretation. Although collaborative mapping methods such as the ones done for mapping building damage after Haiti are good options, faster mapping methods are needed. A comprehensive algorithm for landslide detection was developed in a study by Martha et al. [1]. However, it was not clear whether this algorithm was easily transferable when different data are used and in a different area. According to Martha et al. [1], the re-quantification of different feature characteristics may be necessary if the algorithm is to be used in a different area and with different data sets. They welcomed testing of the approach with other data types and in other areas. This study adopted the algorithm and tested its transferability by identifying and creating landslide inventories from different data and in a different area of Haiti compared to India where it was created. It highlighted the possibilities, limitations and issues surrounding the transferability of such an algorithm.

Since 2005, Google Earth has provided freely and easily accessible high resolution image data around the globe. The relatively easy accessibility and free cost of Google Earth data usually available after disasters could make the OOA process even faster. It was not clear whether use of free Google Earth data with colour but no multispectral information affects the OOA process in any way. This is important as currently, high resolution, free Google Earth data are usually provided in disaster areas. In Haiti, we also had free Geoeye images. This study tested the applicability of Google Earth airborne data for Object-based landslide detection and identified some of the cons associated with its use.

Elevation information is important for Object-based detection of landslides. It is useful to know the effect of DEM resolution on the OOA process and results. This study also aimed at testing if the use of a Lidar derived DEM would improve OOA based landslide detection compared to Aster DEM.

1.3. Objectives

1.3.1. Overall objective

To evaluate the transferability of a generic algorithm for object oriented landslide mapping and pattern analysis by applying it to the 2010 Haiti earthquake-induced landslides situation.

1.3.2. Specific objective and research questions

1. To generate a landslide inventory map by multi temporal stereo image interpretation and classification of landslides into scarps and bodies, and into the various landslide types
2. To test the transferability of a generic algorithm to Haiti area using comparable high resolution multispectral image data as applied in development of the algorithm
   - To what extent is the unaltered algorithm applicable to Geoeye data?
   - What modifications are necessary for the algorithm to be applicable to Geoeye & Aster data combination?
   - What modifications are necessary for the algorithm to be applicable to Geoeye & Lidar data combination?
   - How accurately transferable is the Geoeye & Lidar data algorithm to the validation site?
   - To what extent are the output inventories from the above combinations accurate?
3. To test the transferability of a generic algorithm to Haiti area using non-multispectral data.
   - What are the modifications necessary for the algorithm to be applicable to Google Earth aerial photo and Aster DEM data combination?
   - What are the modifications necessary for the algorithm to be applicable to Google Earth aerial photo and Lidar DEM data combination?
   - To what extent are the output inventories accurate?
   - How does the color characteristic affect the results?
4. To evaluate the effect of higher resolution Lidar DEM on the transferability of existing algorithms
   - How accurate is the output inventory when the unaltered Geoeye image & Aster DEM algorithm is applied to Geoeye image & Lidar DEM data combination?
   - How accurate is the output inventory when the unaltered Google Earth & Aster DEM algorithm is applied to Google Earth & Lidar DEM data combination?
   - Will the higher resolution Lidar DEM improve on the result?
5. To understand to what extent one can use higher detail of DEM and image, color information and Multispectral and information.
   - Of all the inventories from all data combinations made, which one is better in comparison to one from visual image interpretation and why?
   - What are the disadvantages and advantages of each data combination?
6. To test the applicability of the Plateau Objective Function (POF) and data-driven thresholds for landslide recognition for Geoeye & Lidar DEM data combination
   - Does the new methodology improve the recognition accuracies compared to those previously obtained by a single scale approach?
7. To analyze the pattern of earthquake-induced landslides using the created landslide inventory from stereo image interpretation, seismic and environmental factor maps.
   - How was the landslide distribution immediately after the recent Haiti earthquake?
   - What are the factors responsible for the occurrence of landslides where they did?
   - For this particular event, which areas had low, moderate and high susceptibility to landslides?

- Is the information obtained about landslide causative factors, from susceptibility analysis, useful for improvement of the OOA process?

1.4. Relevance of study

In an event of a disaster, there is often a need for quick supply of information not only for search and rescue but also for damage assessment. In an event where landslide inventories are required, OOA could provide a faster method to produce such information compared to traditional means involving fieldwork and visual image interpretation. A proper understanding of transferability of algorithms is essential as it explores the possibility of making the OOA process faster by making algorithms more adoptable against changes in image characteristics and geographical settings. Presence of efficiently transferable algorithms would hasten information availability for decision making while saving time and resources. It is essential therefore, to understand the possibilities and constraints associated with creation of easily transferable algorithms both in geographical space and with different imagery possible.

The use of high resolution multispectral image data is often associated with many limitations, often related to low coverage, high cost and limited accessibility due to restrictions by the satellite providers. This study investigated the possibility of use of such data for semi-automated landslide detection. This information is helpful as it highlights the pros and cons associated with the use of such data. This study highlights the potential embedded in the use of Google Earth data that needs to be tapped into.

These outputs from this study, pattern analysis in particular, can be used for better decision making regarding disaster mitigation, reconstruction, and proper land use planning in Haiti. Availability of a susceptibility map from this study could enhance the understanding of areas that may be or may not be unstable and thus helpful in proper land use planning and disaster prevention.

1.5. Organization of thesis

This thesis consists of 5 chapters. Chapter one is the introductory chapter which highlights the background of this study, explains why the motivation to do this study, and the current problems to be addressed. It also contains the overall objective, specific objectives and research questions to be solved in order to address the problem. Lastly but not least, it explains the relevance of this study, the structure of this thesis and who benefits from outputs of the study.

Chapter two reviews literature on the major aspects of this study. Here, literature on evolution of techniques for landslide inventory mapping, segmentation and segmentation optimisation for Object-based landslide detection and the steps involved in the OOA methodology adopted for this study is reviewed. A discussion is also made of earthquake-induced landslides, factors causing landslides, Weights of Evidence modelling and landslide susceptibility.

Chapter three describes the methods and materials used in this study. Therein, the study area, data sets, software and methods used for each objective are described. Flow charts are also contained here, which show the procedures followed.

Chapter four is the chapter where the results are presented and discussed. For each research question, results were obtained. They are shown and explained in this chapter.

In chapter five, conclusions and recommendations are made. Also, possible areas for further research and the study limitations experienced in this study are pointed out.

2. LITERATURE REVIEW

The first step before any landslide hazard assessment is the preparation of a landslide inventory showing the spatial distribution of the landsides. This chapter describes the evolution of techniques for landslide inventory mapping, segmentation and segmentation optimisation for Object-based landslide detection. It also discusses previous predictions relating to the Haiti earthquake, earthquake-induced landslides and their possible causative factors, landslide susceptibility analysis methodologies and takes a special emphasis on statistical approach involving Weights of Evidence modelling, a method that was adopted for landslide pattern analysis in this study.

2.1. Landslide inventory mapping

2.1.1. Visual image interpretation

The first step in a landslide hazard and risk assessment is the preparation of a landslide inventory map that provides the spatial distribution of locations of past landslide occurrences. The most common method for preparation of landslide inventories till date is aerial photographic interpretation [27]. This involves visual assessment of stereo analogue aerial photos supplemented with detailed field investigation [28-29]. Landslides are associated with specific signatures in imagery often recognised by the human eye. Visual image interpretation is a cognitive process that involves use of specific landslide characteristics like tone, contrast, size, shape and contextual information like location and direction [30]. Key to landslide monitoring also involves careful interpretation of imagery for features like cracks, discontinuities, slopes and depressions which are typical features associated with slope failures [31]. Monitoring of these is important for predicting possible failure zones.

Even though visual image interpretation is accredited for allowing a higher degree of operator control [32], and is considered a more accurate means of landslide feature recognition compared to automated methods it has also been associated with a number of drawbacks. It is a relatively complex and empirical technique that requires properly defined interpretation criteria, experience, methodology and training [33]. Though attempts have been made to standardise the process of visual image interpretation by introducing clearly defined guidelines which provide a number of landslide diagnostics [34-35], this methodology is still a very subjective method for landslide inventory preparation [32]. This often makes the results controversial [32, 36] as no landslide inventories of the same area from two different interpreters are ever the same. The skill of the interpreter is of utmost importance in order to obtain a complete and reliable inventory that is free of controversy [35, 37]. Experienced interpreters will most likely produce relatively similar inventories. Also, this process is often compromised and made tedious due to the fact that landslides occur individually and need to be collected/identified one at a time [38]. This is time consuming and in cases where quick and timely information is required for decision making, this method is not efficient enough [32]. Lastly but not least, the use of aerial photos is often not ideal as these are usually not available soon after a major triggering event has happened. In areas where regeneration of vegetation is often fast, evidences of landslides are often masked before flights for aerial data collection are planned and implemented. This is made worse due to the fact that planning for such surveys is usually expensive and thus takes time at the expense of obtaining aerial photos that have landslide signatures that are clear enough for visual assessment [39].

The making of a complete inventory both in space and time is essential for obtaining a representative and reliable landslide hazard and risk levels for a particular site of interest [40-42]. For an efficient visual based image interpretation to identify landslides, availability of high to very high resolution imagery is prerequisite and very high resolution imagery like QuickBird, Ikonos, Cartosat-1 and Cartosat-2 have become the best available option right now for this purpose [43-45]. This has been facilitated by the increasing number of operational sensors with stereo capability and providing high spatial resolution imagery of 3m and even better

[46]. Availability of such high resolution sensors with stereoscopic capabilities coupled with advances in digital image analysis techniques have led to the evolution of landslide inventory mapping approaches [47]. Visual interpretation with satellite imagery has facilitated faster revisits with larger areal coverage and higher detail [38]. Whereas detection of landslides from satellite imagery can be done visually, it is not the best and most efficient as discussed above. A number of automated and semi-automated techniques for interpretation of this data have been developed as discussed below.

2.1.2. Pixel-based inventory mapping

More advanced approaches to landslide inventory mapping compared to visual image assessment involve pixel-based methods like supervised and unsupervised classification and change detection with image differencing, rationing, Artificial Neural Networks (ANN) and image fusion.

A number of both supervised and unsupervised techniques for change detection have been proposed by different researchers [48-51]. In comparison to unsupervised techniques, supervised techniques usually require availability of ground-truth information. Thus, because in many cases there is lack of ground-truth information, unsupervised classification is always mandatory as the next available option in many applications [52]. Important to note however is that all change detection methods, despite their differences in algorithms, deal with multi-temporal imagery acquired at different dates and with differences in spatial resolution, view and sun angles, coverage and atmospheric conditions at the time of acquisition [53].

Cheng et al. [53] in their study entitled 'Locating landslides using multi-temporal satellite images' demonstrated that spectral rationing and multi-temporal image differencing techniques could be used to identify fresh, non-vegetated landslides. Also, Nichol and Wong [54] demonstrated that with image fusion techniques on SPOT XS images the methodology was able to detect approximately 70% of landslides in Lantau Island, Hong Kong, including those in forested areas.

Despite the proven applicability of pixel-based landslide inventory mapping in a number of studies, it is associated with a number of shortcomings. Pixel-based classification assigns a class to a pixel depending on where it falls in the spectral feature space, not putting into consideration its spatial relation to its neighbours [55]. It depends entirely on the spectral signature of landslides. However, this information is typically not diagnostic and unique to landslides as other land cover classes, often known as 'false positives' exhibit similar spectral characteristics as landslides [1]. Also, pixel-based methods often result in small sized objects in comparison to those obtained from visual image interpretation [56]. Most products from pixel-based approaches are thus often characterised by effect often known as the 'salt and pepper effect' which limits the usability of such outputs in the field. The outputs are most often hard to validate on ground. However, this problem has been reduced by development of Object-based landslide inventory mapping methods as discussed below.

2.1.3. Object-based inventory mapping

Apart from visual image interpretation, landslide inventory mapping can also be done in a semi-automatic way where expert knowledge is incorporated to create sets of rules using characteristic spectral, spatial and morphometric properties of landslides and their false positives. This is also known as Object-based classification [1]. It can make use of a number of features evident on the landslide areas and their surroundings. These may include disruptions of drainage networks, disturbances and anomalies related to vegetation distribution and slope changes easily recognisable from DEMs [35]. Until recently, pixel-based methods for change detection and classification have been developed and used widely. However, these are beginning to be replaced by Object-based methods. Object-based landslide inventory mapping is considered inherently better suited, as it can address landslides, as what they are (objects and not pixels – that have spectral, spatial and contextual characteristics) [57].

OOA identifies landslides more quickly compared to visual interpretation, and hence has the potential to aid timely risk analysis, disaster management and provision of timely information for informed decision making processes in the immediate aftermath of a disaster [1]. The identification and classification of landslides involves use of expert knowledge developed during the image interpretation process for landslide identification. This imitates the cognitive landslide identification during visual image analysis by an expert [1].
The OOA methodology, which was also adopted for this study, involves 3 steps which are identification of landslide candidates, distinguishing real landslides from false positives and lastly identification and classification of landslide types present.

2.1.4. Segmentation and segmentation optimization procedures

This is the very first step required for landslide identification and classification. Basic processing units in OOA are objects or pixel clusters. To analyze images, processing units that group and demarcate the objects are formed based on a certain criterion of heterogeneity and homogeneity by segmentation. This step is essential as it provides the basic blocks for OOA. Thus one is able to extract the objects of interest in an image [58]. In eCognition software, different algorithms are provided like multiresolution, quadtree and chessboard [1]. These segmentation algorithms are often combined together to provide accurate and realistic outputs. The quality of the segmentation process affects, to a high extent, the quality of landslide recognition and classification.
The application of OOA is often associated with a number of problems. The actual analysis relies on proper image segmentation. However, the subjectivity and trial-and-error nature of the segmentation process has been the subject of years of research [57]. Though eCognition software provides different segmentation algorithm options to choose from, the choice of one suitable algorithm for a good segmentation is always a challenge due to the landslide size variability. Various researchers have proposed a number of approaches through which this process could be optimized by reducing over or under estimation of object boundaries as discussed below.
To efficiently detect landslides using contextual, size, shape, and color and process knowledge has proved to be very challenging in the past. This is because landslides have been detected mainly using size and spectral characteristics, factors which are not unique to landslides. In a study by Martha et al. (in review) [3], a methodology which determines multiscale parameters by a Plateau Objective Function derived from the spatial autocorrelation and intra-segment variance analysis was developed. This allows for differently sized features to be identified thus solving the challenges associated with scale dependency of landslides and their false positives. It also makes easier and quicker, the segmentation process to outline landslides by ensuring an automated selection of parameters. Esch et al. [59] on the other hand proposes an optimization process that iteratively combines a sequence of multiscale segmentation, feature based classification and classification based object refinement by merging or clipping of segments. This procedure was tested and it was concluded that it is an adaptive procedure that can facilitate more accurate and robust image segmentation. It was found to improve the segmentation process by a percentage between 20 and 40. However, it is said to increase the processing time. Also, Dragut et al. [60], developed a procedure for the optimization of scale parameter estimations. The tool is called Estimation of Scale Parameter (ESP) and it works by iteratively generating, in a bottom up approach, image objects at multiscale levels and then calculates the local variance for each scale. The scale levels at which the image can be best segmented are selected, depending on the data and the site specific conditions, by evaluating LV plotted against the corresponding scale. According to Lu et al. (In press) [61], despite trials of various researchers to use OOA for landslide detection, all of their proposed approaches failed to produce accurate event related landslide inventories in situations where pre and post event landslides are co-existing. A new approach was thus developed to facilitate rapid mapping of new landslides by change detection technique. This technique emphasizes semi-automated and rapid landslide analysis with minimum operator involvement and manual analysis steps by utilizing a problem specific scale optimization image segmentation process with automated spectral and texture parameters. It achieved an area extent producer accuracy of 75.9%.

With the above literature on segmentation optimization, it can be concluded that this topic has been and is still an area of possible active research.

In the OOA process, after making the appropriate segmentation, this is followed by classification of the different segments to their respective land cover classes, false positives and landslide identification.

2.1.5. The identification of landslides

Most landslide marks of bare rock and debris after a landslide are very visible in remote sensing imagery. Fresh landslides usually give a bright appearance in the imagery. The changes are usually identified and represented with the Normalized Difference Vegetation Index (NDVI) values. Thus NDVI is a criterion used in identifying candidates for landslide [1]. The lower the NDVI value, the higher the probability of presence of a landslide. A number of previous researchers of pixel-based methods for automatic detection of landslides have used spectral characteristics basing on NDVI and digital value [1, 27, 54, 62-64] for the identification of landslides. This step results into two classifications of landslide and non-landslide areas. However, the landslide areas identified are unrefined as they classify along classes that exhibit the same spectral characteristics as landslides, often referred to as 'false positives'.

2.1.6. Distinguishing real landslides from false positives

This is sometimes very difficult. New landslides often exhibit spectral properties, in imagery, that are almost identical to those of other naturally occurring bodies in the environment, and they also do not have unique shapes. After a landslide has occurred, most of the vegetation may be cleared leaving the landslide with a similar reflectance as other non-landslide areas like water, rivers sand, and bare rock. When the NDVI method is used, false positives are usually taken for landslides for cover on ground with a low NDVI for example water, bare rock, river beds and roads. Depending on the prevailing false positive classes in the study site it is thus necessary to develop an algorithm to distinguish these from real landslides [1, 63].

2.1.7. Identification and classification of landslide types present

Morphology characteristics developed by Varnes and local knowledge are usually used in this process for classifying landslides according to their failure mechanism. Characteristics such as length/width ratio and asymmetry are very useful in the identification and classification of landslides [1, 65]. Table 1 gives an example of a logical understanding of landslide types based on the local knowledge and morphology characteristics. It is based on such logical understanding that algorithms are developed for landslide classification

Landslide type	**Logical criteria**
Shallow translational rock slide	Source area is in rocky land with shallow depth, and relatively narrow and elongated shape.
Translational rock slide	Source area is in rocky land with moderate slope and planar terrain curvature.
Debris slide	Source area is in a weathered zone or thickly covered soil, moderate slope and low length.
Debris flow	Source area is in a weathered zone or thickly covered soil and moderate slope, but has a long run-out zone.
Rotational rock slide	Source area is in rocky land with steep slopes, and terrain curvature is concave upward.

Table 1: Logical classification criteria (adopted from Martha et al. [1])

In this study, landslide inventories for earthquake-induced landslides were prepared by both stereo image interpretation and Object-based landslide mapping method. The inventories made by Object-based methods were to test the transferability of the generic algorithm described above. Their accuracies were tested by the inventory developed from stereo image interpretation. The inventory from stereo image interpretation was also used to analyse the pattern of earthquake-induced landslides triggered by the most recent 2010 Haiti earthquake. Discussed below are the key issues pertaining earthquakes and earthquake-induced landslides, their causative factors, methodologies for landslide susceptibility and Weights of Evidence modelling.

2.2. Earthquakes and earthquake-induced landslides

Crustal earthquakes, whether moderate or strong, are often accompanied by a distinctive pattern of co-seismic geological phenomena. These may range from surface faulting to ground cracks, landslides, liquefaction/compaction, which leaves a permanent mark in the landscape [66]. The Haiti earthquake, which triggered a number of landslides and lead to several deaths, economic losses and displacement of persons, was predicted by a number of studies, two of which are briefly explained below.

In 2002, analysis of GPS data collected from a 35 site network in the Dominican indicated high seismic hazard on a number of faults, Enriquillo fault inclusive. It indicated that the Caribbean Plate is moving east-northeast ward at a rate of 15 to 23mm per year towards the North American Plate. This means that there is an oblique convergence of the two plates [67]. Also, another study suggested that the Enriquillo fault was capable of producing an Mw 7.2 earthquake if the entire elastic strain accumulated since the last major earthquake was released in a single event today [68].

One of the principle causes of earthquake damage is land sliding triggered mainly by earthquakes on very susceptible slopes. Earthquakes with magnitude greater than 6.0 like the Haiti earthquake of 7.0 can generate wide spread sliding [69]. Earthquakes ranging from moderate to large earthquakes cause landslides, a large number of casualties, and large economic losses. These landslides follow a pattern depending on the prevailing environmental factors. They are usually reported around the epicentre area even in distances of tens of kilometres [70]. A large number of Haiti landslides were reported in the mountainous area approximately 10-15km southwest of the epicentre with most of these in cut slopes along the highway [71]. This study investigated the controlling factors behind the occurrence of the 2010 Haiti earthquake-induced landslides.

2.3. Environmental and seismic factors controlling the occurrence of landslides

A number of factors have been pointed out in various studies as causes of landslides. These factors include lithology, slope, tectonic features, drainage, distance to epicentre, distance to fault rupture, distance to highways, and road network, distance to drainage lines, magnitude, focal mechanism, surface rupture, focal depth drainage density, distance to settlement, soil moisture and land cover slide [70, 72-73]. A few of these factors are discussed below.

2.3.1. Earthquake magnitude and depth

Slope failures are a common occurrence in tectonically active areas. The magnitude of an earthquake trigger has a significant influence on the magnitude of landslide events. Strong triggers result into a large number of landslides and vice versa [74]. According to Keefer [75], the minimum magnitude for an earthquake to trigger a landslide is M=4 and landslide area increases with increase in earthquake magnitude. Despite a lot of variability in geological, geophysical (earthquake type and depth) and climatic conditions, Keefer [76] established a reasonably good power-law dependence of the total landslide volume on the earthquake's moment magnitude.

2.3.2. Lithology

Landslide phenomena are highly related to the lithology and weathering properties of the materials present in an area. In a study by Yalcin [19], the degree of weathering of the rocks was determined by using the classification of weathering method suggested by ISRM [77] and the weathering map was produced according to the data obtained. As a result of the analysis performed according to the lithology-weathering degree of different units, it was verified that approximately 95% of the landslides occurred in high degrees and among the completely weathered rocks [19]. The structural geology of an area has a significant influence on occurrence of landslides. Structures such as non-tectonic folds and multiple ridges, formed by mass rock creeps, degrade mountain slopes making them susceptible to failures [78].

2.3.3. Distance from fault lines, hanging wall effect and fault type

Crustal/tectonic movements along faults give rise to earthquakes. These earthquakes in turn initiate landslides. In fact, in addition to various static factors causing landslides, earthquakes are one of the major triggers of landslides [7]. According to Gallousi & Koukouvelas [4], who quantified the geographic evolution of earthquake-induced landslides and their relation to active normal results, large landslides due to earthquakes are strongly related to active faults. They are known to dominate in the hanging walls compared to the footwalls of co-seismic faults [79]. Also, depending on the type of fault present, landslides are known to dominate in thrust region areas with high co-seismic slip rate compared to strike-slip regions [80-81]. The presence of a fault acts both as a conditioning and triggering mechanism for landslides. Long-term dip-slips cumulate displacement along active faults, acts as a conditioning geomorphic process through the creation of steep slopes which are more susceptible to landslides. However, during an earthquake event, landslides are triggered on unstable slopes whether or not they are conditioned. Tectonic deformation induces pervasive fracturing of the rocks, which are prone to fail along such slopes. Fault planes may also act as preferential sliding surfaces for landslides by constraining their geometry and promoting the gravitational failure [82]. There is thus an expected trend of number of landslides decreasing away from the fault. This is due to reduction of the conditioning and triggering effects of the faults away from them.

2.3.4. Land cover/Land use

The amount of vegetation cover present in an area strongly influences the occurrence of landslides. Studies have shown that areas with dense, woody-strongly rooted vegetation are less susceptible to landslides as these help in improving the stability of slopes [83]. Land cover and Land use maps depict the spatial distribution of vegetative and non-vegetative cover, and types of land use practices respectively. Vegetation provides both hydrological and mechanical effects that generally are beneficial to the stability of slopes. In contrast, barren areas and fallow lands destabilize the slopes [84-85]. However, there are many conflicting evidences concerning the effects of vegetation on slope stability. Based on the examination of natural terrain in Lantau Island in Hong Kong, Franks [86] reported that sparsely vegetated slopes are most susceptible to failure [86]. According to Neaupane & Piantanakulchai [87], Nilaweera & Nutalaya [88], put forward the most convincing explanation on the effects of vegetation on landslide susceptibility and stated four factors to be accounted for. The hydrological factors (soil moisture depletion as a result of transpiration) and mechanical factors (root reinforcement) increase the stability of a slope. Surcharge from weight of trees may or may not do so depending upon the steepness of slope and potential failure mode.

NDVI is often used as an indicator of the amount of vegetation cover. The NDVI value of an area denotes the amount of vegetation present. The NDVI value is calculated by the formula $NDVI = (IR - R)/ (IR + R)$. A high NDVI value in an image usually implies presence of dense vegetation. Presence of high amounts of chlorophyll results in a low reflectance in the red band. Bare areas, on the other hand, usually have fewer amounts of chlorophyll and thus a low NDVI in the resultant imagery [89].

2.3.5. Distance from road network

One of the controlling factors of slope stability is the distance from road network. Landslides usually occur along roads and foot trails mainly due to inappropriately cut slopes and drainage from the roads and trails [85, 90]. Roads may act as barriers, net sources, net sinks or corridors for water flow. Depending on their location, they usually serve as origins of landslides [89]. Analyses involving such relationships often calculate susceptibility up to a given distance away from the feature of interest as the features are not expected to have any impact beyond the specified distance. Generally, the number of landslides is expected to reduce as we move farther away from the road network. This is due to the reduced impact of the road farther away from it up to a distance when the road no longer affects the landslide pattern.

2.3.6. Slope angle and aspect

The relation between landslides and slope gradient is affected by the interaction of geology with geographic process shaping the terrain. While steeper slopes provide greater potential energy to induce failure, they are also indicative of higher strength of materials. This trade-off between increased driving force and increased soil strength appears to reduce the importance of slope angle/steepness [91]. The slope aspect or slope direction, on the other hand, has the potential to influence its physical properties and its susceptibility to failure. The process that may be operating include exposure to sunlight, drying winds and rainfall [87].

2.3.7. Drainage and Drainage density

The closeness of the slope to drainage lines is another important factor in terms of stability. Streams may adversely affect stability by eroding the slopes or by saturating the lower part of material until resulting in water level increases [92]. In a study by Yalcin [19], it was discovered that landslides were closely located within the first 150 m buffer zones from streams.

Drainage density is the ratio of the total length of the stream to the area of the drainage basin. The higher the drainage density, the lower the infiltration and the faster the movement of the surface flow. Most infiltration takes place next to the streams on slopes that have a high permeability such as alluvium. The higher the drainage density, the higher the susceptibility to landslides [19].

2.4. Landslide susceptibility analysis

A landslide susceptibility map shows the likelihood that a landslide will occur in an area on the basis of the local terrain conditions [93]. It is a necessary tool for proper planning and selection of sites for agriculture, infrastructure and other human developments [94]. The evaluation of landslide susceptibility can be accomplished using three major techniques: deterministic models, heuristic approach and statistical methods [58, 95]. Deterministic approach often involves large-scale geomechanical computation and is based on stability models. They can be useful for mapping hazard at large scales, for instance for construction purposes. However, deterministic models are disadvantageous in that they are data intensive as they require the availability of detailed geotechnical and groundwater data, and they may lead to oversimplification if such data are only partially available [95]. They are advantageous in that they are white-box models as they depend on stability models [96]. A heuristic method also known as the expert-driven approach, on the other hand, is where an expert in geomorphology or an earth scientist decides on the type and degree of hazard for each area, using either a direct mapping approach where the degree of hazard is mapped directly in the field or indirectly after the fieldwork on the basis of a detailed geomorphological map using site specific knowledge obtained from visual image interpretation or field surveys. For landslide susceptibility analysis, two major inputs are essential, a detailed landslide map and environmental factor maps, where the expert defines the weights of each of the factors [95, 97]. The advantage of this method is that each individual features of interest outlined on the map can be analyzed and evaluated separately, based on its unique set of site specific conditions. It is, however, a more time-consuming method that depends also to a large degree on the expertise of the geomorphologist or earth scientist. Another approach involves bivariate or multivariate statistical analysis by Weights of Evidence where the combination of factors that could have led to landslides in the past are determined statistically and quantitative predictions are made for areas currently free of landslides. The bivariate statistical analysis is based on the comparison between the landslides inventory map as a dependent variable and all the separate input parametric maps. This approach allows calculation of the weight for each input variable [84, 95, 97]. This study involved a bivariate statistical approach to study the spatial relationship between landslides and their causative factors. The resulting model identifies three different levels of susceptibility: low, low to moderate, and moderate to high [98].

2.5. Weights of Evidence modeling

Evidence of past landslides is considered an important and the most direct method for landslide susceptibility analysis. This is based on the premise that an area with past landslides is landslide prone and has a high probability of new landslides. Two inputs are essential inputs when carrying out Weights of Evidence (WoE) modelling and these are the landslide inventories and a factor map [99]. Figure 1 is a schematic representation of the WoE modelling method as is usually set up in a GIS environment.

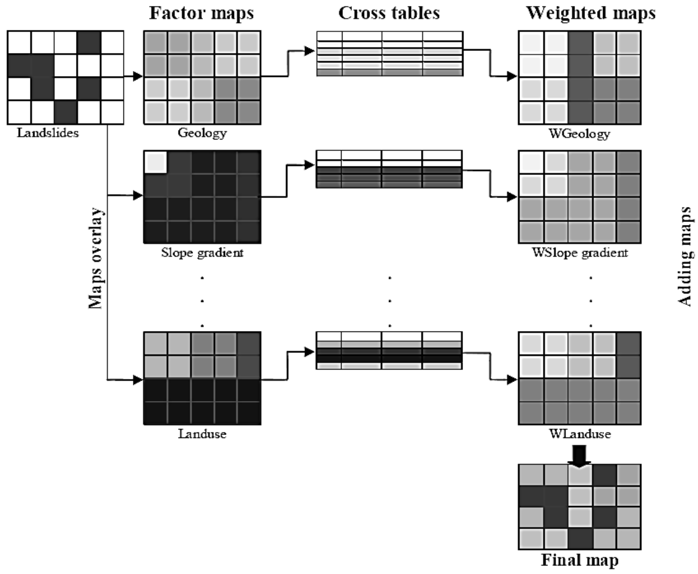

Figure 1: Schematic representation of the WoE modelling method (Adopted from Castellanos et al. [100])

The Weight of Evidence method is used to generate statistically derived weights for all classes in case multiclass maps are used and depending on these weights, the relevant factor maps are then combined into earthquake-induced susceptibility map. Success rates are usually used to decide on the relevance of the factors [101]. This can also be called bivariate statistics. WoE modelling is considered advantageous because it is simple and less time consuming [21]. However, the use of indirect methods such as this has a number of drawbacks these are;

- Simplification: The tendency to simplify the factors that condition landslides, by taking only those that can be relatively easily mapped in an area, such as slope angle or Lithology;
- Generalization: It assumes that landslides happen under the same combination of factors throughout the study area.
- Individual causal factors: The third problem is related to each landslide type having its own set of causal factors, which should be analyzed individually.
- Expert knowledge: There is lack of expert opinion on different landslide types and processes, which is common if these methods are applied by GIS-experts, and not by earth scientists [21, 102].

2.6. Chapter summary

This chapter has reviewed the evolution of methods of preparation of landslide inventories from the traditional visual image interpretation, pixel-based to Object-based methods with an account of some of their shortcomings. It has also discussed earthquakes as triggers to landslides and given an account of some of the major landslide causative factors. It further discussed the various methods available for landslide susceptibility analysis with special emphasis on WoE modelling method, an approach used in this research.

3. MATERIALS AND METHODS

In this chapter, the study areas for this study are briefly described and reasons for choice of the specific sites given. It also highlights the software and major methodologies utilised amongst which are stereo image interpretation, Object-based landslide mapping, accuracy assessment, Weights of Evidence modelling, and frequency-area analysis. The section also contains demonstrations in form of flow charts of how the input datasets were prepared and a work flow for the essential steps in this study.

3.1. Study area

3.1.1. Location map:

Haiti is located on the western third part of the island of Hispaniola. This island is located between the Atlantic Ocean and Caribbean Sea, which it shares with the Dominican Republic. Haiti has an area of 27,750 square kilometres. Its capital and largest city, Port-au-Prince, is in a bay on the country's south western coast. The specific study area for this study is located in the southern part of Haiti. It is located along the Enriquillo fault and down to the south. It cross- cuts the departmental cities of Port au Prince, Jacmel and Leogane. The choice of the study areas was based on a number of considerations amongst which were nearness to the 12th January earthquake epicentre, Enriquillo Plantain Garden Fault System and presence of pre and post disaster imagery. Specifically, for the OOA study, areas with both small and large landslides and coverage of Lidar data along the Enriquillo Plantain Garden Fault System were chosen for both the training and validation sites. The validation study site for OOA had to be with area coverage larger than that of the first OOA training study site.

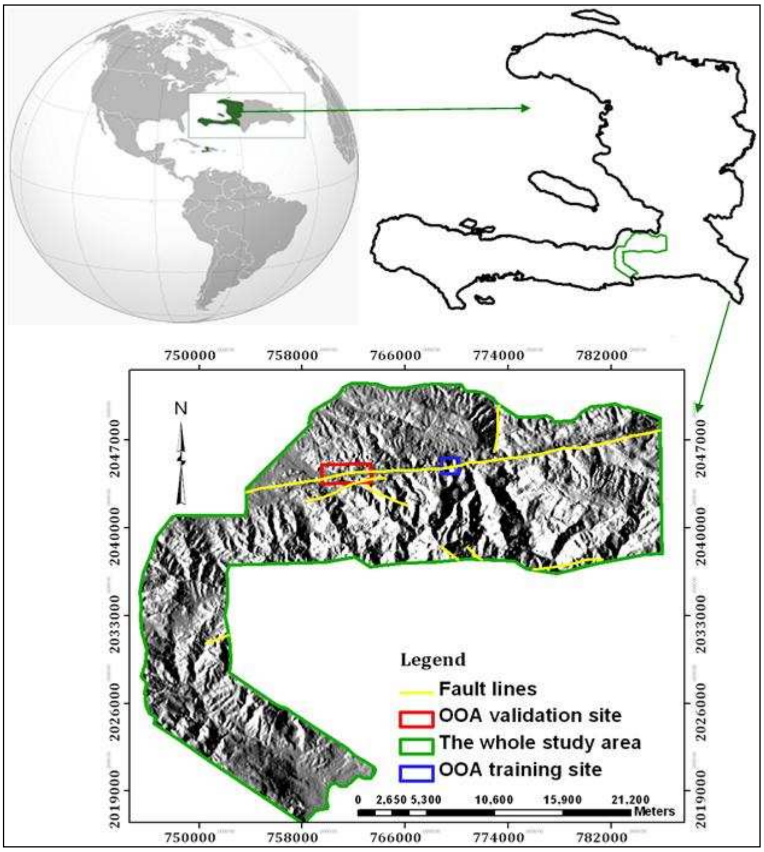

Figure 2: Location map of the study area with a 3D perspective

3.1.2. Economy

According to recent reports, the gross domestic Product for the year 2008 was US $11.59 billion after sustaining 2.3% growth from 2007. 80% of Haitians are said to be living below the poverty level. Haiti is the poorest country in the northern Hemisphere with wide spread corruption. 2/3rds of the Haiti population depends on subsistence agriculture [103]. However, it is also a country endowed with a number of natural resources amongst which are bauxite, copper, calcium carbonate, gold, marble, hydropower, silver, antimony, tin, lignite, limestone, manganese, iron, tungsten, salt, clay, and various building stones [104].

3.1.3. Topography and Geology

Haiti is characterized by rugged topography in the west and central Hispaniola. It is endowed with five mountain ranges which divide the country into three regions. These are the northern, which includes the northern peninsula; central region; and the southern region, which includes the southern peninsula. The backbone of the island of Hispaniola is made up of four major mountain ranges that extend from west to east. The mountains are characterized by limestone although some with volcanic formations mainly within the Massif du Nord. Present, in many parts of Haiti are karstic features like limestone caves, grottoes, and subterranean rivers to mention but a few [104]. The Enriquillo Fault system, where the earthquake occurred, separates basaltic rocks to the south of the fault and sedimentary rocks which consist of sandstone and limestone to the north [71].

3.1.4. Fault system/ Tectonic setting

The Haiti is located in the eastern side of Gonâve microplate. It is bounded by both the North American and Caribbean plates. It is has two strike slips, the Septentrional Fault (SFZ) to the north and The Enriquillo Fault that ends abruptly in south central Hispaniola [103]. The main fault studied in this study is the Enriquillo fault. It is the east-west striking fault that follows the southern peninsula of Haiti into the Enriquillo valley which is located in the Dominican Republic. This fault is estimated to be approximately 250 km long. See Figure 3.

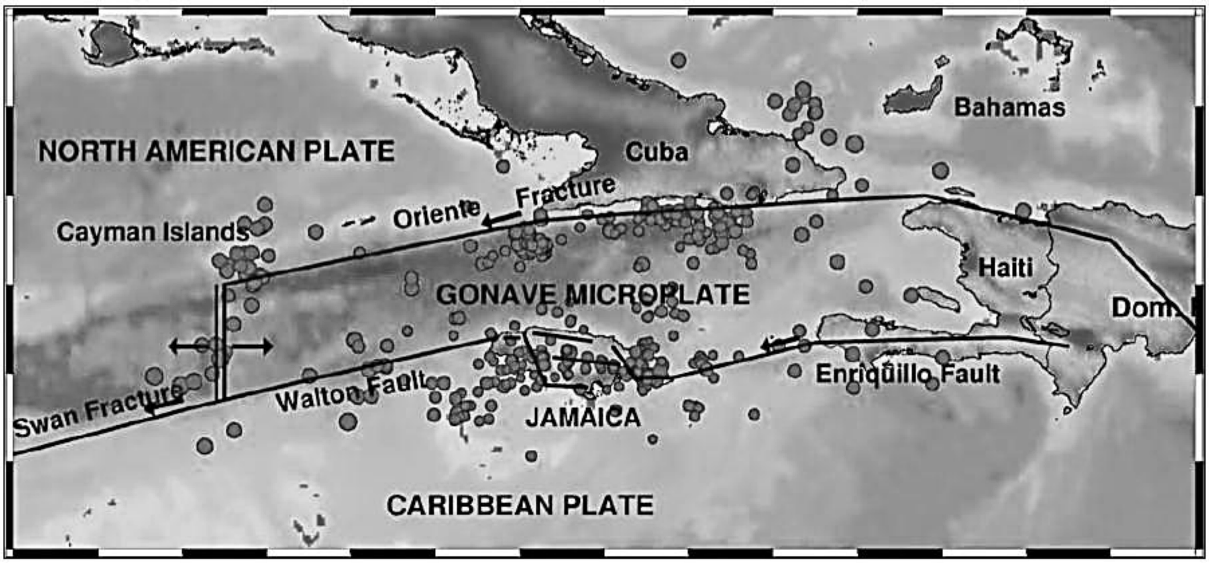

Figure 3: Location of the two major strikes slips faults that go through Haiti

The dots are locations of earthquakes within and around the Gonâve microplate (From Impact Forecasting LLC [103])

3.2. Materials

3.2.1. Data used:

The adopted algorithm was developed with 5.8 m multispectral data from Resourcesat-1 and a 10 m DEM generated from 2.5 m Cartosat-1 image. However, this data is not widely available in areas outside India. This study tested the application of the algorithm to different image data of Geoeye and Google Earth aerial photos in combination with different DEM data of Aster and Lidar. Table 2 is a tabulated summary of attributes of these data and additional data used in susceptibility analysis.

<table>
<tr><th>Data</th><th>Data source</th><th>Format</th><th>Information/attributes contained</th><th>No. of bands</th><th>Resolution (m)</th></tr>
<tr><td>Google Earth aerial photos</td><td>Google Earth</td><td rowspan="9">Raster</td><td>Colour information (RGB)</td><td>3</td><td>1</td></tr>
<tr><td>Geoeye image</td><td>Geoeye</td><td>Multispectral information (RGB & NIR)</td><td>4</td><td>2, 0.5</td></tr>
<tr><td>Aster DEM</td><td>Earth Remote Sensing Data Analysis Centre</td><td>Elevation information</td><td rowspan="13">Not applicable</td><td>30</td></tr>
<tr><td>Lidar DEM</td><td>World bank</td><td>Elevation information</td><td>1</td></tr>
<tr><td>NDVI</td><td rowspan="5">User made</td><td>NDVI information</td><td>2</td></tr>
<tr><td>Flow direction</td><td>Flow direction information</td><td rowspan="4">1, 30</td></tr>
<tr><td>Slope</td><td>Slope information</td></tr>
<tr><td>Aspect</td><td>Aspect information</td></tr>
<tr><td>Hillshade</td><td>Hillshade information</td></tr>
<tr><td>Rivers/Drainage</td><td>USGS/Minustah</td><td rowspan="6">Vector</td><td>Drainage codes, Hydrology(cycle e.g. annual, intermittent fluctuating, non-perennial) and length</td><td rowspan="6">Not applicable</td></tr>
<tr><td>Fault</td><td>USGS/Minustah</td><td>Fault name, description, layer</td></tr>
<tr><td>Roads</td><td>USGS/Minustah</td><td>Road name (type, code, length)</td></tr>
<tr><td>Lithology (1:250,000)</td><td>Adapted from Ellen et al. [2]</td><td>Lithology classes</td></tr>
<tr><td>Landslide inventories</td><td>User made</td><td>Activity, part, type, sub-type, area</td></tr>
<tr><td>Administrative boundaries(Admin2)</td><td>USGS/Minustah</td><td>ID admin 1, Admin1, ID admin 2, Admin 2, length, shape area</td></tr>
</table>

Table 2: List of data used

3.2.2. Comment on importance of DEM resolution and accuracy for this study

In this study, Aster and Lidar DEMs were used to obtain derivatives like slope, flow direction, aspect and hillshade for both landslide susceptibility analysis and Object-based landslide detection. For representative outputs from these analyses on a localised basis using these DEM derivatives, DEM resolution and accuracy are of utmost importance.

An Aster DEM is a very large product that covers very vast expanses of global land. The global Aster DEM is often associated with a number of disadvantages. Though it meets the estimated vertical accuracy of 20m at 95% confidence at a global level, the aster DEM contains a number of artefacts and residual anomalies that affect its overall accuracy. Also, with no inland water mask applied, there is no proper representation of elevation in large inland water bodies. Though with elevation postings about 30m, the detail of topographic expression resolvable for the Aster GDEM is between 100m and 120m [105]. Aster absolute DEMs have an accuracy ranging between ±7 and ±50m whereas the relative DEMs have ±10-30m [106-108].

On the other hand, Fugro EarthData is a company that owns and operates two Lidar systems that capture Lidar data with vertical accuracy of +/-9cm to 40cm and horizontal accuracy of 15-60cm [109]. Lidar DEM data is obtained by aircraft-mounted lasers. The airborne aircraft releases high frequency laser beam towards the earth's surface. The Lidar sensor then records the time lapse between release and return of the beam thus obtaining Lidar data [110]. Lidar data error sources include position errors, range errors and orientation errors. The position errors are due to GPS uncertainty, range errors due to atmospheric distortion whereas orientation errors related to positioning of the aircraft-mounted laser [111]. In a study by Evansa et al. [112], Cartosat-1 absolute DEMs were shown to have vertical accuracies that are virtually similar as those derived from SRTM 30-meter data and are somewhat more accurate than ASTER DEMs. This study tested the effect Lidar and Aster DEMs on Object-based landslide detection.

3.2.3. Software used

A number of software were utilised in this study. Table 3 is a list and brief description of what each of the software was used for.

Software used	Purpose
Ilwis	This was used mainly for stereo image interpretation, pattern and susceptibility analysis. It was also used to create the scripts that were used
Erdas	Erdas was mainly used in image mosaicing, image enhancement and sub setting imagery. It was also used for NDVI indice calculation for the Geoeye image
ArcGIS	Also used for image interpretation; OOA data preparation , visualization of OOA outputs, accuracy assessment, pattern analysis input data preparation and computation of Moran's I index
eCognition	For all work involving OOA, eCognition software was used for data analysis to obtain landslide inventories
Microsoft Excel	This was mainly used to analyze and properly represent pattern analysis results in graphics. It was also used for calculations involving accuracy assessment and Frequency-Area analysis It was also used for computations involving the plateau objective function
Microsoft Word	Used mainly for report preparation and graphical representation preparation.
Microsoft Visual	This was used for preparation of work flow charts and thesis structure graphics.
Endnote	This was used to prepare the list of references used in this study
MATLAB	This was used, in combination with Microsoft excel, for Frequency-Area analysis
CurveExpert 1.4	This was used for plotting some of the Frequency-Area curves
SPSS	This was used for K-means cluster analysis for OOA

Table 3: List of software used

3.3. Methodology

3.3.1. Work Flow Chart

Data analysis was carried out following a number of steps. These are illustrated in the flow chart in Figure 4.

Figure 4: Study Work Flow

Described below is an elaboration of some of the major steps and methodologies highlighted in this flow chart

3.3.2. Stereo visual image interpretation

A landslide inventory shows the spatial distribution of landslides in an area of interest. Depending on the intended use of the inventory, it may be points or polygons. Also, they may be prepared using different methods ranging from historical surveys, field surveys and visual image interpretation to automated or semi-automated methods [37, 39, 96]. The inventory used in this study for susceptibility analysis and validation of OOA outputs was prepared by stereo visual image interpretation.
A Google Earth image was first downloaded with the aid of "gripper.py" tool written in Python software. It downloads, mosaics all tiles and automatically georefences them. With the Google Earth image and the pre-disaster Aster DEM available online, stereo images were created for both anaglyph and stereoscope visualization. Using a screen scope, stereo image interpretation was carried out. Landslide boundaries were then digitized. Also, the elevation exaggeration feature in Google Earth was useful in viewing 3D. 3D visualisation was carried out for identification of landslides, their parts, activity and types.
Landslides can be identified visually from imagery by using a number of morphometric properties and high surface reflectivity [113]. In this study, a number of landslide diagnostics like vegetation clearance, concave-convex and semicircular niches, step-like morphology, hummocky relief, steepening of slopes and interruption of drainage lines were used to identify these landslides. The method used by van Westen et al. [114] was adopted for landslide identification and assignment of attributes. See Table 4 and Table 23 for the checklist and the image characteristics of the various mass movement types used to assign attributes.

Type	Subtype	Activity	Vegetation	Part
Slide Lateral spread Debris Flow Debris avalanche	Rotational Translational Complex Unknown	Stable Relict Reactivated Dormant Abandoned Dormant	Bare Low High/Dense	Scarp Body Transport Unknown

Table 4: Checklist used for characterisation of slope failures
Adapted from van Westen et al. [114] and Soeters and Westen [35]

After digitizing and assigning attributes, the result was a landslide inventory showing landslide extent and attributes landslide ID, type, subtype, activity and landslide parts. This inventory was used in the pattern analysis stage in combination with the factor maps. It was also used for accuracy assessment of OOA products as it is considered an inventory of better quality compared to those obtained (semi) automatically. It was used as the ground-truth data. For a visual impression of how the inventory looks like, see Figure 9.

3.3.3. Brief description of the adopted OOA algorithm

The adopted algorithm for landslide detection was developed in a study within the Indian Himalayas [1]. The entire methodology was divided into 3 steps (See Figure 46). These were steps are described below.

3.3.3.1. Identification of landslide candidates:

This step was aimed at identifying and separating landslide candidates from other areas such as forest land, orchards and crop land. This was achieved by use of the NDVI criterion. Non-landslide areas are usually characterised by relatively high NDVI values compared to possible landslide areas.

3.2.2.2. Separation of landslides from false positives:

With the NDVI cut-off criterion used, objects with similar or lower NDVI values, such as rock outcrops, roads, water bodies and river beds, were misclassified as landslide candidates. This step involved a step by step elimination of these false positives by incorporation of their spectral, morphometric and contextual information (See Figure 5).

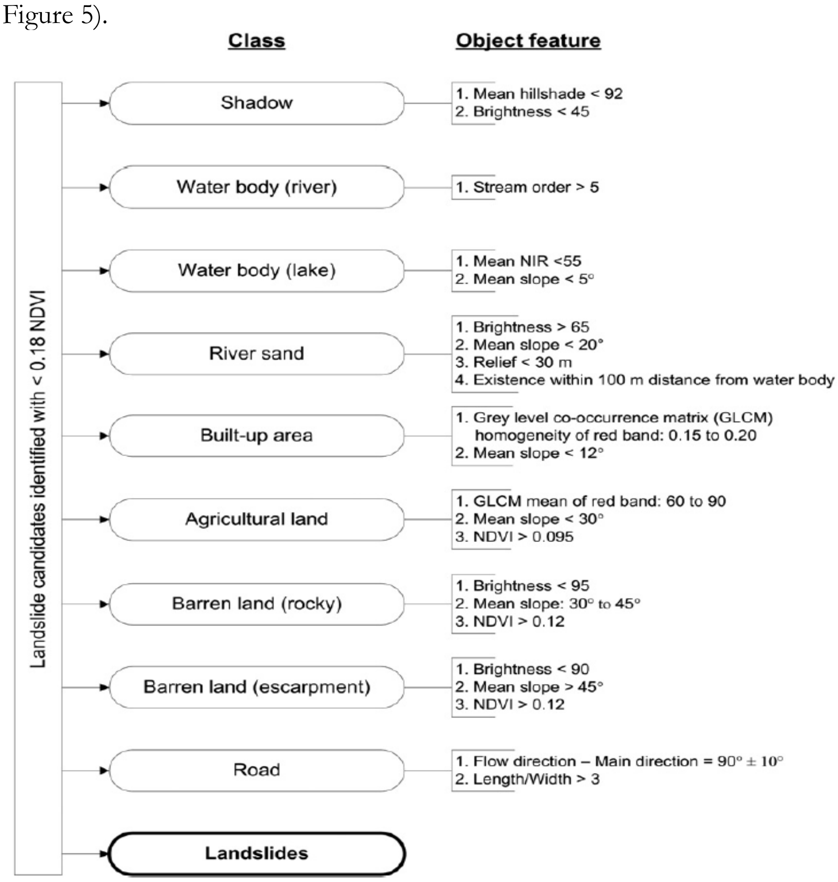

Figure 5: Illustration of the thresholding used by Martha et al. [1]

3.2.2.3. Identification of landslide types

This step involved the use of adjacency condition for source area to classify landslides based on material and types of movement, local field knowledge for the classification of landslides according to their failure mechanism and the length/width ratio and asymmetry for classification of shallow landslides (See Appendix G).

However, it was not clear whether this algorithm is easily transferable when different data are used and in a different area. The unaltered adopted algorithm was first applied to the training site without modifications. Its transferability was later tested for different data combinations. Discussed below are the steps followed to test the transferability of this algorithm in the Haiti area with the different data combinations.

3.3.4. Understanding of the false positive classes in the training site

The first step to creation of an algorithm is to understand the study area. This involved visual image interpretation carried out on Google Earth aerial photos and mapping of the possible false positive classes present in the study site. This was to obtain a general overview and an understanding of the study site and the possible false positives existent in the area for the formulation of the site specific algorithms for the Haiti study site. Outputs from this section are shown under section 4.3.

3.3.5. Input data preparation

All data preparation procedures for OOA analysis were carried out in ArcGIS and ERDAS imagine software. The NDVI map used was created from an orthorectified 2m resolution Geoeye image, acquired on 14th January 2010, in Erdas software. On the other hand, the Aster and Lidar DEMs and their derivatives like hillshade, flow direction, slope curvature, and slope maps were extracted in ArcGIS software using the basic tools available therein. These were imported into eCognition software as image (.img) files and assigned their respective layer aliases. Attempts were made to derive an automatic drainage network for the study areas, however, this was not utilised in the analysis due to limitations as discussed under section 4.5.3.2. Thus, a drainage network was created manually by visual interpretation and imported into eCognition software as a shape file. This was also assigned a layer alias named drainage in eCognition software.

3.3.6. Application of the unchanged algorithm to Haiti training site

The algorithm developed by Martha et al. [1] was first applied on the Haiti training site area data without modifications. It was applied on data combinations of Geoeye image & Aster DEM and Geoeye image & Lidar DEM with one combination at a time. This was to understand to what extent the algorithm developed for a totally different area of the Himalayas could be helpful in identifying landslides in another area, Haiti in this case, and with different data sets. The map results obtained from the unaltered algorithm were used to calculate both producer and consumer accuracies for correct detection of landslide extent by comparison to the landslide inventory from stereo image interpretation for the training site. The results from this section are given and discussed under section 4.4 of this thesis.

3.3.7. Adaptations of the original data set with different data combinations

To understand the adaptability of the adopted algorithm, a number of tests were incorporated for different data combinations. In Table 5 is a summary of the data combinations employed. Important to note is that for each of the data combinations, two data inputs were a pre-requisite, that is, a DEM and an image whether multispectral or non-multispectral. In the adaptation process, efforts were made to maximise the potential of each data combination by exploring all possible options for creating of an accurate and transferable algorithm

	Himalaya's study	**Haiti Data combinations**			
	Resourcesat-1& Cartosat-1	**Geoeye& Aster**	**Google Earth& Aster**	**Google Earth & Lidar**	**Geoeye & Lidar**
Image used	Resourcesat-1	Geoeye	Google Earth Aerial photo	Google Earth Aerial photo	Geoeye
DEM used	Cartosat-1	Aster	Aster	Lidar	Lidar
DEM derivatives	Hillshade Flow direction Slope curvature	hillshade Flow direction slope	hillshade Flow direction slope	hillshade Flow direction slope	hillshade Flow direction slope
Additional data	Drainage NDVI	Drainage NDVI Susceptibility map	Drainage	Drainage	Drainage NDVI
Abbreviations used	**RI&CD**	**GI&AD**	**GE&AD**	**GE&LD**	**GI&LD**

Table 5: Summary of data combination pairs analysed and their respective data inputs

Adaptation of the original data set with different data combinations summarised in Table 5 was achieved by finding the most appropriate object features, parameters and thresholds for each of the false positives existing in the training site. This process resulted in one landslide inventory per combination, whose quality was tested against the inventory from stereo visual image interpretation by calculations of producer and consumer accuracies for correct detection of landslide extent.

3.3.7.1. Application of unaltered GI&AD and GE&AD algorithm on GI&LD and GE&LD data combination respectively

This step involved application of the algorithms developed for Aster DEM on Lidar DEM data. This was mainly for comparison purposes, to test whether this unchanged algorithm works conveniently well with a higher resolution DEM. These results in comparison with those from Geoeye image & Aster DEM combination also highlighted the effect of DEM resolution. The results from this analysis are discussed under section 1.1

3.3.7.2. Application of the algorithm developed for the training site using GI&LD data on the validation site

This step involved the application of the unaltered algorithm developed from Geoeye imagery and Lidar DEM for the training site on the validation site. This was to test the performance of the created algorithm for creation of landslide inventories. It also highlighted possibility of having an easily transferable algorithm for the Haiti area. The comparison of results from the different data combinations gave a broad understanding of the implications of use of different data on both algorithm transferability and accuracy of outputs.

3.3.8. Set up of the methodology in eCognition software

For each of the data combinations discussed above, an eCognition project was set up. The general structure of the project was set up as illustrated in Figure 6. The data specific parameterisation for each of the levels in the process tree is discussed under section 4.5

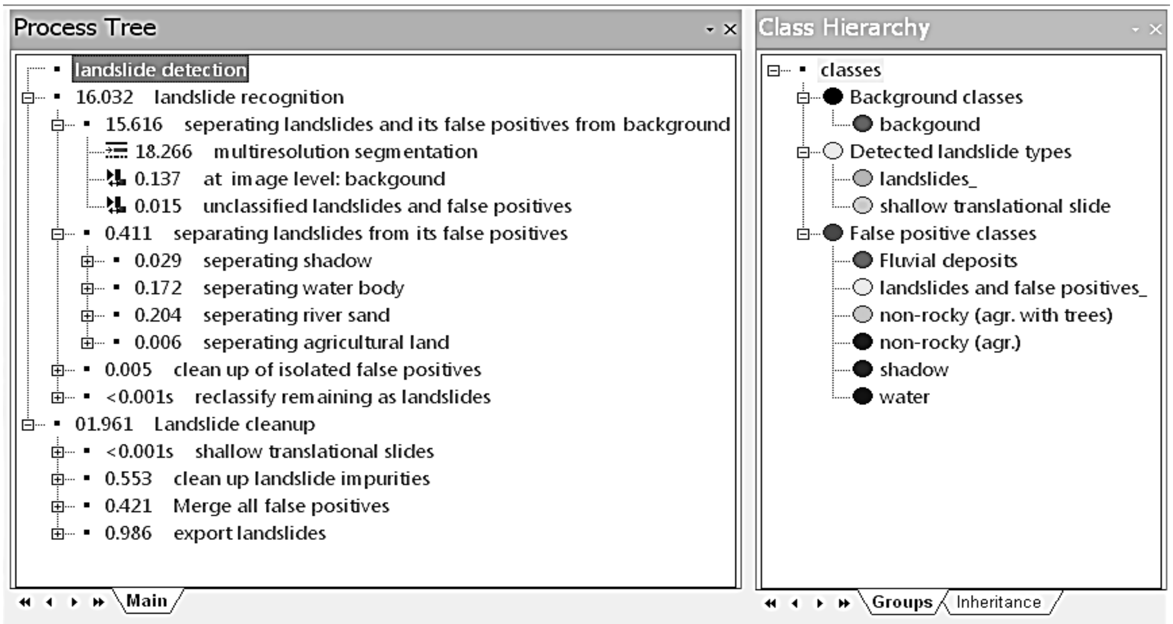

Figure 6: OOA methodology setup in eCognition software (adapted from Martha et al. [1])

3.3.9. The adopted Plateau Objective Function and data-driven thresholding

Due to the subjective, trial and error nature of the selection of parameters coupled with the scale dependency nature of landslides and their false positives, the process of creation of easily transferable algorithms that properly delineate landslide boundaries has certain limitations. This methodology, also known as the Plateau Objective Function (POF), is geared towards ensuring objectivity in the selection of parameters and identification of different sized objects by multiple scale parameters derived from the spatial autocorrelation and intrasegment variance analysis [3]. Optimization of segments was carried out by implementation of the Espindola *et al.*'s [115] objective function, which is a combination of intra-segment variance (v) and Moran's I index (I), for scale factors 5-50, at an increment value of 1, while maintaining constant shape and compactness values for the Geoeye image data. Equations used in the computation are Eq.1 to Eq. 4. Intra-segment variance computations were executed in Microsoft excel whereas Moran's I index was computed in ArcGIS. POF was calculated by combining these two variables after normalisation.

$$v = \frac{\sum_{i=1}^{n} \alpha_i v_i}{\sum_{i=1}^{n} \alpha_i} \qquad (Eq. 1)$$

$$I = \frac{n}{s_o} \times \frac{\sum_{i=1}^{n} \sum_{i=1}^{n} w_{i,j} z_j z_j}{\sum_{i=1}^{n} z_i^2} \qquad (Eq. 2)$$

These two were then normalized using Normalization function in Eq.3

$$F(x) = \frac{x_{max} - x}{x_{max} - x_{min}} \qquad (Eq. 3)$$

A summation of the two normalized values of intra-segment variance (v) and Moran's I index gave the Objective function

$$F(v, I) = F(v) + F(I) \qquad (Eq. 4)$$

α_i	Area of segment *i*
v_i	intra-segment variance of segment *i*
s_o	Aggregate of all spatial weights
$w_{i,j}$	the spatial weight between object *i* and *j*, which is 1 for adjacent regions or 0
n	total number of objects
z_i	is the deviation of the brightness value of object *i* from its mean ($x_i - \bar{x}$),

Table 6: Symbols explained

This step was followed by extraction of landslide candidates by use of the NDVI parameter together with the scale factor corresponding to the first peak of the plateau. A step by step approach was also followed for the classification of false positives. Because sizes of false positives also vary in size/ areal extent, multiple scales were used, these were chosen by visual assessment of the segments created at different scales. To obtain data-driven thresholds for each of them, cluster analysis was carried out in SPSS software. A two-step clustering algorithm was first used to determine the number of existing classes in an objective manner and this was followed by cluster analysis by k-means cluster analysis. The step by step approach and the results obtained from this methodology are discussed under section 4.14.

3.3.10. Accuracy assessment by correct detection of landslide extent

To decide on the usability of a map obtained manually or automatically from remote sensing data for a particular purpose, an accuracy assessment is required [116]. In this study, the landslide inventories from OOA were analyzed for both producer and consumer accuracies in percentage. Without field investigations, the landslide inventory from stereo visual image interpretation was used as the ground-truth data set to validate the OOA outputs. They were based on Eq. 5 & Eq.6.

Given that; **A= Areal coverage of OOA output & B= Areal coverage of Visual inventory**

Producer accuracy is defined as the probability of a reference pixel being rightly classified in a category divided by the total number of pixels in that category from the reference data [116]. This was translated to:
Areal coverage of correctly identified OOA landslides/ Areal coverage of Visual inventory *100
Therefore;

$$Producer\ accuracy = \frac{A \cap B}{B} x100 \qquad (Eq. 5)$$

The consumer accuracy, on the other hand is the total number of correct pixels in the category divided by the total number of pixels classified in that category [116]. This was translated to:
Areal coverage of correctly identified of OOA landslides / Areal coverage of OOA output *100

Therefore;

$$Consumer\ accuracy = \frac{A \cap B}{A} \times 100 \qquad (Eq. 6)$$

The accuracy values obtained were used to make a number of deductions concerning the best data sets combinations, parameters and the transferability of the algorithms. For results obtained from this methodology, see under section 4.6.2

3.3.11. Frequency-Area analysis

To understand the landslide distribution of the landslides identified in the study area after the Haiti Earthquake, a Frequency-Area analysis based on the three-parameter inverse-gamma distribution [33] was carried out. Landslide inventories often give total landslide areas that include both the failure and run-out areas. Though it is most preferable to use landslide volumes and failure areas, these are usually difficult to determine [33]. For each of the landslides identified during stereo image interpretation, the landslide parts originally identified were merged into one to avoid frequency and area misrepresentations. Though areas corrected for topographic gradient would be considered ideal, this is rarely done and the areas used in landslide statistical analysis are usually planar areas [33]. The planar areas of these individual landslides were computed in ArcGIS and their attribute tables accessed in Microsoft Excel. Calculations of frequency, frequency density and probability density were made. The excel results were then used as inputs into Matlab software for computation of the best fit of the three-parameter inverse-gamma distribution to the landslide inventory of the study area. The probability density (pdf) and the inverse-gamma functions used for the analysis are Eq.7 & Eq.8.

$$p(A_L) = \frac{1}{N_{LT}} \times \frac{\delta N_L}{\delta A_L} \qquad Eq.7$$

$$p(A_L; \rho, a, s) = \frac{1}{a\Gamma(\rho)} \left[\frac{a}{A_L - s}\right]^{p+1} \quad exp \ \left[-\frac{a}{A_L - s}\right] \qquad Eq.8$$

Variable	Description
$\boldsymbol{p(A_L)}$	Probability density: the frequency density, *f(A_l)*, divided by the total number of landslides in a substantially complete landslide inventory, N_{LT}
$\boldsymbol{\Gamma(\xi)}$	Gamma function, $\Gamma(\xi) = \int_0^{\infty} \mathrm{y}^{\xi-1} \exp(-\mathrm{y})\,\mathrm{dy}, \xi > 0.$
$\boldsymbol{N_{LT}}$	Total number of landslides in an inventory
$\boldsymbol{A_L}$	Area of landslide
$\boldsymbol{\frac{\delta N_L}{\delta A_L}}$	δN_LIs the number of landslides with areas between A_L and $A_L + \delta A_L$
$\boldsymbol{\rho}$	Parameter primarily controlling power-law decay for medium and large values in three-parameter inverse-gamma probability distribution.
$\boldsymbol{\Gamma(\rho)}$	Is the gamma function of ρ
$\boldsymbol{a}$	Parameter primarily controlling location of maximum probability in three-parameter inverse-gamma probability distribution
s	Parameter primarily controlling exponential rollover for small values in three-parameter inverse-gamma probability distribution

Table 7: Variables used in equations (Adapted from Malamud et al. [33])

PhD researcher Xuanmei Fan (ESA department) made a script for this methodology. It is this script that was used to implement Eq. 7 and Eq. 8 in Matlab software. See section 4.2 for the resultant best fit of the inverse-gamma distribution.

3.3.12. Preparation of landslide causative factor maps for pattern analysis

To determine the causative factors for the Haiti earthquake triggered landslides, a number of factors were studied. These are; lithology, flow direction, distances to roads, slope, aspect, distance to rivers/drainage lines, distance from Enriquillo Plantain fault and elevation. These were individually prepared in ILWIS software into readily usable maps for crossing with the visual image interpretation landslide inventory and further analysis. The factor maps used for analysis are shown in (Appendix B). Figure 7 illustrates the work flow followed to prepare each of these factor maps for analysis.

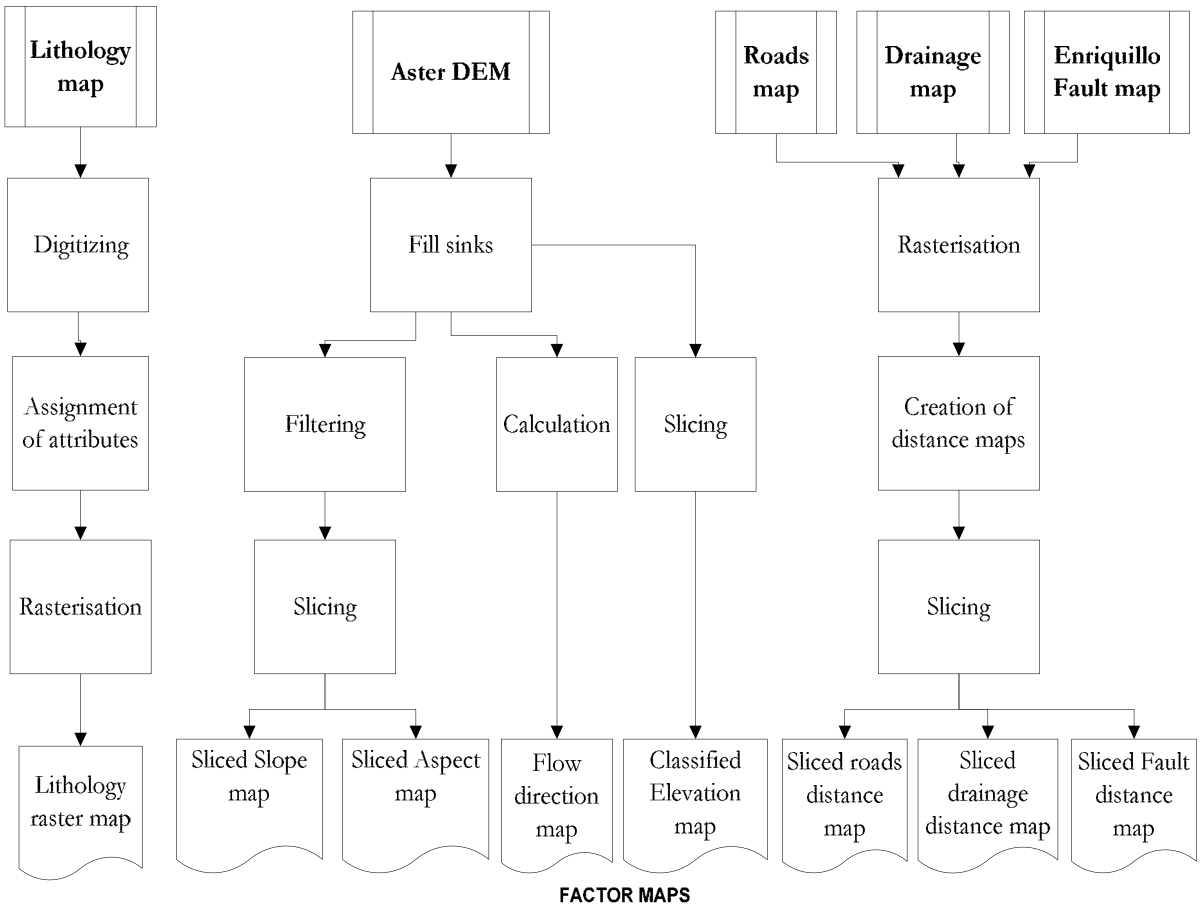

Figure 7: Work flow followed for the preparation of landslide causative factor map for analysis

3.3.13. Landslide pattern and susceptibility analysis

Pattern analysis was carried out by Weights of Evidence modelling (WoE) adopted from Bonham-Carter [117]. Multi-class maps of possible causative factors for landslides were identified, prepared and crossed with the inventory to obtain cross table statistics [114]. Only the scarps of active or reactivated landslides from stereo visual image interpretation were used in the analysis. This is because locations of scarps represent the true location of factors responsible for causing landslides. Use of landslide bodies or run-out parts may not give a true representation of these factors as landslide material, once loose, can move over long distances and thus across factor classes. The output cross table statistics were used to further calculate different calculations among which were; the presence (W+) and absence (W-) weights, the contrast factor and final weights for each class in the multi-class maps multi-class maps. These weights and factors are calculated as shown in the equations Eq. 9, Eq. 10, Eq. 11 and Eq. 12.

$$W_i^+ = log_e \frac{P\{B_i|S\}}{P\{B_i|\bar{S}\}} \qquad (Eq.9)$$

$$W_i^- = log_e \frac{P\{\bar{B}_i|S\}}{P\{\bar{B}_i|\bar{S}\}} \qquad (Eq.10)$$

$$W_{final} = W_{plus} + W_{mintotal} - W_{min} \qquad (Eq. 11)$$

$$C_W = W_{plus} - W_{min} \qquad (Eq. 12)$$

Where;
B_i = Presence of potential landslide conditioning factor
$\overline{B}_i$ = Absence of a potential landslide conditioning factor
S =Presence of a landslide
$\bar{S}$ = Absence of a landslide
C_w = Contrast
W_i^+ is used to indicate the importance of the presence of the factor for the occurrence of landslides. It is positive in the presence of factor for the occurrence of landslides and negative if not favourable.
W_i^- is used to indicate the importance of the absence of the factor for the occurrence of landslides. It is positive if the absence of the factor is favourable for the occurrence of landslides and negative when it is not.
The contrast factor, on the other hand, quantifies the spatial association between a map class and the occurrence of landslides. It is 0 when the landslide map class pattern and landslide pattern overlap only by chance, positive when there is a positive association and negative when there is a negative association between the two patterns.
Success rating was done both manually by typing appropriate expressions and by use of a script. Scripts were made and used to run most of these statistical calculations described above for the individual factor maps (see Appendix C). The results were relations of each factor class within the multi-class maps with landslides. The resultant final weight per factor class depends on the landslide density [96]. They were used to determine the factors, and which classes of factors were determining the pattern thus causing the landslides. Calculations were made for percentages of maps and percentages of landslides. These calculations were used to generate success rate curves for sensitivity analysis of individual causative factors (see Figure 33). Success rate curves were used to determine the main causative factors for landslides.
The susceptibility map was calculated by summing up the causative factors' weight maps to obtain one unclassified weight map. Success rating was performed for this map and the results are illustrated in Figure 34. Depending on the success rate curve, class boundaries were determined and this unclassified weight map was then sliced into 3 classes, Low, Low to Moderate and moderate to High. For the output susceptibility map of the study area see Figure 35.

3.4. Chapter summary

This chapter has described the study area by its location, economy, topography and tectonic setting. It has explained the reasons why the specific study sites were selected which were attributed to data availability and locational preferences. It has given an account of the data and software used and highlighted the importance of DEM accuracy for this study. The chapter has further described the methodology by first presenting the entire methodology with a work flow chart, illustrating the major steps followed. The flow chart is then explained in detail by description of how stereo visual image interpretation was done and the guidelines that were followed. It gives the structure of how Object-based inventory mapping was done, the data combinations that were tested and how accuracy assessment was carried out for the outputs. It also highlights the process followed for segmentation optimization; data-driven thresholding and frequency-area analysis for the landslide inventories. The chapter ends by giving an illustration of the steps followed for creation of input factor data for WoE modelling and the WoE modelling process.

4. RESULTS AND DISCUSSION

Using the methods and materials discussed in chapter 3, analysis was carried out and results were obtained to address the research questions under section 1.3.2. These results are presented and discussed in this chapter. The chapter begins with a statistical summary of the inventories from stereo image interpretation; it is followed by a discussion of the false positives identified in the OOA study sites. It gives an account of application of the adopted algorithm and its adaptation to study site, accuracy assessment of the outputs. It also discusses the effect of DEM resolution and colour, comments on usability of Google Earth aerial photo data, transferability of the generic algorithm and pros and cons observed with the use of the different data combinations. It ends with the results and discussion of the POF methodology and parameterisation by K-means cluster analysis.

4.1. Visual Landslide Inventory map output

With most of the landslides in the epicentre area already mapped by Dr. Cees van Westen and Mr. Tolga Gorum (ESA Department, ITC), further interpretation was done of co-seismic landslides farther away to cover the whole study area for this study. Attributes like landslide ID, type and part were identified. There were significantly visible large numbers of landslides along the Enriquillo–Plantain Garden fault compared to other parts of the study area. Illustrated in Figure 8, Figure 9 and Figure 10 are the visual landslide inventories and a summary of results on the landslide statistics in the study areas.

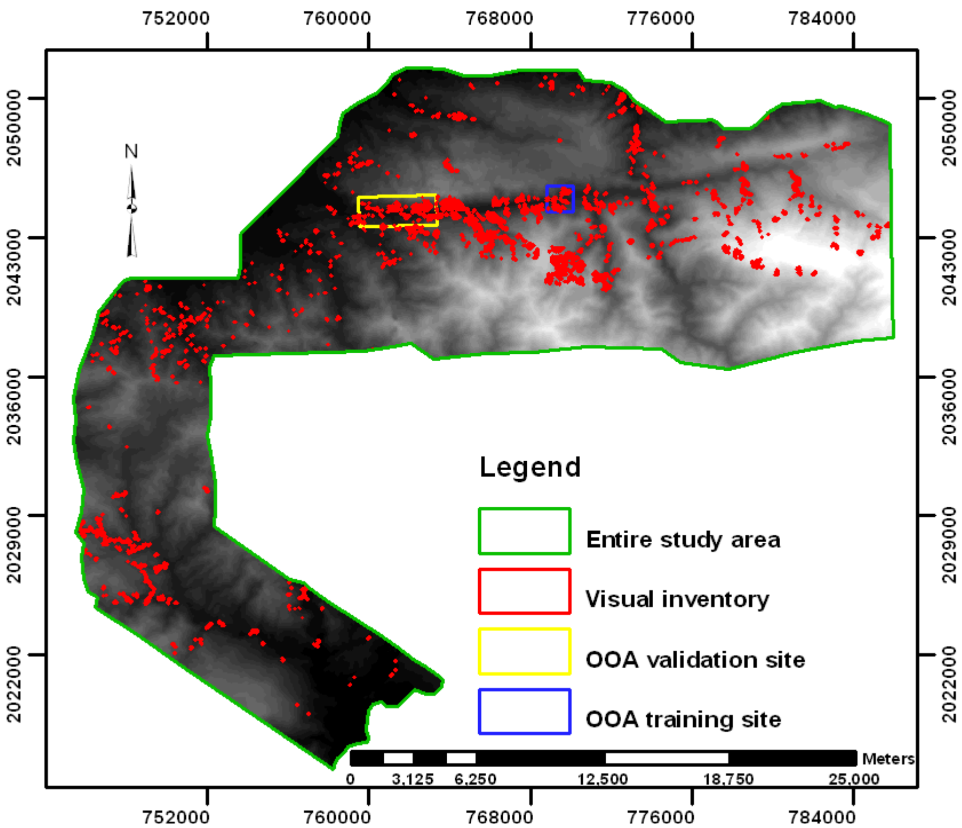

Figure 8: Illustration of the visual inventory used for pattern analysis

The outlines of landslides in the visual inventories for the training and validation sites were mainly used for accuracy assessment of the outputs from the different data combinations whereas scarps for the inventory of the entire study area was used in landslide pattern analysis.

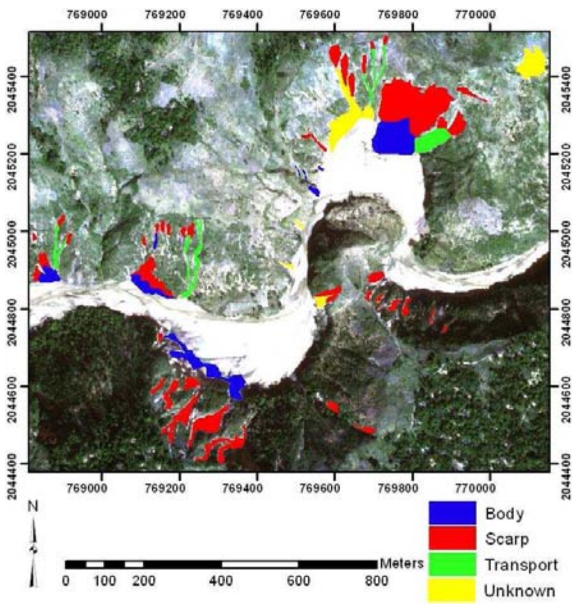

Figure 9: Illustration of Visual inventory map for the training site

Statistics	Entire study area	OOA training site	OOA validation site
Total number of landslides identified	2281	43	195
Total landslide area (m^2)	4600000	90000	310000
Total mapped area (m^2)	585080000	1900000	5660000
Maximum landslide size (m^2)	80000	30000	20000
Landslide density (landslides/m^2)	3.90E-06	2.26E-05	3.45E-05
% of area affected by landslides (%)	0.79	4.76	5.44

Table 8: Statistical results from the visual landslide inventories

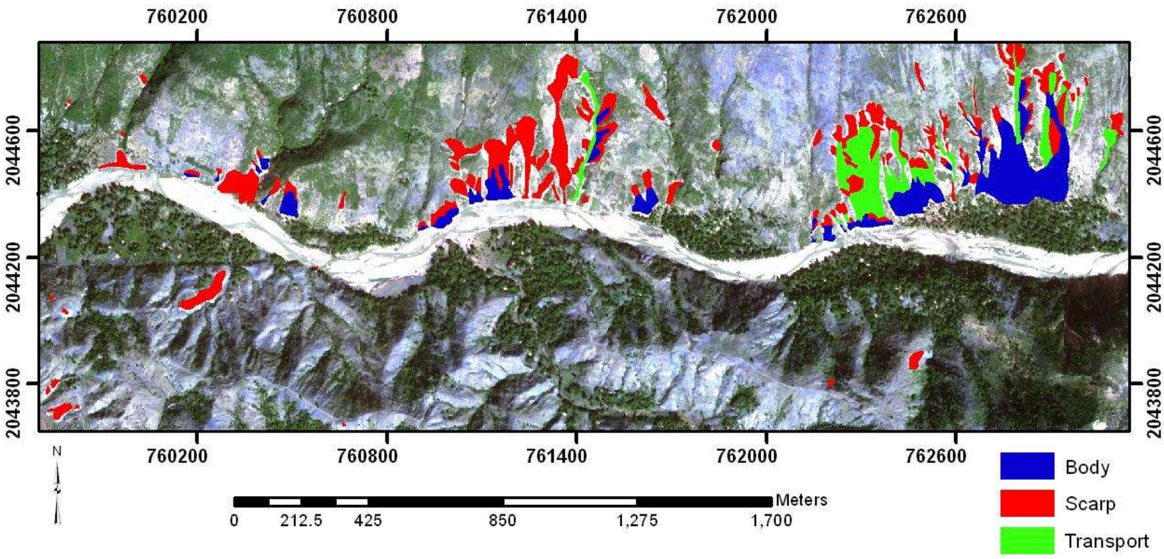

Figure 10: Illustration of visual inventory for the validation site

4.2. Frequency-Area distribution for the landslide inventory

Landslide frequency-area distribution quantifies the number of landslides that occur at different landslide sizes [33]. With the landslide inventory obtained from stereo visual image interpretation for the entire study area, Figure 11 is the Frequency-Area distribution obtained. The best fit of the inverse-Gamma distribution was obtained by taking ρ =0.8839, a =4.51E-04, s =-5.85E-05. It gave an r^2 =0.8316. From Figure 11, the frequency of smaller sized landslides increases as the area size increases until a particular maximum value where landslides are most frequent. After this maximum point, as the landslide area increases, there is a steady reduction in the landslide frequency.

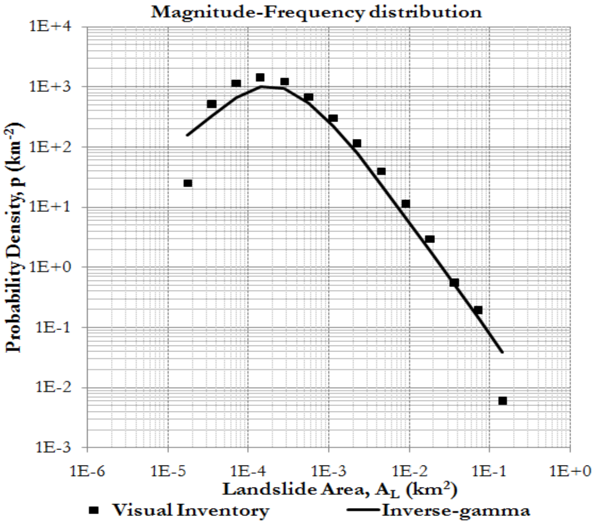

Figure 11: Magnitude-Frequency distribution of the inventory from stereo image interpretation

This trend supports the increasing evidence that asserts that despite the variations in landslide characteristics in terms of types, distributions, patterns and triggers, the frequency of small landslides increases with increases in frequency whereas that of medium to large landslides varies as an inverse power of the landslide area [113, 118-124]

4.3. Understanding the OOA training site

To gain an understanding of the false positive classes that are present in the training study site, a visual image interpretation was carried out on the Google Earth aerial photo for the study site. Figure 12 is the map created for the OOA training site showing the distribution of the identified possible false positive classes.

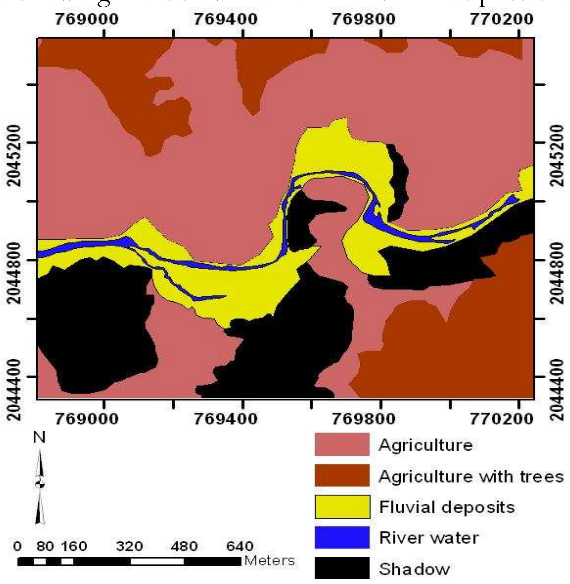

Figure 12: Map showing distribution of the identified possible false positives

The Himalayas' Madhyamaheshwar sub-catchment which was used as a training site for the adopted algorithm consisted of a number of false positive classes. These were shadow, water body, river sand, built-up area, agricultural land, barren land and roads. The Haiti training site, on the other hand comprised of false positive classes of water of the Momanche River, fluvial deposits along this river, agricultural areas and agriculture mixed with trees. Also, a number of areas were characterised by existence in shadow areas (see Figure 12). The agricultural fields, mostly to the north of the study site, were characterised by well developed terraces.

4.4. Application of unaltered algorithm on Haiti training site

To test the transferability of the previously described algorithm (see section 3.3.3) to another area and data set, it was first applied without modification on the Haiti training site using Geoeye-Lidar and Geoeye-Aster data. Figure 13 is the map output (for the un-resampled Geoeye-Lidar data) and accuracies obtained.

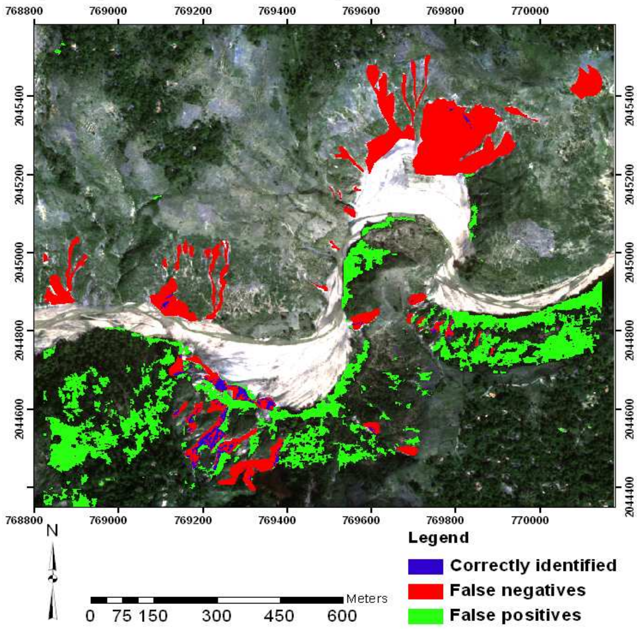

Figure 13: Classified inventory from unmodified algorithm

Data combinations	Resampled Geoeye & Lidar data	Un-resampled Geoeye & Lidar data	Un-resampled Geoeye & Aster data
Landslide area, visually mapped (m²)	88349.1	88349.1	88349.1
Landslide area, OOA based (m²)	107531.2	113051.8	55296.7
Total OOA area correctly identified (m²)	6022	6477.52	1132.9
Producer accuracy (%)	**6.8**	**7.3**	**1.3**
Consumer accuracy (%)	**5.6**	**5.7**	**2.1**

Table 9: Accuracy assessment for inventories from adopted algorithm for different data combinations

From Table 9, resampled means that the data used was resampled to the resolutions used by Martha et al. [1] whereas un-resampled means: the original resolutions of the input data were retained.

From the results in Table 9, the algorithm, without any modifications, can be said to have not worked at all for mapping landslides in the Haiti test area with the Geoeye & Lidar data. All the accuracies obtained are extremely low. Lower than 76.4% recognition accuracy for the extent of landslides which was obtained when the same algorithm was tested on a separate catchment in northern India. This can be attributed to the terrain

differences between the study areas and the fact that the adopted algorithm was developed by a single scale approach with user-defined thresholds. While such an algorithm is advantageous as it ensures flexibility and quasi-cognitive decision making, it is also data and site specific and is not robust enough to accommodate significant variations in site and data properties [3] thus the low accuracies obtained. For example, the absolute hillshade and brightness thresholds used in the algorithm are not directly applicable to the Haiti area and the Geoeye & Lidar data due to differences in data properties like azimuth parameters during data collection, resolution and spectral differences.
To create more accurate landslide inventories for the Haiti area with different data combinations, the originally adopted algorithm had to be adapted.

4.5. Adaptation of algorithms for the different data combinations

To apply the algorithm for Haiti for better landslide detection, the adopted algorithm was altered by changing the object features, parameters and thresholds used though the general structure involving identification of landslides and later sequential elimination of false positives was maintained. Discussed below are the object features, parameters and their thresholds used, explanations why the adaptations were made from the previously used where the algorithm was adopted and the results obtained after the adaptations to the algorithm are applied for the Haiti study areas.

4.5.1. Segmentation

This step involved the demarcation of boundaries of features of interest. The multiresolution segmentation algorithm which requires one to set the shape, compactness, scale parameter and image layer weights was used for this initial segmentation. Selection of an appropriate scale parameter is essential for proper image segmentation and the subsequent classification in Object-based approaches. The accuracy of segmentation decreases with increase in segmentation scales and the negative effects of under-segmentation are usually more pronounced at larger scale parameters [125]. To select the most appropriate scale factor, trials were made using 10, 20, 30 and 50 scale factors for both the Geoeye image and Google Earth aerial photo data. By visual assessment of the delineations, the scale parameter of 10 was selected as it was giving a better demarcation of feature boundaries of both small and larger landslides for both images (compare Figure 14a-d for the Geoeye image). Other parameters set were shape (0.1), compactness (0.5) and image layer weights, assigning a weight of 1 for the RGB layers. A low weight of 0.1 was assigned to shape because landslides exhibit a lot of variability in shape and size. For segmentation, emphasis was thus given to colour.

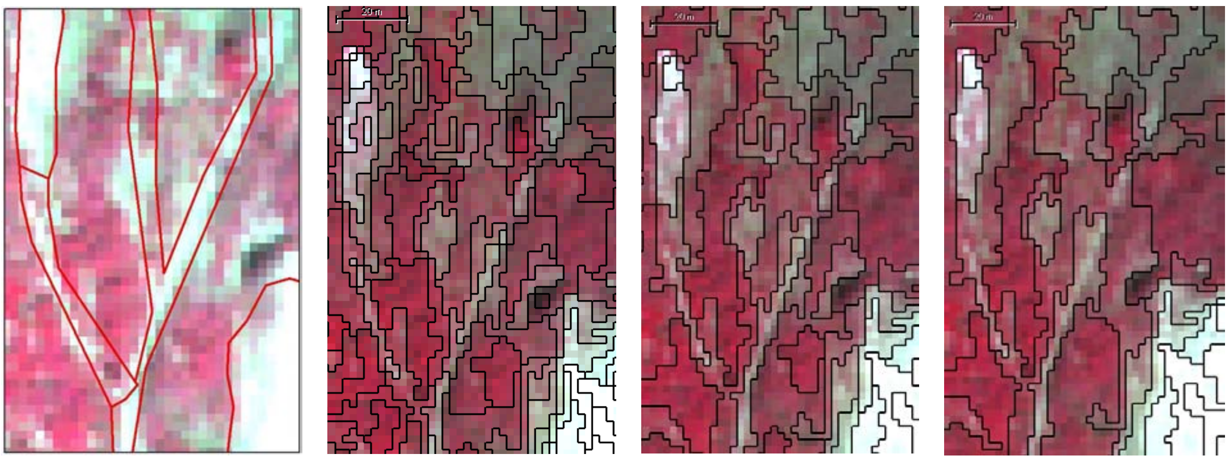

Figure 14: Visual inventory, b) Scale factor 10, c) Scale factor 20 and d) Scale factor 30

4.5.2. Identification of landslide candidates

This step involved the setting of thresholds separating the background from the landslides and their false positives. The parameters used and accompanying thresholds are shown in the Table 10 and explanations below the table.

	Himalaya's area	**Haiti area**			
	Resourcesat_1 & Cartosat_1	**Geoeye & Aster**	**Google & Aster**	**Google & Lidar**	**Geoeye & Lidar**
Background	Mean layer 3 = 0	Mean NDVI≥0.49	Max.diff≥2.5	Max.diff≥2.5	Mean NDVI≥0.49
Landslides and false positives	Mean NDVI ≤0.18	Mean NDVI≤0.49	Max.diff≤2.5	Max.diff≤2.5	Mean NDVI≤0.49

Table 10: Parameters used for identification of landslide candidates

NDVI is a parameter that is sensitive to differences in levels of vegetation cover. This is the main reason why it is usually considered a good and reliable parameter for landslide identification [1]. This was found true in this study too. This parameter was used because for data combinations where the Geoeye image was used to derive NDVI values, areas without vegetation and thus with low NDVI values were coinciding with areas with landslides. This parameter was thus found useful to separate the background from landslides and their false positives. However, for the Google Earth aerial photo & Aster DEM data combination where no NDVI data was available, the maximum difference (max.diff) parameter calculated in eCognition was found useful. Maximum difference is calculated by subtracting the minimum mean value of a segment in the bands available from the maximum value, divided by the brightness of the segment. Landslides and their false positives are characterized by significantly high brightness, low NIR and high red values compared to vegetated areas which usually have low brightness, high NIR and low red values. All these dynamics put into consideration leave a trend where the background areas have a higher maximum difference compared to those of landslides and their false positives. This parameter was thus found useful for Google Earth aerial photo & Aster DEM and Google Earth aerial photo & Lidar DEM data combinations where NDVI data was not available for use. The thresholds used for Haiti and those used in the Himalaya's differ greatly. This can be attributed to differences in background and false positive classes present and the differences in data properties.

4.5.3. Separation of landslides from false positives

Another classification was performed for parts that were neither classified as background and are not real landslides. This step involved the separation of false positives like fluvial deposits, shadow, river water and agricultural land from true landslide candidates one at a time. Using class specific thresholds, each of the false positive class was isolated. The remaining parts of landslides and false positives were then merged using the merge region algorithm. These can be referred to as the un-cleaned up true landslides candidates (un-cleaned up because the classification of parts that were neither classified as false positives and are neither landslide was not sufficient to remove all the impurities). Thus another operation was performed at a later stage. The merged un-cleaned up true landslides candidates were renamed to landslides by using the classification algorithm. The next step was mainly aimed at refining the landslide candidates. The landslides were renamed to shallow translational slides after a chessboard segmentation and setting of restraining parameters for refining the shallow translational slides further. The cleaned up landslide inventory was exported to ArcGIS and an accuracy assessment was carried out. Discussed below are the criteria used for the separation of landslides from each of their false positives.

Even though the NDVI and maximum difference parameters were successful in the classification of the background, a mixed up class of landslides and their false positives was retained. The next step was, thus, aimed at the separation of real landslides from false positives. The false positives in the study area comprised of water, fluvial deposits, agricultural areas, agricultural areas with trees and shadowed areas and these are areas that exhibited similar NDVI and maximum difference range values as for true landslides. The object features, parameters and their thresholds used to classify these false positives are discussed below.

4.5.3.1. Distinguishing of shadow

Table 11 shows the criteria used to classify shadowed areas for the different data combinations tested.

Himalaya's area	**Haiti area**			
Resourcesat_1 & Cartosat_1	**Geoeye & Aster**	**Google & Aster**	**Google & Lidar**	**Geoeye & Lidar**
Mean hillshade < 92 Brightness < 45	Mean brightness≤130	Mean brightness≤90	Mean hillshade≤55	Mean hillshade≤55

Table 11: Criteria used to distinguish and classify shadow

In the study by Martha et al. [1] from which the algorithm was adopted, mean hillshade and brightness parameters were found most suitable to identify and classify shadows. For data combinations where an Aster DEM was used, the hillshade parameter was not found useful because of the coarse nature of the DEM from which the hillshade was created. Mean brightness parameter was thus a better alternative. The hillshade image, usually generated from a DEM, depicts the surface illumination for a given position of sun by calculating the illumination values for each cell of the DEM. In this study, when adaptations were made, parameters like mean layer 4, mean layer 3, mean brightness and mean NDVI were found to be useful for shadow delineation. However, as shown in Table 11, only mean brightness was used. This is because the other parameters especially mean layer 4 and NDVI took along water which also exhibits low values thus resulting in misclassification of not only water, but the fluvial deposits false positive class as its parameters depends on the distance from the river water. The mean brightness of water, though also usually low compared to that for real landslides, was found to be lower for shadowed areas thus allowing use of this parameter for shadow classification. Shadowed areas compared to water class, had lower brightness values. For data combinations where the Lidar DEM was used, the mean hillshade parameter was found useful, taking advantage of the high spatial resolution of the Lidar DEM. The differences in hillshade threshold values for Haiti and Himalaya's can be attributed to differences in DEM elevation and image data properties. The hillshade values were computed using the DEMs and azimuth and altitude parameters of their respective image data for the different combinations.

4.5.3.2. Distinguishing of river water

Table 12 shows the criteria used for classification of river water for the different data combinations

Himalaya's area	**Haiti area**			
Resourcesat_1&Cartosat_1	**Geoeye & Aster**	**Google & Aster**	**Google & Lidar**	**Geoeye & Lidar**
Stream order > 5	ID drainage=5			

Table 12: Criteria used to distinguish and classify water

Logically thinking, river water can easily be classified by use of low NIR values and asymmetry parameters. However, the use of NIR values to classify water was not useful. This was due to presence of shadow, which too, has low NIR values. Manual setting of a threshold to separate these two classes led to some misclassifications. An additional parameter of asymmetry was also found handy for the most parts of the river network; however, some parts of the network were left out. The failure of these two parameters to successfully identify the entire river water can be attributed to ambiguous spectral information present due to the sedimentation process within the river and the surroundings (See Figure 15). The sedimentation process leads to partial absorption of the Electromagnetic radiation (EMR) due to presence of both sediments and big boulders in the water [1]. It was therefore decided that a thematic layer of the perennial Momanche river be used for this purpose.

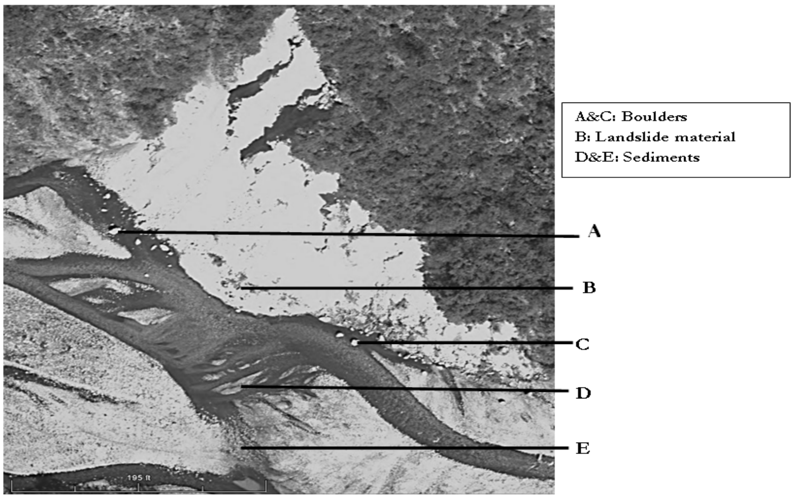

Figure 15: Google Earth Illustration for the sedimentation processes

In the study from which the algorithm was adopted, an automatically derived stream network and ordered using the Stahler method was used. However, in this study, due to the use of a low resolution 30m Aster DEM, the automatically derived and ordered river network was not a good representation of the reality, mainly, in form of estimation of position and extent of the river (see Figure 19), a manually created river drainage network was thus made. It was assigned an ID=5 for the perennial Momanche river network and used in the analysis (see Table 12).

When the 1m Lidar DEM was used to automatically derive and order the stream, a better representation of the river water network was obtained. However, because different segments of the same stream were assigned different stream orders, some with orders similar to those of tributaries and there was no sufficient information to verify actual presence of these streams (see Figure 20), it was decided that the manually created river water network be used. This was tested with different thresholds of 100, 150, 200 and 250, all of which gave stream orders that included tributaries. However, with a detailed local knowledge of the presence of these drainage network distributions of the area, the automatically derived stream network could have been sufficiently useful for the analysis.

4.5.3.3. Distinguishing of fluvial deposits

Table 13 shows the criteria used to classify fluvial deposits.

Himalaya's area	**Haiti area**			
Resourcesat_1& Cartosat_1	**Geoeye & Aster**	**Google & Aster**	**Google & Lidar**	**Geoeye & Lidar**
Brightness>65 Mean slope<20^0 Relief<30m Existence within 100m distance from water	Mean slope≤6^0 Existence within 100m distance from water	Mean slope≤6^0 Existence within 100m distance from water	Mean slope≤12^0 Existence within 120m distance from water	Mean slope≤12^0 Existence within 120m distance from water

Table 13: Criteria used to distinguish and classify fluvial deposits

In this study, two factors were useful for the identification and classification of fluvial deposits. These were mean slope and existence within a particular distance from water/river water class (see Table 13).

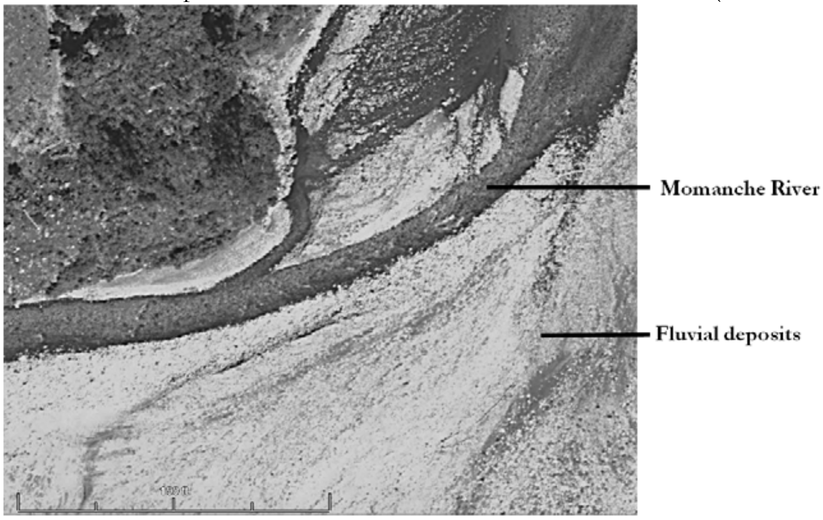

Figure 16: Google Earth illustration of location of fluvial deposits

Fluvial deposits are usually located in low lying areas with low slope values. In the study areas, they also exist in areas nearest to the river water. The differences in threshold values of the three data combinations can be attributed to three possible reasons namely; differences in topography of study sites (the steeper sloped Himalayas compared to Haiti), differences in DEM resolutions and the fact that the used Aster DEM was a pre-disaster DEM whereas the Lidar DEM was a post disaster DEM. Generally, where the Aster DEM was used, the thresholds are lower. This is because increase in threshold values with the Aster DEM lead to over exceedance of the fluvial deposit boundaries because of the already coarse DEM. However, with the Lidar DEM, the values are more precise and thus, though higher, do not overly exceed the class boundaries. This reason also explains the differences in distance values from water.

4.5.3.4. Distinguishing of agricultural areas

The Grey Level Co-occurrence Matrix (GLCM) parameter is a texture measure that calculates the frequency of combination of grey values [1]. In eCognition, these values were calculated using the Haralick's method [126]. The GLCM Mean of red band: 60-90^0 texture parameter was found distinctively useful in the study by Martha et al. [1] because the study area was characterised by terraces distinctively parallel to contours and largely uniform in width pattern.

Himalaya's area	**Haiti area**			
Resourcesat_1 & Cartosat_1	**Geoeye & Aster**	**Google & Aster**	**Google & Lidar**	**Geoeye & Lidar**
GLCM Mean of red band: 60-90^0 Mean slope ≤30^0 NDVI≥0.094	GLCM Homogeneity (quick 8/11) pan (all dir) ≥ 0.24 Mean of blue≤260 Mean of green≤165 Mean of red≤190	max.diff≥2.9	max.diff≥2.9	Mean of blue≤260 Mean of red≤190

Table 14: Criteria used to distinguish agricultural areas

The GLCM homogeneity texture parameter for the Geoeye panchromatic band was useful for classification of agricultural areas for the Haiti study area (See Table 14). This can be attributed to the distinctive pattern created by agricultural terraces present in the study area. From stereo visual image interpretation, the northern part of the study area is characterised by well developed terraces (see Figure 18). Terraces are features, well developed in the Caribbean and Hispaniola in particular [127]. For the Google Earth aerial photo data combinations where panchromatic data was not available, the maximum difference parameter was found useful. Non-landslide areas have higher maximum difference values than landslide areas thus the observed thresholds.

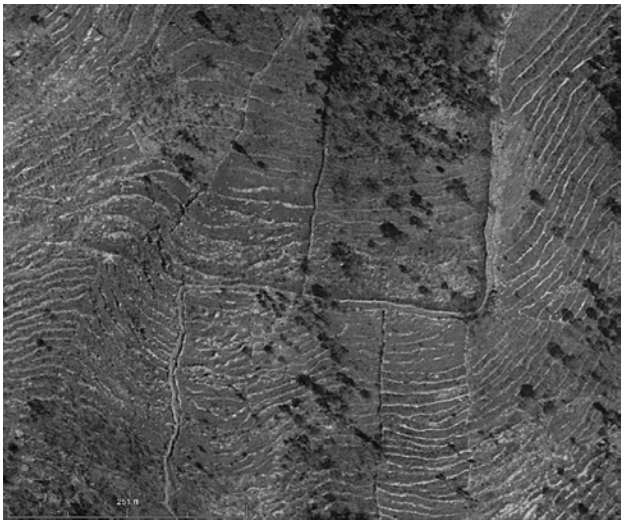

Figure 17: Google Earth illustration of well-developed terraces to the north of the study area

Compared to landslide areas, agricultural areas should be easily distinguishable by their characteristic lower layer values and thresholds in the Geoeye image data. This could account for the usability of mean layer values for the data combination where Geoeye images were used.
For Google Earth aerial photo data and Aster DEM combination, the maximum difference parameter was useful. This is because agricultural areas, compared to landslide areas, have characteristic lower brightness values and significantly lower minimum and maximum layer values. In imagery such areas will usually have high maximum difference values compared to landslide areas.

4.5.3.5. Distinguishing of agricultural areas with trees

This false positive class was mainly comprised of agricultural fields which at the same time were characterised by presence of scattered trees. This class was classified using the criteria shown in Table 15.

Himalaya's area	Haiti area			
Resourcesat_1&Cartosat_1	**Geoeye & Aster**	**Google & Aster**	**Google & Lidar**	**Geoeye & Lidar**
GLCM Mean of red band: 60-90^0 Mean slope ≤30^0 NDVI≥0.094	Max.diff≥2.3 Mean NDVI≥0.39	Max.diff≥3.4	Max.diff≥3.3	Max.diff≥2.3 Mean NDVI≥0.475

Table 15: Criteria used to distinguish agricultural areas with trees

For the Haiti study area, two parameters were used to classify areas characterised by agriculture with trees. These are NDVI and maximum difference. NDVI was found useful because such areas are characterised by high levels of vegetation, compared to landslide areas, thus high NDVI values. The maximum difference parameter was found to be most appropriate to use for all the data combinations. This is because areas characterised by agriculture with trees are characterised by low brightness values thus making them have a distinctively high maximum difference value. Also, as pointed out earlier, landslide areas are characterised by low NDVI values thus the possibility to use NDVI values higher than certain thresholds to classify areas that are agricultural with trees.

4.5.4. Clean up of landslide impurities

After the classification of the most obvious landslides, false positives and landslide impurities, shallow translational slides were retained. However, these landslides still had some impurities (non-landslide areas classified as landslides). These were removed in a two stage process. The removal was done before and after performing chessboard segmentation. The impurities that could not be removed by the criteria used before the segmentation were removed after the chessboard segmentation. A chessboard segmentation was done to obtain tiny single objects that could be reclassified more accurately and thus remove impurities (non-landslide areas).

	Himalaya's	**Haiti area**			
	Resourcesat_ 1&Cartosat_1	**Geoeye & Aster**	**Google & Aster**	**Google & Lidar**	**Geoeye & Lidar**
Before chessboard segmentation	Mean NDVI≥ 0.18	Mean of red≤190 Area≥70 (contained)	Mean brightness≤101 Area≤20 Mean slope≥7^0 (contained)	Mean brightness≤101 Area≤20 Mean slope≥7^0 (contained)	Mean brightness≤139 GLCM Homogeneity (quick 8\11) (all dir.) >= 0.45 Area≥60 (contained) Relief≥35 (contained)
After chessboard segmentation		Mean of blue≤270 Mean of green≤174	Mean blue≤125 Mean of green≤124	Mean blue≤125 Mean green≤124 Mean slope≤5^0	Mean of slope≤7^0 Max. diff. ≥ 2

Table 16: Criteria for landslide impurities removal

Contained means: These were discriminatory criteria specifically for the shallow translational landslides

It is at this stage that other parameters like mean slope, relief and area came into play to clean up impurities (See Table 16). Landslides are commonly found in high relief and slope areas. The area parameter was also found useful in removal of small isolated non-landslide pixels. This was particularly handy for the Google Earth aerial photo data where the outputs are associated with occurrence of many tiny isolated pixels (could be referred to as salt and pepper effect)

The final landslide inventory output maps were then exported as shape files to ArcGIS where an accuracy assessment, based on correct detection of landslide extent, was carried out as will be presented later.

4.6. Map outputs and accuracy assessment

Each of the data combinations resulted into a landslide inventory whose quality was tested against a landslide inventory from visual image interpretation. Presented in sections 4.6.1 and 4.6.2 are the classified inventory map outputs, their accuracy assessment results, and later, a discussion of these results.

4.6.1. Classified landslide inventory map outputs

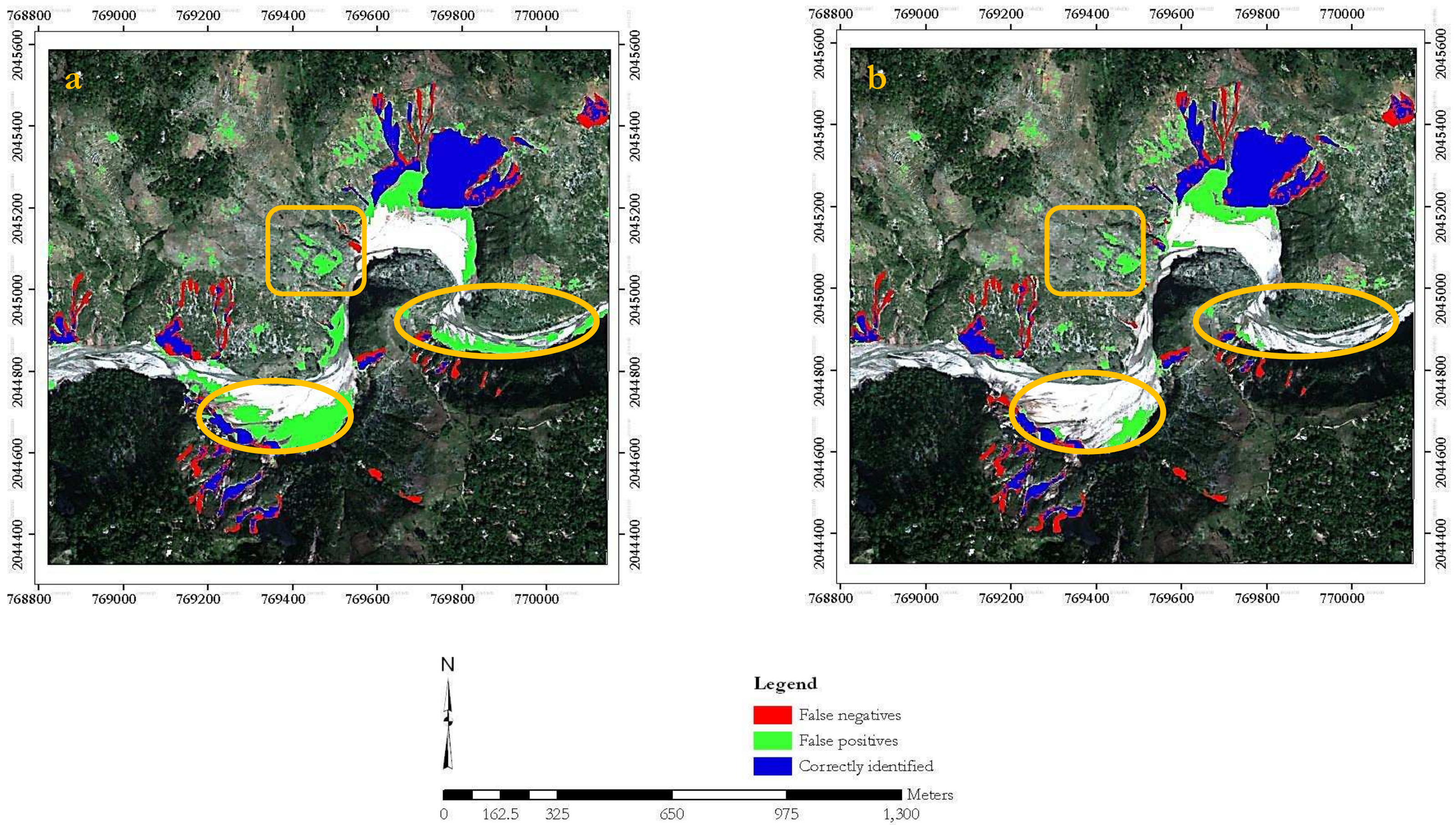

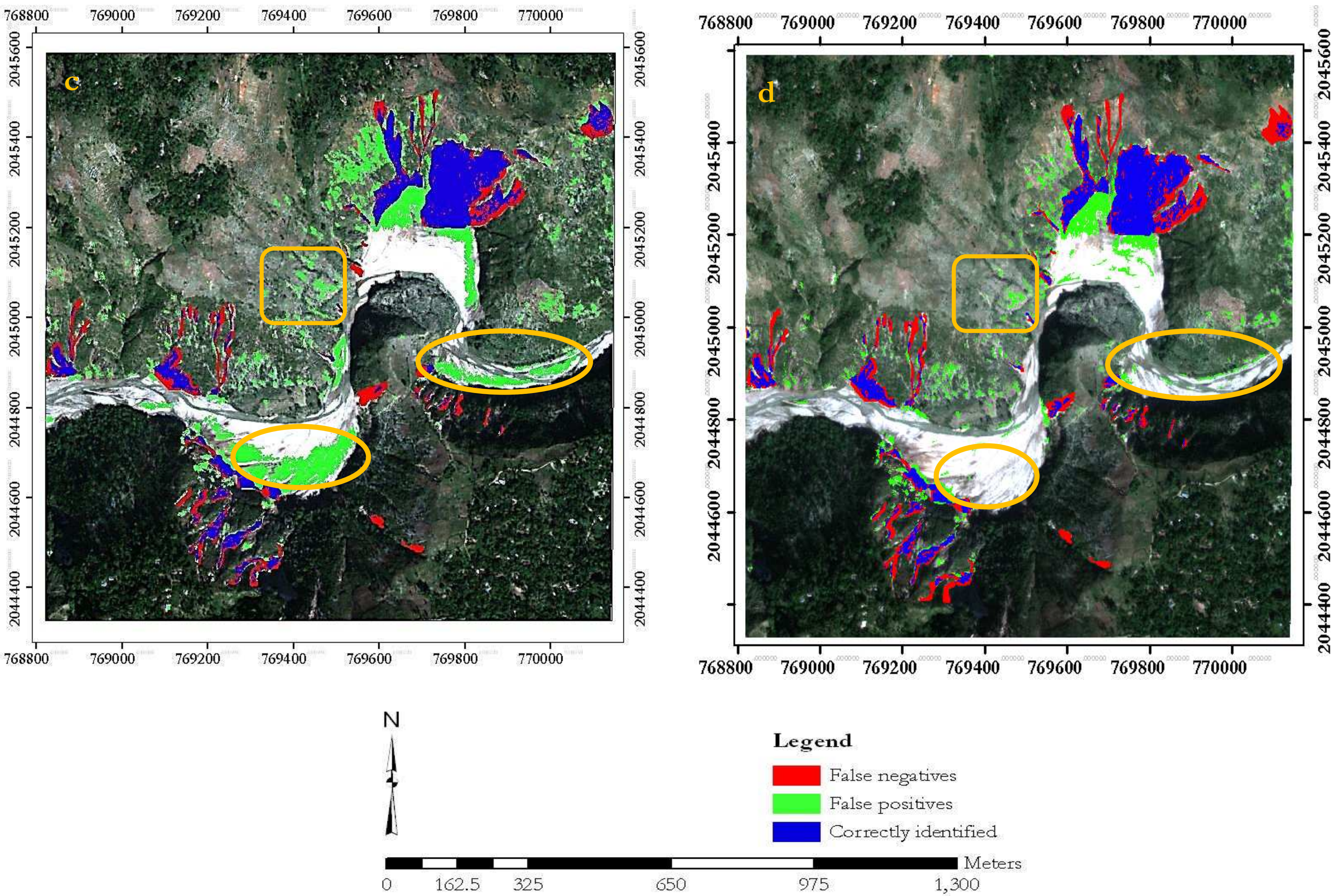
c
d
768800
769000
769200
769400
769600
769800
770000
2044400
2044600
2044800
2045000
2045200
2045400
2045600
N
Legend
False negatives
False positives
Correctly identified
0
162.5
325
650
975
1,300
Meters

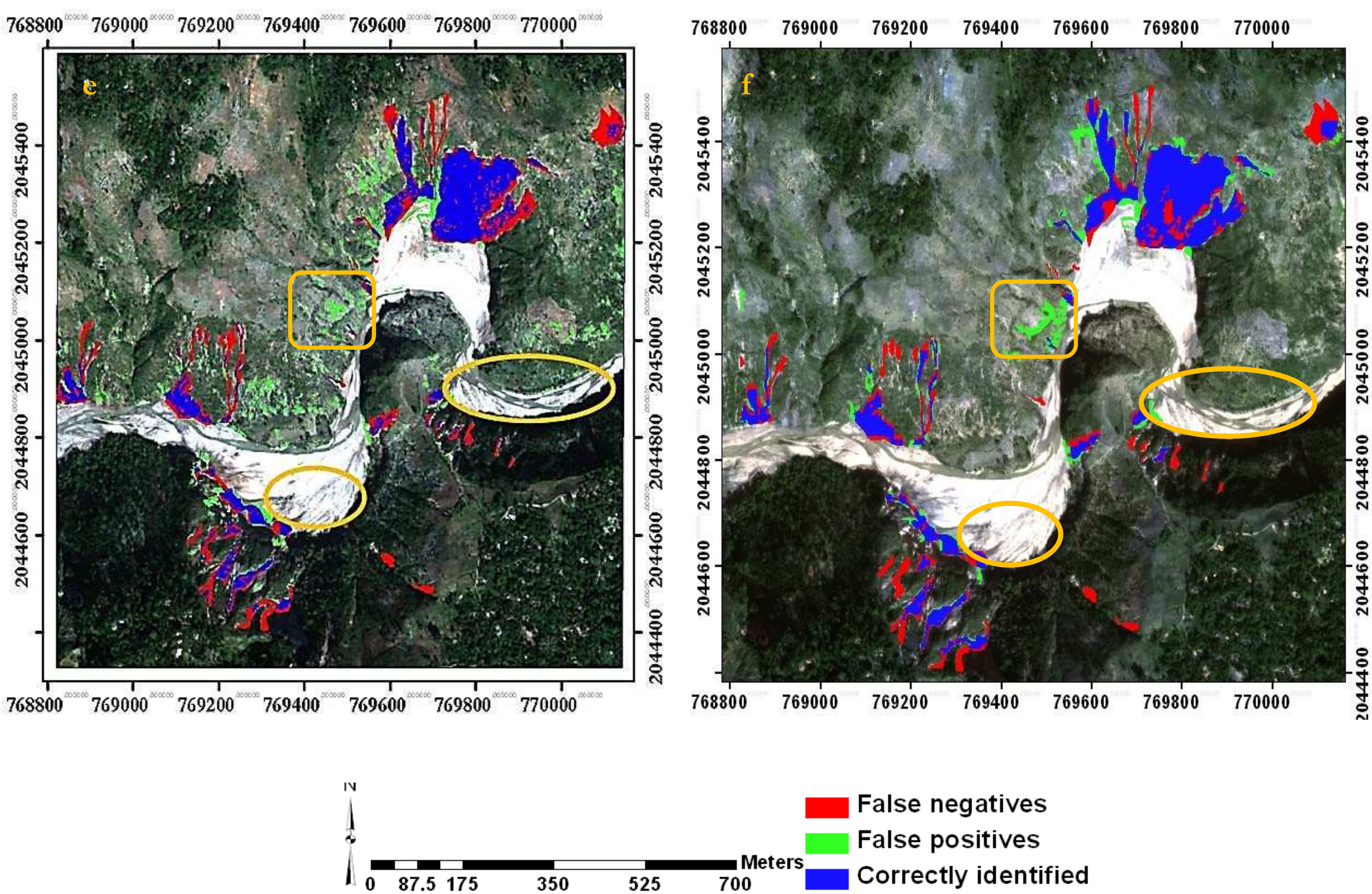
e
f
768800
769000
769200
769400
769600
769800
770000
2044400
2044600
2044800
2045000
2045200
2045400
N
0
87.5
175
350
525
700
Meters
False negatives
False positives
Correctly identified

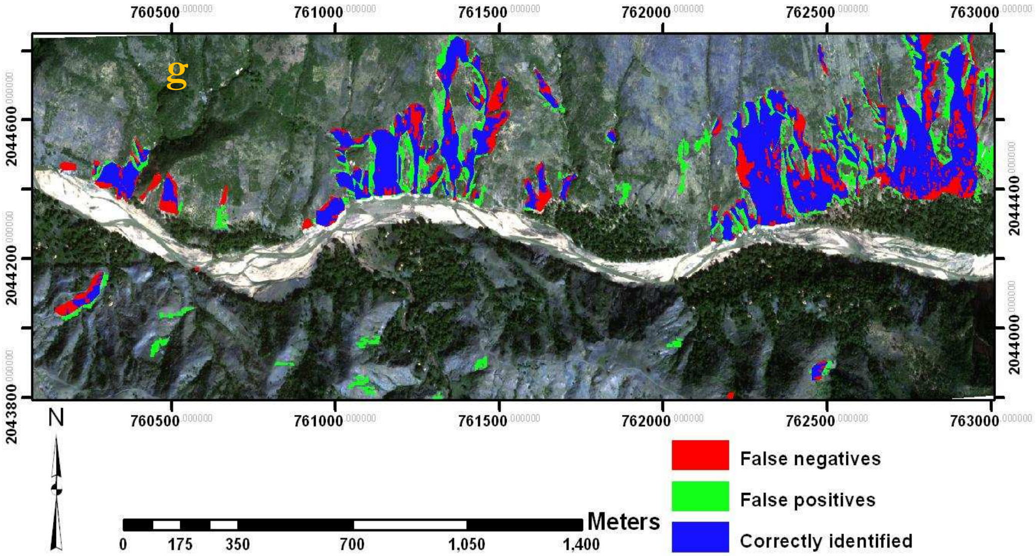

Figure 18: a) Geoeye image & Aster DEM Classified Inventory, b) Inventory from Geoeye image & Aster DEM algorithm applied on Geoeye image & Lidar DEM, c) Classified Inventory from Google Earth & Aster DEM data, d) Inventory from Google Earth & Aster algorithm applied on Google Earth & Lidar, e) Classified Inventory from Google Earth and Lidar DEM data, f) Classified Inventory from Geoeye image & Lidar DEM data (Training site) and g) Classified landslide inventory for Geoeye image & Lidar DEM for the validation site

4.6.2. Accuracy assessment for the different data combination map outputs

This accuracy assessment is based on the correct detection of landslide extent.

Data combinations	Geoeye & Aster	Geoeye & Aster algorithm applied on Geoeye & Lidar	Google Earth & Aster	Google Earth & Aster algorithm applied on Google Earth & Lidar	Google Earth & Lidar	Geoeye & Lidar (Training site)	Geoeye & Lidar (Validation site)
Total area of visual inventory (m^2)	88349.12	88349.12	88349.12	88349.12	88349.12	88349.12	307832.71
Total area of OOA inventory (m^2)	123584.81	94884.14	128375.72	85491.36	71109.12	74104.75	310002.00
Total correctly identified area (m^2)	59417.98	58088.92	58269.78	51517.67	49740.49	58688.85	215813.67
Producer accuracy (%)	**67.25**	**65.75**	**65.95**	**58.31**	**56.30**	**66.43**	**70.11**
Consumer accuracy (%)	**48.08**	**61.22**	**45.39**	**60.26**	**69.95**	**79.20**	**69.62**

Table 17: Accuracy assessment for the different data combination map outputs

4.7. Effect of DEM resolution

For this study, both the pre-disaster 30m Aster and a post-disaster 1m Lidar DEM were used for analysis mainly for the classification of fluvial deposits and clean up processes using their slope derivative (See section 4.5.3). The effect of use of different DEM data on algorithm transferability was tested by application of the algorithm developed for Geoeye & Aster and Google Earth aerial photos & Aster data combinations on Geoeye & Lidar and Google aerial photos & Lidar data combinations respectively without any modifications. From visual comparison of Figure 18a against Figure 18b and Figure 18c against Figure 18d and their respective producer and consumer accuracies in Table 17, there was a reduction in producer accuracies for both combinations after algorithm transfer. However, there was also a significant improvement in consumer accuracies for both combinations after algorithm transfer. A similar trend of improvement in consumer accuracy is also observed when results from Geoeye image & Aster DEM and Google Earth & Aster DEM are compared to those from Geoeye imagery & Lidar DEM and Google Earth & Lidar DEM data combinations respectively. Generally, there was lower consumer accuracies observed where Aster DEM was used than where Lidar DEM data was used. This is because the slope parameter derived from the Aster DEM was less efficient in accurately classifying the fluvial deposit false positive class compared to that from the Lidar DEM. This led to misclassification of parts of fluvial deposits as landslide areas.
In the study by Martha et al. [1], a drainage network derived by Stahler methodology from the 10m Cartosat_1 DEM was used in the algorithm to classify water. In an attempt to adopt the methodology, stream networks were created from both 30m Aster and the 1m Lidar DEM. As can be observed from the Figure 19 and Figure 20, the Aster DEM gave a stream network that had more locational variations than observed whereas the Lidar DEM, though gave a better locational estimation, also gave more details in terms of number of streams identified compared to those visually identifiable from the imagery.

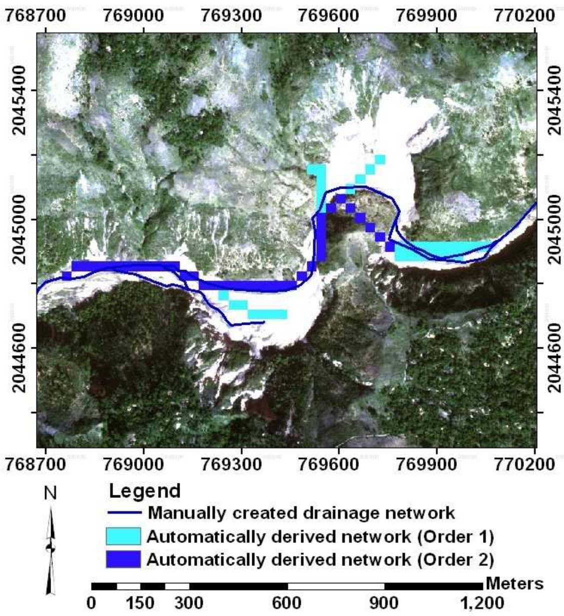

Figure 19: Aster DEM derived drainage network

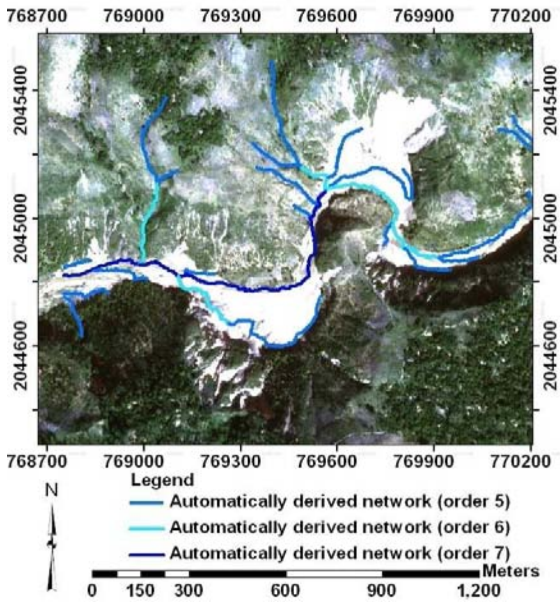

Figure 20: Lidar DEM derived drainage network

As pointed out earlier under section 3.2.2, an Aster DEM is a very large product covering very vast expanses of global land that is characterised by lots of artefacts and residual anomalies that affect its overall accuracy [105]. This limits its application for much localized applications, as in this case, that requires very detailed elevation data. Its low accuracy negatively affected the accuracy results obtained from OOA as there is a lot of elevation averaging, as has been illustrated.

With detailed information on actual presence of the additional streams identified from the Lidar DEM, this stream network is useful for more accurate OOA classification. The Lidar data used in this study, being of a much higher resolution of 1m, can be considered better data, better suited for the representation of the terrain and elevation values of the study area than the global Aster DEM. It was more efficient in classification of fluvial deposits. This also explains its higher consumer accuracy values as observed in Table 17 in data combinations where the Lidar DEM was utilised.

4.8. The effect of colour in Google Earth data

Google Earth aerial photo data has no multispectral data. Instead, it has colour information. This was the information used in the OOA process. Though Google Earth aerial photos data was of a higher spatial resolution compared to Geoeye data, it exhibited a number of short comings which are also evident in the output landslide inventories.

Elimination of false positives and false negatives was more difficult with the Google Earth data and this lead to consistently lower consumer accuracy for the data combinations where it was utilised. The outputs were also characterised of very small isolated pixels (See Figure 18c, d and e). This is often called the salt and pepper effect. Such outputs make validation on ground difficult and may sometimes be impossible.

The salt and pepper effect became more evident after a chessboard segmentation which was aimed at making small square objects that could be more accurately classified. This aroused a number of questions as to whether the salt and pepper effect was due to the effect of colour distribution associated with a small object size (1) used in the chessboard segmentation or the high detail of the Google Earth aerial photo data. Discussed below are the attempts made to establish and explain whether the salt and pepper effect was due to either or a combination of these possible reasons mentioned above.

To establish whether the salt and pepper effect was due to the high detail due to the spatial resolution, the previously 1m Google Earth aerial photo data was resampled to the resolution of Geoeye image (2m). A visual comparison of Figure 21b, c and d reveals a clear reduction in the salt and pepper effect after resampling of the data. Thus the high spatial resolution contributed significantly to the presence of the salt and pepper effect. With an increase in spatial resolution, images become more rich in information content and the internal variability within homogeneous classes is made more prominent [128-129]. This enhances the local variance making values of adjacent pixels differ significantly [130]. A class that would have otherwise had a relatively uniform appearance appears heterogeneous, incorporating very small changes in reflectance. This increase in variability reduces the statistical separability of otherwise similar classes [130] and results in a salt and pepper effect as observed with inventories from the Google Earth aerial photo data. A visual comparison of Figure 22 and Figure 23 reveals the heterogeneous nature of the Google Earth aerial photo data used in this study. The Geoeye image is more homogeneous with less internal heterogeneity thus its reduced salt and pepper effect and more effective elimination of false positives.

However, an important question that came to light was whether the spatial resolution was entirely responsible for the salt and pepper effect in the Google Earth data. This was because, even with a lower resolution of 2m (see Figure 21c), the salt and pepper effect is still present though in smaller amounts. This is not present in the results from the 2m multispectral Geoeye image (see Figure 21b) though the same general methodology was used for both data combinations. Thus, a test was set up to ascertain whether the object size of 1 which was used for Google Earth data could have contributed to the salt and pepper effect. While maintaining a common methodology in the process tree, the object size was adjusted to 2. A visual comparison of Figure 21d with Figure 21e and Figure 21c and Figure 21f indicates a reduction in the salt and pepper effect when a higher object size is used. Thus smaller object sizes increase the salt and pepper effect.

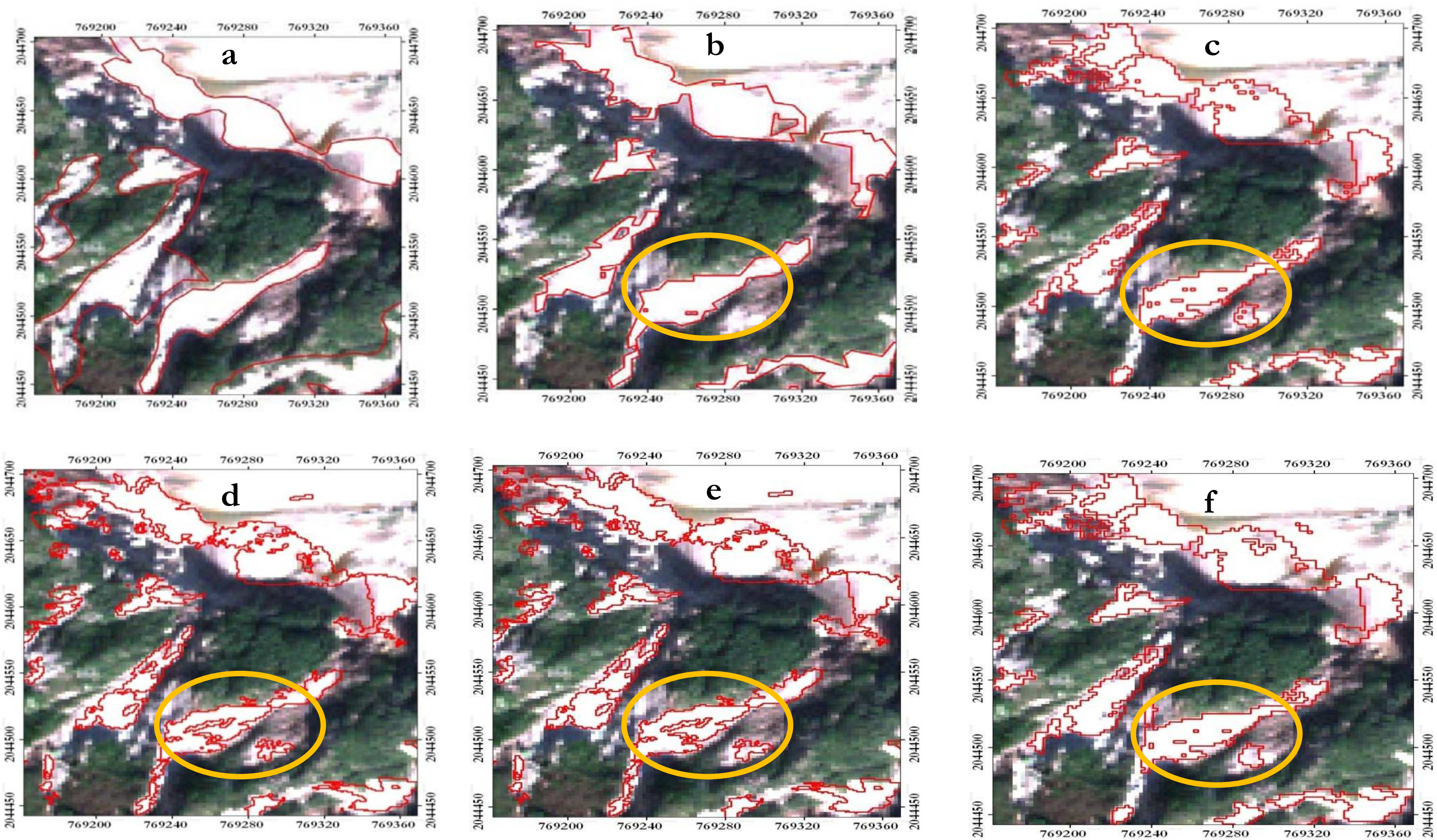

Figure 21: a) Inventory from visual interpretation, b) Inventory from Geoeye (2m)-Lidar DEM pair (object size 1), c) Inventory from Google (2m)-Lidar DEM (object size 1), d) Inventory from Google (1m) and Lidar DEM (object size 1), e) Inventory from Google (1m)-Lidar DEM pair (object size 2) and f) Inventory from Google (2m)-Lidar DEM (object size 2)

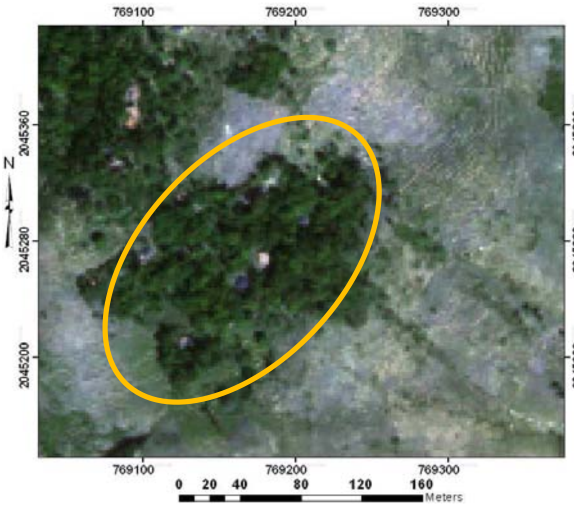

Figure 22: More homogeneous nature of Geoeye image

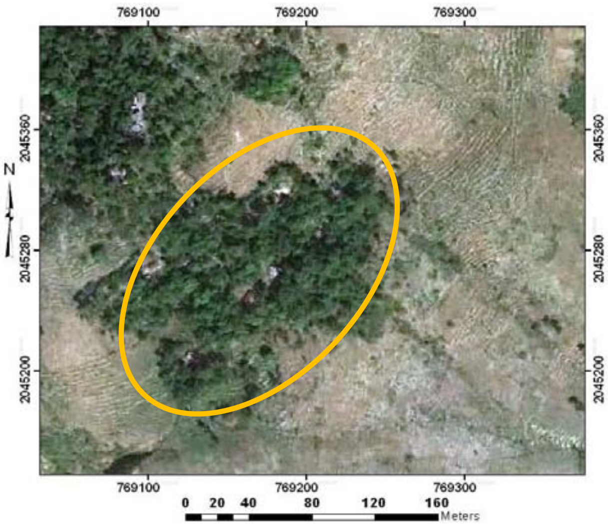

Figure 23: More heterogeneous nature of Google Earth aerial photo

The chessboard segmentation and the small object size used turned an otherwise Object-based approach into a more or less pixel-based approach. However, the object size to choose highly depends on the image resolution present and care must be taken to find the optimal object size otherwise big object sizes will in turn lead to overgeneralization which may adversely affect the accuracy of landslide identification.
Therefore, the salt and pepper effect has been attributed to the high spatial resolution of the Google Earth aerial photo data which affects the colour distribution in the data and the object size used during the chessboard segmentation.

4.9. Usability of Google Earth data Vs. Geoeye multispectral information for OOA

Since June 2005, Google Earth has been providing remote sensing data round the world. These data are endowed with a number of advantages amongst which are ability to visualise 3D and it allows users to adjust both the tilt of the line of sight and the location of the observer. These advantages coupled together give users an impression of a flight of exploration [131].
This study investigated the usability of Google Earth aerial photo data of 1m spatial resolution for Object-based landslide detection. The landslide inventories obtained from its use were compared to those from a 2m Geoeye data set. This was tested by comparing landslide inventories obtained from its use to those from a 2m Geoeye data set where similar DEM data were used. From comparison of Figure 18a with Figure 18c, Figure 18f with Figure 18e and general comparison of their producer and consumer accuracies in Table 17, it can be observed that Geoeye data, though of a lower spatial resolution compared to Google Earth aerial photo data recorded better accuracies for both producer and consumer accuracies. Possible reasons for this are discussed and explained under section 4.8.
Though not as good as results obtained where Geoeye data was used, the relatively high and not significantly deviant producer accuracy for the Google Earth aerial photo & Aster DEM and Google Earth aerial photo & Lidar DEM data combinations from those obtained by Geoeye suggests that non-spectral Google Earth aerial photo data could potentially be used in lieu of high resolution multispectral data for OOA work. The usability of Google Earth aerial photo data comes in handy especially in developing countries, facilitating substantial savings in terms of both cost and time.

4.10. Transferability of the developed algorithm to the validation site

Availability of timely information during the immediate aftermath of disasters both for search, rescue and timely planning requires methodologies that hasten the data analysis process. OOA provides this option. However, it can also be time consuming with manual selection of object features, parameters and thresholds. This could be reduced by having an easily transferable OOA methodology for landslide identification. The possibility of having an easily transferable algorithm for the Haiti area was tested by applying the algorithm developed for a training site on the validation site without modifications.

As observed from Table 17, when the Geoeye & Lidar DEM algorithm developed for the training site was used for landslide detection on the validation site, it gave producer and consumer percentage accuracies of 70.11 and 69.62 compared to 66.43 and 79.20 obtained in the training site. The percentages obtained on the validation site, though with lower consumer accuracy than those recorded in the training site, highlight a high potential for creation of a fully transferable algorithm for the Haiti area with better accuracies. With a better methodology to efficiently eliminate the false positives and false negatives, there exists a high potential for an accurately transferable algorithm for the Haiti region.

One major challenge observed in this study, is striking a balance between creating an algorithm that was both accurate and robust enough to accommodate variability between the study and validation sites. There is always a conflict between ensuring a robust and at the same time accurate algorithm. The optimal balance between the two has to always be established for an efficient and transferable algorithm. Establishing such a balance is always laborious as it is a trial and error approach with this methodology.

4.11. Accuracy of outputs and choice of the best data combinations

One of the other challenges experienced in this study was finding an optimal balance of the producer and consumer accuracies. Both poor consumer and producer accuracies of the landslide inventory have adverse effects on all the subsequent processes the output is used for. Low producer accuracy may lead to under estimation of risk to landslide hazard as this means that some landslide areas are left out whereas low consumer accuracy may lead to over estimation of the risk to landslide hazard due to inclusion of non landslide areas. However, from a personal and risk reduction perspective, over estimation of the risk can be better accommodated than an under estimation [132-133] thus better a low consumer accuracy than producer accuracy. However this is subjective and different researchers may have different takes/views on this matter. Depending on the intended use of the outputs, efforts can be made to maximise the accuracies with preference to one more than the other. However, in this study, efforts were made to balance the best combination of the two accuracy measures by different trials and selection of one algorithm with more balanced accuracies.

For all algorithms and data combinations, there was a systematic non recognition of the thin shaped landslides, probably due to inappropriate delineation during segmentation as a result of their thin shape and occurrence in spectrally similar classes [1]. Also, there was systematic recognition of bare agricultural fields as landslides which exhibited spectral signatures that are more or less similar to those for landslides (see Figure 25).

From a comparison of producer and consumer accuracies in Table 17, the algorithm developed for the training site using Geoeye image & Lidar DEM data gave the best result with the best balance of producer accuracies compared to the other data combinations. This can be attributed to the high level of detail (spatial resolutions) of both the multispectral data and DEM. It can also be attributed to the presence of multispectral information that facilitated more accurate elimination of false positives compared to Google Earth data that had a salt and pepper effect.

4.12. Pros and cons of each data combinations

Table 18 gives a summary of the pros and cons of use of each of the data sets used in this study in relation to Object-based landslide detection and transferability of OOA algorithms.

DATA	ADVANTAGES	DISADVANTAGES
ASTER DEM	▪ Aster DEM data are free and easily accessible for most areas of the world making algorithms developed from such combinations more transferable to other geographical areas.	▪ OOA products obtained from Aster DEM have less accurate approximations of landslide boundaries. This is mainly due to the DEM'S low spatial resolution which makes derivatives like slope and hillshade less representative of the reality.
LIDAR DEM	▪ Ensures better approximations of landslide boundaries and elimination of false positives and negatives due to better representation of the reality	▪ Not easily accessible, is expensive and usually with a low coverage for the most parts of the world thus limiting algorithm transferability to areas without this data or with limited funds to purchase them.
GOOGLE EARTH	▪ Google Earth data are free in that its users do not pay directly and it is easily accessible for most areas of the world. This makes algorithms developed from such combinations more transferable to other geographical areas. ▪ They are usually provided in very high resolutions. ▪ The ability to use Google Earth software to display the data provides a better insight into the study site. It provides the ability to visualize 3D and allows users to adjust both the tilt of the line of sight and the location of the observer [131].	▪ The outputs are affected by the salt and pepper (they have many tiny pixels) effect making the ground-truthing for such outputs problematic. ▪ Due to the mosaic nature of Google Earth data, they are characterized by stripes along the joining lines thus introducing errors during the OOA process (See Figure 24). ▪ The user does not get direct access to the raw data. This limits the extent to which the user can enhance the image to provide improved viewing and interpretation. Instead, compressed versions are provided which are smaller in file size at the expense of spatial and spectral detail [134]. ▪ They often lack easily accessible and detailed metadata as was experienced in this study.
GEOEYE	▪ Good quality spectral image data with up to 0.5m spatial resolution panchromatic band data facilitates better elimination of false positives and false negatives due to its good representation of reality.	▪ Geoeye images are expensive to purchase and not readily accessible for many areas around the world due to their low coverage, limiting transferability of algorithms developed using this data to other geographical areas.

Table 18: Pros and cons of each data combination

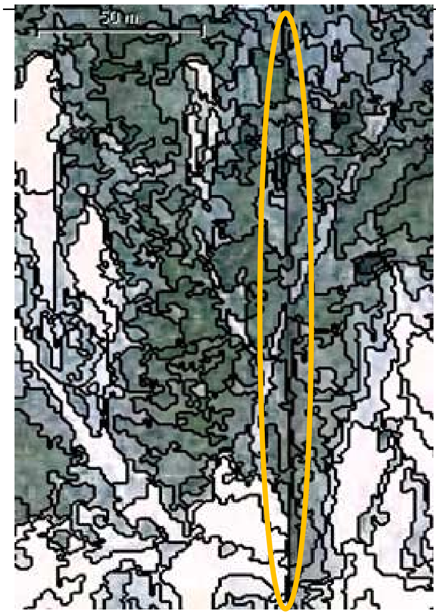

Figure 24: Stripped Google earth aerial photo

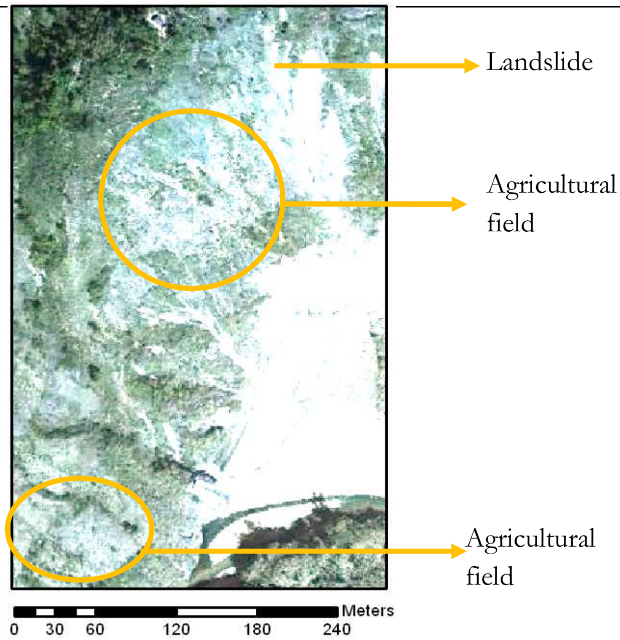

Figure 25: Ambiguities in spectral signatures

4.13. Frequency-Area distribution for the OOA landslide inventories

Figure 26 are the Frequency-area distribution curves obtained for the landslide inventories obtained from visual image interpretation, Google-Aster and Geoeye-Lidar data combinations.

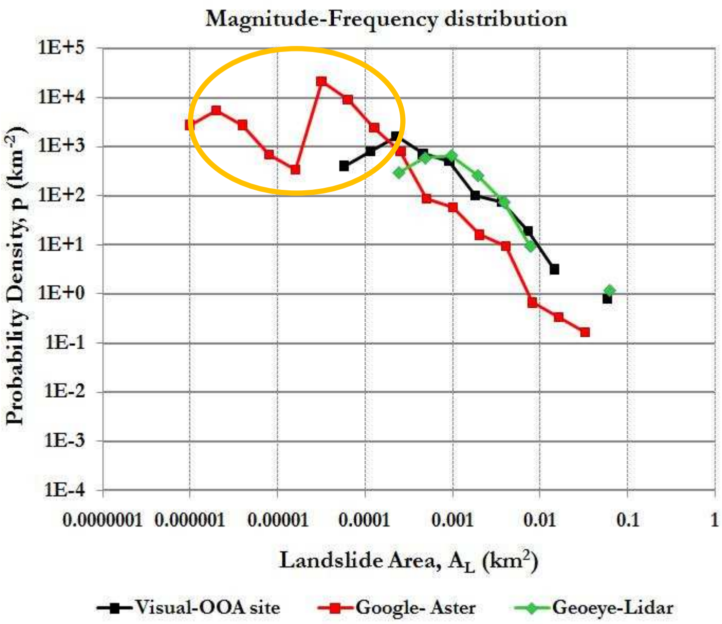

Figure 26: Frequency-Area distribution for the OOA landslide inventories

Google Earth aerial photo & Aster DEM data combination gave the highest probability density for small sized landslides. Also, its trend is significantly deviant from that of the visual inventory in comparison to the trend obtained from Geoeye & Lidar data combination. This can be attributed to the salt and pepper effect with this data combination which leads to outputs that are less representative of the reality.

4.14. The Plateau objective function analysis for Geoeye & Lidar data combination.

4.14.1. Scale factor optimisation

As noted in earlier parts of this discussion, the previous methodology used to determine the scale factor and thresholds to use was based on a trial and error approach in combination with visual assessment which was identified as laborious, irreproducible and may not lead to robust algorithms. It was based on use of only one scale factor for classification of all the false positives and landslide sizes, a criterion not reasonable due to existence of a lot of variability in sizes of landslides and their false positives in the real world. Also, the thresholds used are not dynamic as they are user-defined and not data-driven. This second methodology was aimed at testing the feasibility of use of non user-defined optimal multi-scales and dynamic and data-driven thresholds for landslide classification. Objective function values were computed at different scales from 5-50 (in increments of 1) using mean brightness values for the Geoeye image. The POF value was computed and obtained at 1.13. The optimal segmentation scales obtained are 27, 29 and 31 as indicated in the Figure 27. Initial segmentation was carried out at scale 27. According to Martha et al. (in review) [3], the scale factor corresponding to the first peak has the highest capability to properly delineate small landslides compared to the other peaks. This was true for this study too as the other two scale factors were already too coarse (high) to accurately delineate the small landslides. This is the reason why the scale factor at the first peak was chosen.

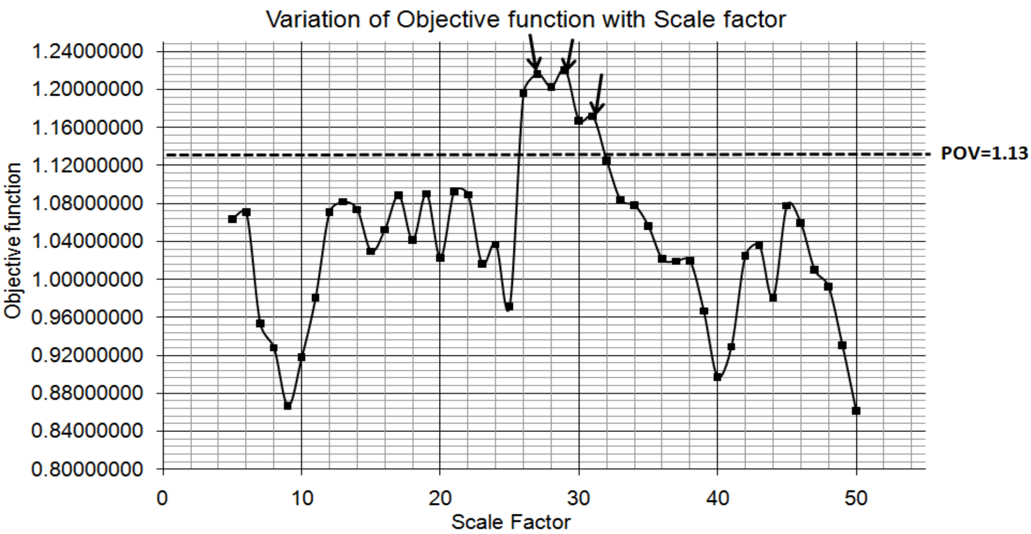

Figure 27: Objective functions illustrating the peaks used in OOA segmentation

The optimal scale values identified by the POF are significantly higher than the 10 scale factor previously identified by visual assessment as optimal. Important question that came to mind is whether use of these optimal scales in combination with dynamic thresholds from k-means cluster analysis would improve the landslide detection process. This question is answered under section 4.14.4.

4.14.2. Separation of landslide candidates from background

At scale factor 27, the NDVI criterion was used to obtain class centres by k-means clustering. One essential input into k-means cluster analysis is the number of clusters. To determine this objectively, a two-step cluster analysis was first carried out to obtain the most optimal number of clusters. This was then used as input into k-means cluster analysis. The cluster centres obtained are as shown in Table 19. The background was separated from landslide candidates by use of the NDVI criterion. Areas with NDVI value >= 0.412 were classified as background (This was also comprised of the agricultural areas with trees). This is because we do not expect landslides in highly vegetated areas so better to eliminate them from any further analysis.

	Clusters identified			
	cluster 1	**cluster 2**	**cluster 3**	**cluster 4**
Mean NDVI cluster centres	-0.171	0.063	0.248	0.412
Class thresholds created from cluster centres	Mean NDVI≤-0.171	Mean NDVI≤0.063	Mean NDVI≤0.248	Mean NDVI≤0.412 Mean NDVI≥0.412
False positive class identified in cluster by visual assessment	Shadow+ agriculture	River water	Mixed class of all false positives and landslides though dominantly Fluvial deposits	Mixed class of all false positives and landslides though dominantly agricultural

Table 19: Cluster centres from NDVI criterion at scale factor 27

The classes created from the thresholds were therefore used as a basis for further classification of false positives.

4.14.3. Classification of false positives and clean up

Table 20 gives the criteria used for classification of false positives and clean up processes

Separation of landslides from false positives				
False positive	Scale Factor	Classes used as basis for segmentation and classification	Criteria	Method to obtain threshold
River water	27	cluster 2	-0.121>Mean NDVI≤ 0.063	Two-step and K-means cluster analysis
Shadow	31	cluster 1, 3 & 4	Mean hillshade≤ 72.147	
Fluvial deposits	31	cluster 3 & 4	Mean slope≤ 6.355	
			Existence within 100m distance from water	Contextual information
Agricultural area	29	cluster 1, 2, 3 &4	Mean slope≥11.488 GLCM StdDEV (quick 8/11) pan (all dir.) <=3.4	Two-step and K-means cluster analysis
Agricultural with trees	29	cluster 1, 2, 3 &4 (Same as background class)	Mean NDVI ≥0.412	
Clean up processes				

- clean up of isolated false positives
  - class3, class4 with Brightness >= 117 at image level: landslides and false positives_
- reclassify remaining as landslides
  - landslides and false positives_ with Mean slope >= 12 at image level: landslides_
- Clean-up
  - shallow translational slides
    - landslides_ at Image level shallow translational slide
  - clean up landslide impurities
    - shallow translational slide with Max. diff. >= 2 at image level: unclassified
    - landslides at image level merge region
    - shallow translational slide with Area <= 160 Pxl at image level: unclassified
    - shallow translational slide with Standard deviation pan <= 66 at image level: unclassified
  - Merge all false positives
  - export landslides

Table 20: Criteria for classification of false positives and cleanup process

River water was fully identified by cluster 2 using the NDVI criterion. Shadow was identified using the hillshade information. Areas covered by shadow usually characterised by low hillshade values thus the obtained threshold. Fluvial deposits were identified and classified using a slope and distance from water criteria. Fluvial deposits usually occur in low lying areas, this is the reason why the slope criterion was efficient. They also occur in areas nearest to Momanche River. Agricultural areas with trees are characterised by high NDVI values and were classified by a similar threshold for the background class. Pure agricultural areas were the hardest class to classify with no clear cut spectral signature. However, criteria of slope and GLCM texture measure for the panchromatic band were found useful for the classification. The clean up processes were performed at a scale factor of 27. The criteria used to eliminate false positives include brightness, mean slope, maximum difference, area and mean standard deviation of the Geoeye panchromatic band as seen in Table 20. Indicated in the next section are the inventories and accuracies obtained..

4.14.4. Output landslide inventories and accuracy assessment

Figure 29 and Figure 30 show the landslide inventory outputs

Figure 28: Segmentation at scale factor 27

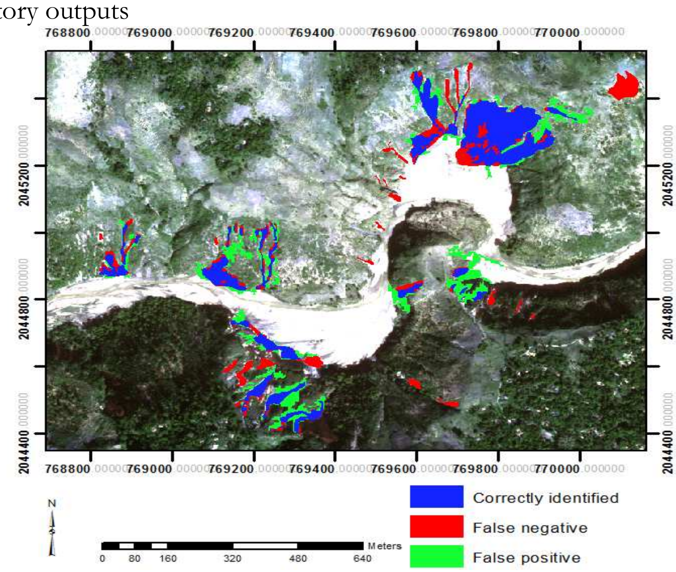

Figure 29: Classified landslide inventory from training site

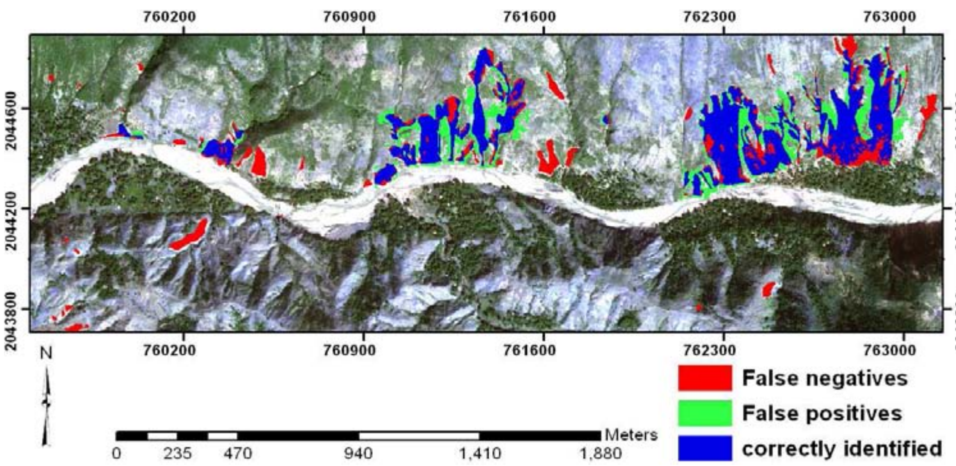

Figure 30: Classified inventory from validation site

	Training site	Validation site
Total area of visual inventory (m^2)	88349.12	307832.71
Total area of OOA inventory (m^2)	94858.00	313220.00
Total correctly identified area (m^2)	59752.72	212907.65
Producer accuracy (%)	**67.63**	**69.16**
Consumer accuracy (%)	**62.99**	**67.97**

Table 21: Accuracy assessment by correct detection of landslide extent

A comparison of producer and consumer accuracies for Geoeye & Lidar data combination obtained with user-defined parameters and thresholds and when segment optimization is carried out in combination with data-driven thresholding by k-means cluster analysis indicate no significant improvement in the accuracies. No significant differences were recorded amongst the accuracies though better consumer accuracy was observed with user-defined single scale factor and thresholding. This can be attributed to better user control in elimination of false positives with this approach than with data-driven methodology. Also, the differences in scale factors used could have been the other reason. Visual assessment of delineations made at scale factors 27, 29 and 31, which were identified and used as the optimal scale factor for data-driven analysis, shows imperfections in delineation of small and narrow shaped landslides (see Figure 28). So, the multi-scale segmentation approach and data-driven thresholds did not significantly improve the accuracies previously obtained from the single scale, user-defined thresholding approach (67.63% vs. 66.43% producer accuracies for the training site). When the algorithm was tested on the validation site, it gave producer and consumer accuracies of 69.16 and 67.97% compared to 67.63 and 62.99% at the training site. These relatively balanced (not significantly different) accuracies could be an indicator that this algorithm is relatively robust though it did not necessarily give better accuracies.

4.15. Environmental factors affecting presence of landslides

To understand the environmental factors affecting the presence of landslides, the WoE modeling method was used in combination with the contrast factor. Contrast factor is a measure of the correlation between points and patterns [135]. It quantifies the spatial association between a map class and the occurrence of landslides. A number of possible landslide causative factors were used to determine the pattern of the Haiti landslides and to explain why the landslides took place where they did. These included lithology, flow direction, distance to roads, slope, aspect, distance to rivers/drainage lines, Distance from Enriquillo Plantain fault and elevation. Presented in Figure 31 and Figure 32 are the factor susceptibility maps and contrast factors obtained from the analysis and thereafter, explanations on possible reasons for the trends obtained for landslide distributions.

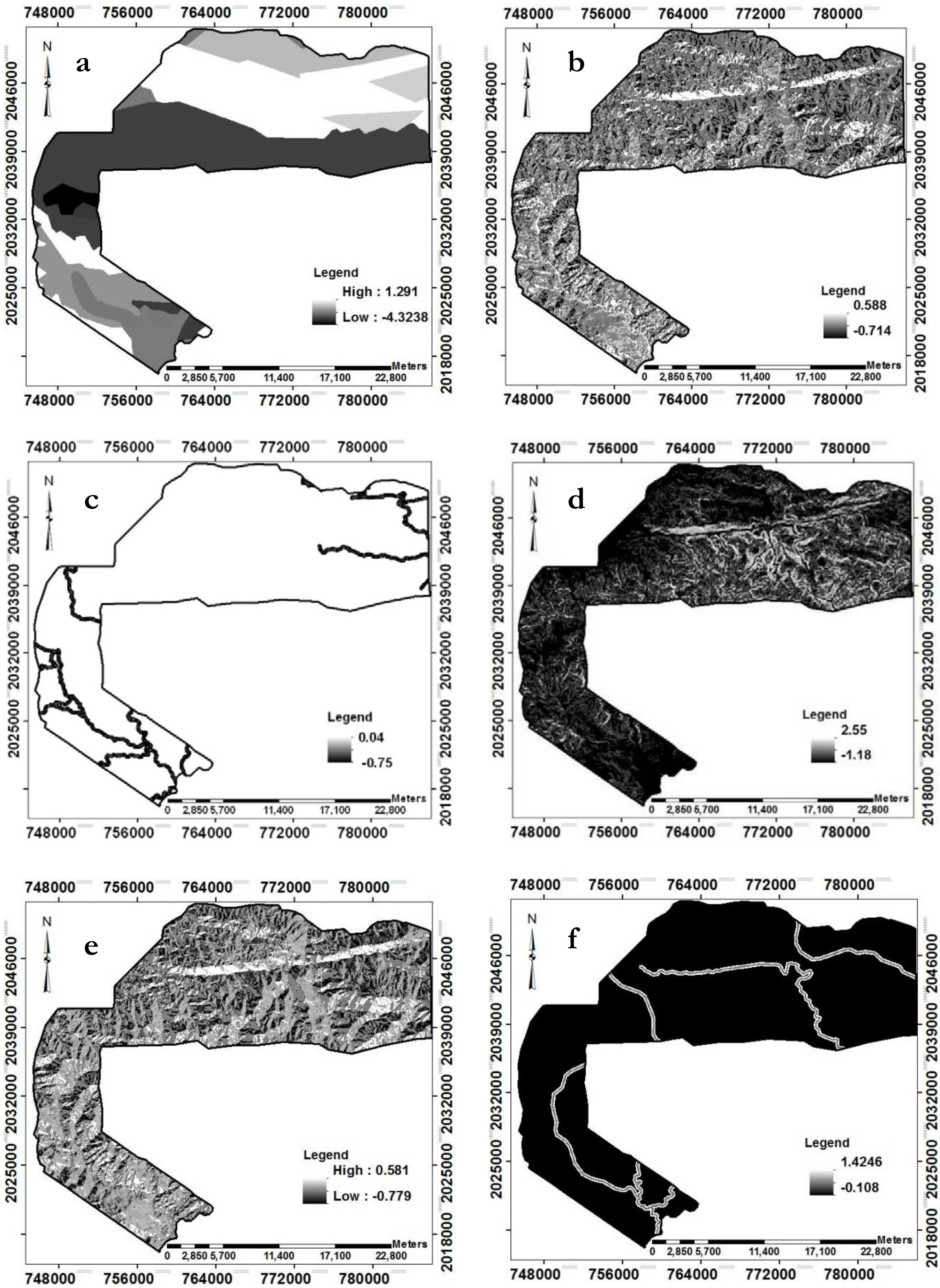
a
Legend
High : 1.291
Low : -4.3238
b
Legend
0.588
-0.714
c
Legend
0.04
-0.75
d
Legend
2.55
-1.18
e
Legend
High : 0.581
Low : -0.779
f
Legend
1.4246
-0.108
N
Meters
0 2,850 5,700 11,400 17,100 22,800
748000 756000 764000 772000 780000
2018000 2025000 2032000 2039000 2046000

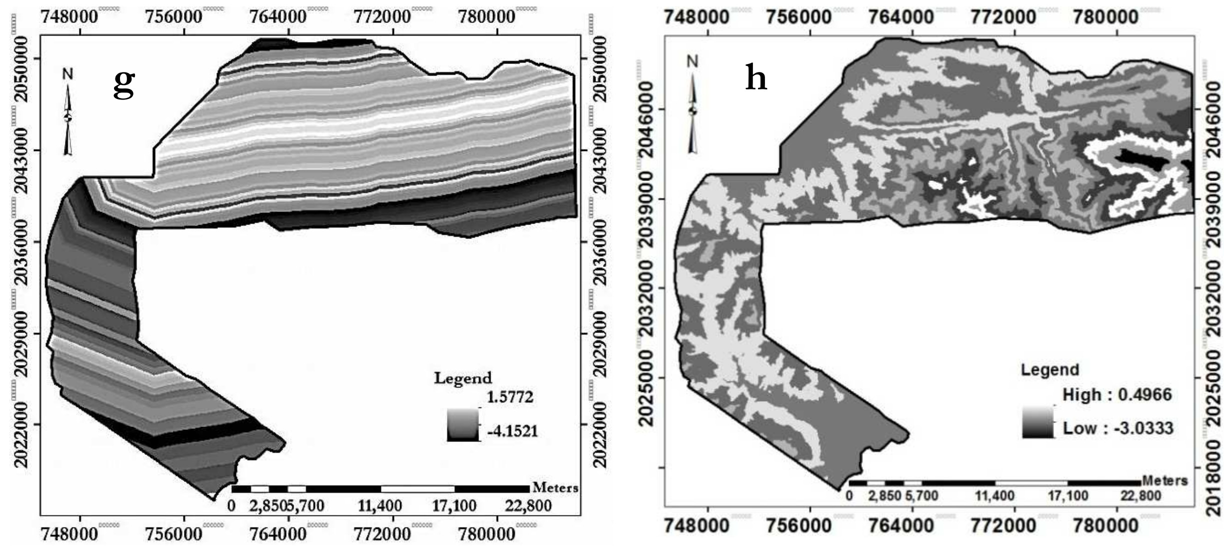

Figure 31: Weight maps of a) Lithology, b) Flow direction, c) Distance from major roads, d) Slope, e) Aspect, f) Distance to rivers, g) Distance from the Enriquillo fault and h) Elevation

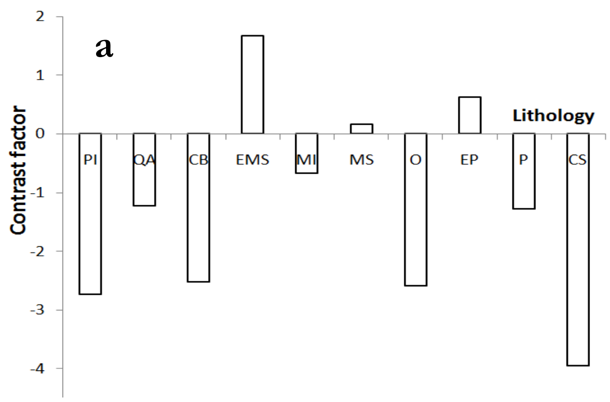

See legend under appendix E

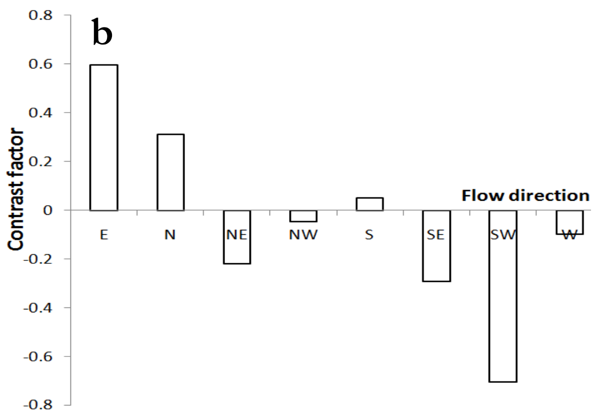

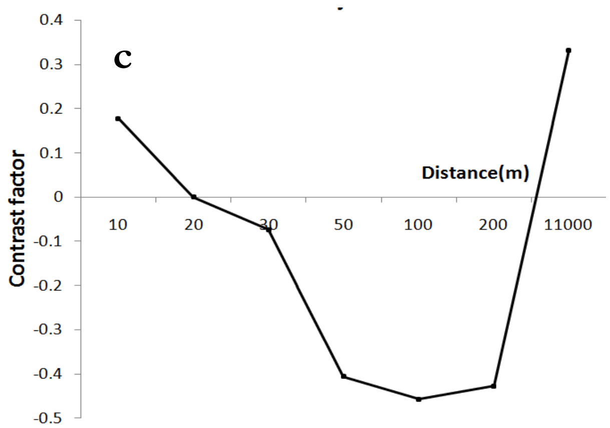

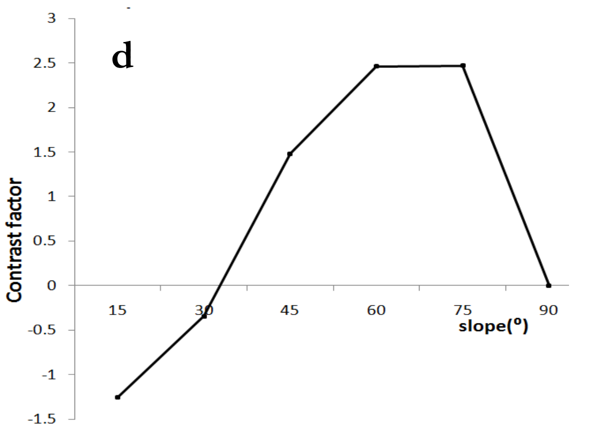

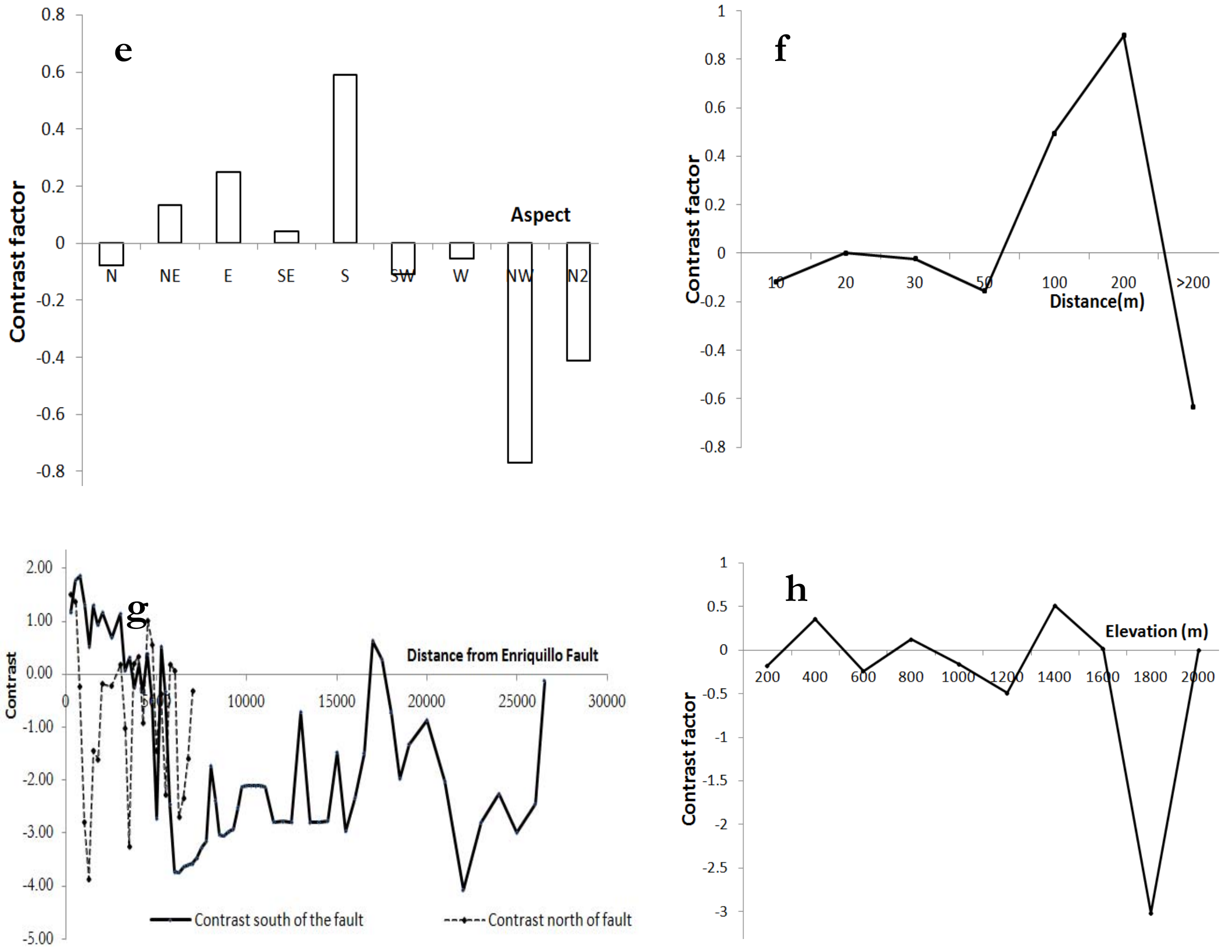

Figure 32: Variation of contrast factor with; a) Lithology, b) Flow direction, c) Distance from major roads, d) Slope, e) Aspect, f) Distance to rivers, g) Distance from the Enriquillo fault and h) Elevation

4.15.1. Lithology

The study area is characterized of sedimentary and volcanic rocks. From Figure 32a, landslides dominated in the Middle to Upper Eocene limestone geologic unit characterized by pelagic biomicrites due to significantly highly positive contrast factor of 1.67. Other geologic units that also had positive contrasts are those characterized by tertiary sedimentary Upper Palaeocene to Lower to Middle Eocene and sedimentary- tertiary Upper Miocene limestone rocks. However, all the other geologic units had negative contrast implying a negative association between their occurrence and the presence of landslides. The highly negative contrast was exhibited by the geological unit characterized by tertiary Senonian pelagic limestone.

4.15.2. Flow direction and aspect

The landslides occurred mainly in the East and Northern directions of flow with contrast factors of 0.60 and 0.31 respectively. All other directions, except for South which had an almost zero positive contrast and North West and West which had an almost zero negative contrasts, had negative weights and negative contrast factors as illustrated in Figure 32b.The South Western direction greatly inhibited the occurrence of landslides. The presence of an almost zero contrast for the North West, South and West implies that these directions had no significant effect on occurrence of landslides as they occur there only by chance.

The aspect of a slope determines slope exposure to sunlight, drying winds and rainfall [92, 136-137]. These in turn affect both moisture retention and presence/absence of vegetation, which in turn may affect the strength of the soil thus the susceptibility to landslides [138]. From Figure 32e, it can be concluded the landslides dominated in the Southern facing slopes which have the highest positive contrast of 0.59. Also, we had positive association between aspect and landslide density in the South-East, East, and North-East. The landslides were highly inhibited in the North-West facing slopes where the contrast factor was -0.77. The North, North2, South West and North West facing slopes too had a negative association between the slope and landslide density.

Though these factors are considered to be related and should give relatively similar trends, they exhibited variations in trends. This can be attributed to the approach in computation of directions because whereas flow direction is computed for every central pixel of input blocks of 3 by 3 pixels, each time comparing the value of the central pixel with the value of its 8 neighbours, the computation of aspect depends on the slicing angles used as boundary values and ILWIS software provides 9 possible aspect classes. However, important to note for both factors is that a trend was observed where there was a negative association with all directions to the West and a positive association with directions associated with the East.

4.15.3. Distance from major roads

From the weighted factor map in Figure 31c and the ranges of contrast statistics displayed in Figure 32c on distance from major roads, it can be concluded that the distance from major roads played no significant role in the occurrence of landslides. According to the statistics, the landslides that occurred did within 10m from the roads with a low contrast value of 0.1778 and in distances greater than 200m meters. All other distances between 10 and 200m inhibited the occurrence of landslides. However, important to note is the steadily decreasing trend of contrast factors up to a distance of about 100m. The unexpected increase in the contrast after the distance of 200m may be attributed other factors that come into play to determine the pattern as it is unreasonable for roads to affect occurrence of landslides at such long distances. Thus, from this study, distance from major roads is not a factor that significantly determined the pattern of the landslides.

4.15.4. Slope

From Figure 32d, it can be concluded that most of the landslides occurred in the slope range of 30-75^{o} with the most number within 60-75^{o} slope range. These slope ranges, even in reality, are considered favourable for the occurrence of landslides. However, the negative contrasts in slope ranges 0-30 imply a negative association between the slope and landslide density. The presences of slopes of 0-30^{o} inhibit the occurrence of landslides, according to this analysis. Also, after in the slope range of 75-90^{o}, no landslides were reported there. This can be attributed to very steep slopes that most often than not, do not favour the occurrence of landslides thus the observed trend. This trend fits what we would expect in reality. The resultant susceptibility map from these dynamics can be viewed in Figure 31d.

4.15.5. Distance from Rivers/drainage lines

As the distance from drainage lines increases, the probability of occurrence of landslides should/ is expected to decrease. From Figure 32f, there is no reasonable trend of association within a distance of 200m from the drainage lines. There are negative contrast factors within a distance of 50m from the drainage lines contrary to what is expected. However, after 200m, there is a clear reduction to highly negative contrast. This is what is expected in the real world due to less influence of the water seepage at longer distances away from the river. For the landslide susceptibility map from these dynamics, see Figure 31f.

4.15.6. Distance from Enriquillo Plantain fault

Closest to the active fault lines, the probability of occurrence of landslides is expected to be higher than areas far away. From Figure 32g, generally, the contrast factor values were high and exhibited a decreasing trend until at a distance of approximately 1250m where the pattern fades out and becomes relatively uneven though still significantly low compared to those near the fault. Recent evidence indicates the lack of surface rupture, coupled with other seismologic, geologic and geodetic observations, suggests that little, if any, accumulated strain was released on the Enriquillo–Plantain Garden strike-slip fault in the earthquake [139-140]. This stress can be concluded to have caused the occurrence of landslides nearest to the fault. The reducing trend is due to the reduction of stress away from the fault until the point where it doesn't significantly affect and other factors come into play. There is highest landslide susceptibility along the fault too (See Figure 31g).

According to Figure 32g, landslides dominated more on the Southern than the Northern part of the fault. Emerging evidence indicates that Haiti earthquake ruptured on a previously unmapped blind thrust fault now called the the Léogâne fault which lies subparallel to but is different from the Enriquillo–Plantain Garden fault. It is said to have resulted into elevated topography to the South of the Enriquillo–Plantain Garden fault [141]. This could explain the dominance of landslides to the South of the Enriquillo fault.

4.15.7. Elevation

High elevations are usually characterized by mountain summits that usually consist of weathered rocks with higher shear strength. At intermediate elevations are thin colluviums that are usually more susceptible to landslides. However, at very low elevations, the occurrence of landslides is limited because the terrain itself is gentle and covered by thick colluvial material. A high water table will be required to initiate landslides in such areas [138]. According to the susceptibility map in Figure 31h and Figure 32h no significant or well defined trend was observed for the influence of elevation in most ranges of elevation. Except for elevation ranges of 1200-1400m, where there is a contrast factor of 0.51 and in areas with elevation ranges of 1600-1800m, where have negative 3.6 for the contrast factor and there were no landslides above 1800 meters there were no significant trends. The lack of landslides and a highly negative contrast at very high elevations can be attributed to high shear strength of the rocks. The positive contrast factor for elevation 1200-1400m can be due to presence of relatively favourable conditions for the occurrence of landslides at these elevations.

4.15.8. Success rating to select the best factors

For each of the factor maps included in the analysis, a weight map was obtained. Success rating was performed for the weight maps. Success rating is a good method for accuracy assessment of landslide susceptibility maps. It indicates how much percentage of all landslides occur in the classes with the highest value of susceptibility map [142]. It indicates how well the created model performs for the landslide evidence from which it was made. To determine which factors significantly affected the pattern of landslides, a sensitivity analysis was carried out for all the factors. The results from this analysis are shown in Figure 33.

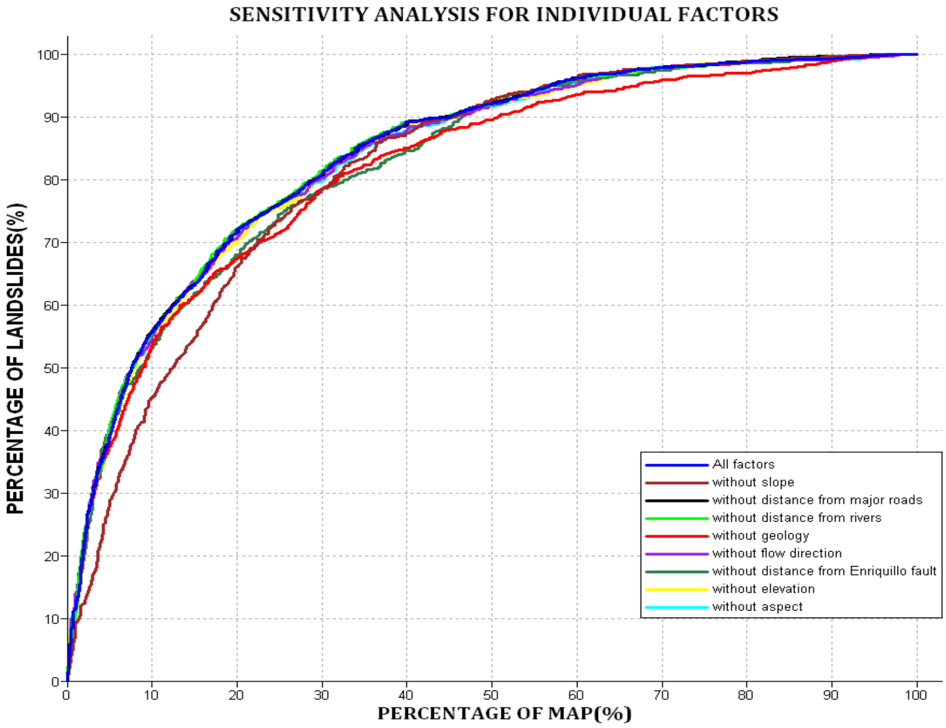

Figure 33: Sensitivity analysis for individual factors

From Figure 33, it can be concluded that there were three main factors that determined the pattern of landslides in Haiti. These were; lithology, slope, and the distance from the Enriquillo fault. This step was important for understanding the extent to which each of the factors determines the pattern of landslides.

4.15.9. Susceptibility map for the study area

The susceptibility map was obtaining by summing up the weight maps of the causative factors and success rating was performed for the output map. The results obtained were used in the classification of the map into susceptibility classes low, low to moderate and moderate to high. The most reasonable map output was obtained at 20.07 and 60% of map pixels (See Figure 34). The weights at these percentages were obtained from the cross table statistics and used as thresholds for slicing the susceptibility map.
From Figure 35, low susceptibility means the areas where there is less likely to be any landslides. Such areas are usually considered safe for development, including human settlement. Low to moderate susceptibility means that the areas are averagely safe and can be developed with a number of protection measures in place. Moderate to high susceptibility, on the other hand implies that the areas are highly unstable and are not suitable for development especially human settlement.
From the susceptibility map in Figure 35, it can be concluded that the highest landslide susceptibility within this study area is located in the areas surrounding the Enriquillo Plantain fault. From the success rating of the landslide susceptibility map, it can be concluded that the output susceptibility map is a fairly good predictor for the landslides because for example, to predict 80% of the total landslides, we need 30% of the susceptibility map.
Important to note is that with more and better thematic data for the study area, this susceptibility map can be improved on. Also, depending on the boundary values selected for slicing of the susceptibility, this map may appear different. However, reasonable thresholds should be selected to obtain meaningful results.

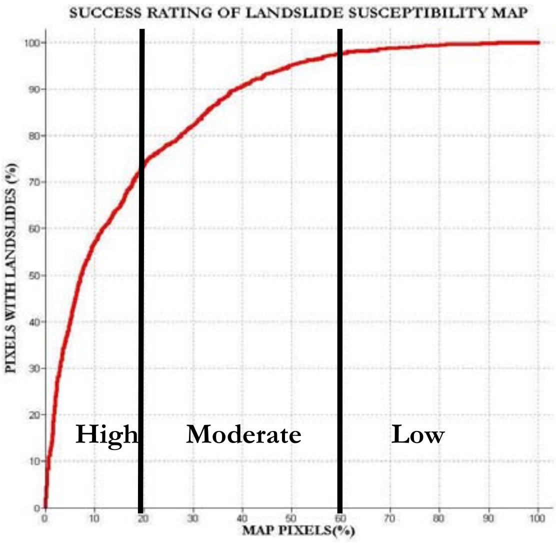

Figure 34: Success rate curve for landslide susceptibility map

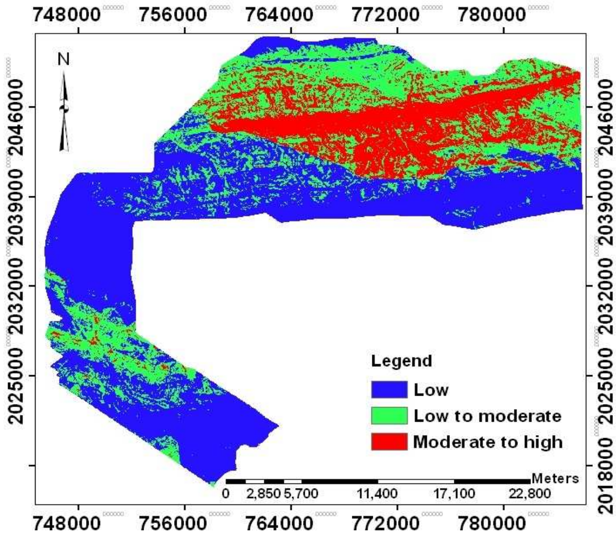

Figure 35: Classified Landslide susceptibility map

4.16. Application of results from susceptibility analysis for improvement of OOA output

The total susceptibility map from susceptibility analysis was used in improvement of the OOA process for the Geoeye-Aster data combination. It was found useful in the elimination of some of the false positives. This was achieved by adding an extra condition susceptibility ≤ 2.2 to the clean up processes. Areas with total susceptibility equal to or less than 2.2 were considered as non-landslide zones. The individual weighted factor maps like geology were not very useful for application in the OOA process. This was due to the low detail of both the thematic and DEM data used in the susceptibility analysis so the individual weighted factors were not good for such a much localised application. The resultant classified landslide inventory is as shown in Figure 36.

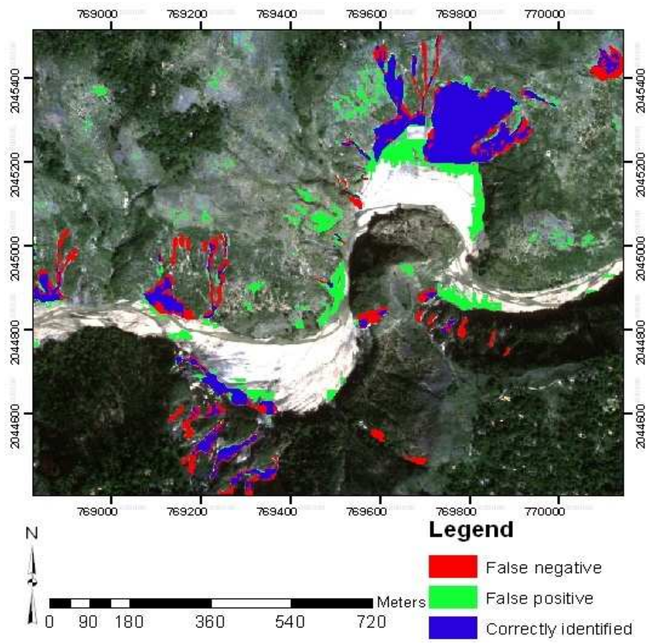

Figure 36: Classified landslide inventory obtained from Geoeye-Aster after incorporation of susceptibility weight map

Data combinations	**Geoeye & Aster**
Total area of visual inventory (m^2)	88349.12
Total area of OOA inventory (m^2)	98196.00
Total correctly identified area (m^2)	58221.57
Producer accuracy (%)	**65.90**
Consumer accuracy (%)	**59.29**

Table 22: Accuracy assessment for the output landslide inventory after incorporation of susceptibility

An accuracy assessment based on correct detection of landslide extent was carried out (see Table 22). The producer and consumer accuracies obtained are 65.90 and 59.29% respectively. An improvement in consumer accuracy was registered from the previously obtained 48.08 to 59.29% after incorporation of the total susceptibility weight map. This highlights the possibility of use of information from susceptibility for improvement of OOA outputs. With better/more detailed thematic and DEM data, information from susceptibility analysis could be very useful for OOA as well. A large number of false positives were still existent in the output due to the presence of bare agricultural fields which were hard to eliminate and the coarse nature of the Aster DEM (thus slope derivative) which led to inefficiency in classification of fluvial deposits.

4.17. Chapter summary

This chapter contained the results and discussion. It began with a presentation of the initial statistical characteristics of the landslide inventories obtained from stereo visual image interpretation for study areas of pattern analysis, training site and validation site for OOA. It presented and described the Frequency-Area distribution trend of the entire inventory from stereo image interpretation in relation to previously established trends available in literature of previous studies. It further described the training study site in terms of its false positive classes. The low accuracies obtained from the application of the unchanged adopted algorithm on the training site for this study are explained. This chapter also described, in detail, the step by step parameterisation done when the adopted algorithm was being adapted to the training site with an explanation of why specific parameters, object features and thresholds were selected for the specific false positives. Discussions were also made on for the accuracies obtained for the OOA outputs and the observed effect of DEM resolution, use of colour for OOA, usability of Google Earth data and the transferability of expert based algorithm created for the training site to the validation site. It further presents results from the choice of the best data combination and the pros and cons associated with the use of the different data combinations. Also, the implementation of POF methodology for Geoeye & Lidar data combination, outputs and accuracies are presented and discussed. The chapter further goes on to present and explain the landslide causal factors for the study area with an in-depth look into the trends and explanations for the observed trends in relation to already existing knowledge of how the trends should vary with the different factors. The chapter ends with a presentation of the landslide susceptibility map obtained for the study area, the success rating of the susceptibility map and its application for the improvement of OOA work.

5. CONCLUSIONS, RECOMMENDATIONS AND LIMITATIONS

5.1. Conclusions

The purpose of this study was to evaluate the extent to which a generic algorithm that was developed for a study site in the Himalayas is transferable when applied to a geographically different area and with different data sets and to understand the landslide distribution pattern of the 2010 Haiti earthquake-induced landslides. Based on the results obtained in chapter 4, the following conclusions were made.

- The algorithm that was developed by Martha et al. [1], without modifications on the parameters and thresholds, did not work efficiently for the Haiti area with Geoeye & Lidar data. It resulted in 7.3% producer and 5.7% consumer accuracies. This was attributed to lack of robustness of this single-scaled algorithm as all thresholds were user-defined rather than data-driven and the terrain difference between the two areas. With adjustment of the parameters and their thresh holds to suit the data, land cover classes and false positives present in the Haiti training site, this algorithm worked better with improvement in accuracy for the Geoeye-Lidar data combination to 66.43 and 79.20% producer and consumer accuracies respectively. However, it was observed that it consists of many steps of individual manual parameterisation and selection of thresholds. It is based on a lot of personal judgement and no standards exist. The subjectivity and trial and error nature for selection of object features, parameters and thresholds, makes the process irreproducible, laborious and time consuming to obtain the most appropriate object features, parameters and thresholds. This was even worse when dealing with different data combinations that differ in many aspects like spatial and spectral properties as was experienced in this test study.
- With 70.11 and 69.62% producer and consumer accuracies obtained for user-defined thresholding methodology and 69.16 and 67.97% respectively for data-driven thresholding methodology, both obtained for the validation site, this study has highlighted that there is a high potential for creating a fully transferable algorithm for the Haiti region. However, for an algorithm developed for a specific site by user-defined thresholds to be effectively transferable to another site without modifications, there is need for the two sites to be geomorphologically comparable otherwise; the algorithms are rendered less effective. As has been illustrated in this study, the adopted algorithm that was originally developed for Himalayas study site didn't work efficiently in Haiti when applied without modifications. If the two sites are not comparable, the algorithm should be robust enough to accommodate a lot of variability. Site specific parameters and thresholds which may differ from one site to another should be avoided in the algorithms. In this study, there was a conflict of interest in ensuring an optimal balance between making the algorithm robust and ensuring good consumer and producer accuracies. In an effort to make a robust algorithm that could efficiently detect landslides both on the training site and the validation site there was often, a reduction in their effectiveness to accurately detect landslides extents. Though not always clear, an optimal balance of the two always needs to be found for an efficient and transferable algorithm.
- The algorithm from Geoeye-Aster data combination applied without modification on Geoeye-Lidar gave 65.75 and 61.22% producer and consumer accuracies whereas that from Google Earth aerial photo-Aster applied on Google Earth aerial photo-Lidar gave 58.31 and 60.26% producer and consumer accuracies respectively. This illustrated a possibility for an algorithm that is transferable across different DEM data sets. However, with user-defined thresholds, this is significantly limited by the individual data properties. The setting of specific thresholds is data dependent and different data have different thresholds. The use of a specific data set introduces all the pros and cons associated with the use of that specific data set which may enhance or reduce the performance of the algorithm. Also, there is a limit to which data sets a specific algorithm can be transferable to, as some data may

be incomparable in some aspects for example multispectral vs. colour information as was in the Geoeye image and Google Earth data. A lot of such limitations to algorithm transferability still exist and can only be better understood and solved through further research.

- The more standardised methodology for selection of scale factors using the Plateau Objective function and thresholding by k-means cluster analysis, did not necessarily record improvements in the accuracy of landslide detection or transferability of the algorithm. In fact, user-defined thresholding and scale factor selection recorded better consumer accuracies of 79.20 and 69.62% for the training and validation sites respectively compared to the data-driven approach which gave 62.99 and 67.97% for the training and validation sites respectively. This was probably due to better operator control with user-defined thresholding. However, it was observed to be more objective requiring fewer hard coded rules and was robust.
- For Geoeye data, use of Aster DEM gave 45.39% consumer accuracy compared to 79.20% with the Lidar DEM. This study has illustrated that with higher resolution Lidar DEM data; there is a significant improvement in consumer accuracies. It makes the process of elimination of false positives more accurate and precise. It has also been concluded that the use of such higher detailed information, though is usually more expensive, greatly enhances the quality of the outputs and so is worth the investment. Important to keep in mind, however, is that use of high resolution DEM data to create transferable algorithms will often limit the geographical extent to which these algorithms can be applied as this data often has a low areal coverage compared to low resolution data.
- From this study, it has been observed that though not as good as multi-spectral data, the use of Google Earth aerial photo data for OOA is a promising venture with a lot of potential. This is very handy for developing countries where resources to access high detailed multispectral data are limited. It gave producer and consumer accuracies of 56.30% and 69.95% compared to Geoeye's 66.43% and 79.20% respectively when used in combination with Lidar data. However, it was associated with a number of short comings like the salt and pepper effect, it was more hard to eliminate false positives and its mosaic nature which introduced errors in the process. The salt and pepper effect was attributed to the object size used in the chessboard segmentation and its very high spatial resolution.
- The Haiti earthquake triggered a large number of landslides highly concentrated along the Enriquillo Plantain fault. From the statistical analysis, combined with the sensitivity analysis, it was established that these landslides were caused by three main factors. These were lithology, slope, and the distance from the Enriquillo Plantain fault. Landslides dominated in areas within 1km from Enriquillo fault, slopes of 30-70^{o} and areas characterised by cracked and porous Middle to Upper Eocene limestone. They dominated more to the South than North of the Enriquillo fault. All the other factors incorporated in this study like distance to roads, rivers, the flow direction, elevation and aspect did not show a significant contribution to the overall pattern of the landslides. The highest landslide susceptibility is concentrated along the Enriquillo Plantain fault.
- Outputs from susceptibility analysis provide valuable information that is useable for improvement of OOA. In this study, the produced susceptibility map was very useful in elimination of false positives and improvement of consumer accuracy of the Geoeye-Aster data combination from 48.08 to 59.29%.

5.2. Research contributions

- This study has illustrated the possibility of having a fully transferable algorithm for landslide inventory creation for the Haiti area and across different data sets. Such algorithms are essential during initial disaster response phases where timely information is required.

- This study could be the pioneer of the kind of detailed analysis of the pattern of the earthquake-induced landslides for the Haiti earthquake and algorithm transferability test for the Haiti area. Thus, could be a basis for future landslide susceptibility; hazard and algorithm transferability analyses.
- This study has illustrated the possibility of use of readily available and cheap non-multispectral data for relatively quick Object-based landslide inventory production. Thus is very handy especially in least developed countries where availability of good quality imagery is limited due to lack of funds.
- It has highlighted the pros and cons associated with the use of different data for OOA and their implications on algorithm transferability. These are issues, important to understand for creation of an effectively transferable algorithm.
- This study has attempted to explain and provide insight into why the Haiti earthquake-induced landslides occurred where they did. As a result, it has made available susceptibility maps for the study area that could be useful with improvements, where deemed necessary, for both educational and incorporation in the planning activities and disaster risk management programmes.

5.3. Recommendations and further research prospects

- Subject to availability of large areal coverage of data, prospect for further research includes the application of the obtained algorithms to the entire Haiti area and use of the OOA output landslide inventory for susceptibility analysis to ascertain its accuracy in comparison to the outputs obtained when a visual landslide inventory is utilized .
- Important to note at this point is that in this study, though effort was made to maximize and balance the producer accuracy, was more aimed at efficiently illustrating the pros and cons associated with the use of different data on algorithm transferability. Thus there exists a possibility of improving these results for a specific application.
- The subjective nature of manual selection of object features, parameters and thresholds makes the whole process laborious, subjective and irreproducible. This also leads to considerable variations in both consumer and producer accuracies thus making decision making regarding the better products to use dicey. Further studies need to be done on issues concerning the optimal balancing between consumer and producer accuracies
- For all data combinations used, there was a systematic non-recognition of small and narrow shaped landslides and recognition of bare agricultural fields as landslides thus limiting the accuracy of outputs. More research could be performed to find a methodology to eliminate such false negatives and false positives. This would go a long way to improve the applicability of OOA for landslide detection and susceptibility analysis in this area.
- The use of Google Earth aerial photo data seems a promising venture for OOA related work. More research on how to make this data more useful by reducing its cons, identified in this study, is highly recommended. Pressing issues to address are mainly those related to reduction of the salt and pepper effect, and making of algorithms made for multispectral data transferable to Google Earth aerial photo data.
- Outputs from susceptibility analysis provide valuable information on the hazard situation of the study area. Incorporation of such outputs in the land use planning system with improvements, where deemed necessary, could be handy. Also, such outputs are an important tool for improvement of the OOA process.
- Subject to availability of more and better thematic and topographic data, incorporation of more factors in the susceptibility analysis for improvements is still possible.
- Detailed mapping to obtain detailed, accurate and standardized thematic and topographic data for the Haiti area would help to greatly improve analysis work related to landslide susceptibility assessment.

Such contextual data and outputs from susceptibility analysis, since they would be more accurate, could be a valuable input into the Object-based landslide detection.

5.4. Research limitations

5.4.1. Data limitations

- Most of the data obtained online from different sources lacked detailed and easily accessible metadata making it also difficult to access its quality and thus its suitability for use. This was mainly for the thematic data used.
- This study involved multi-temporal image interpretation of imagery. However, there was lack of pre-disaster imagery for some parts of the study area making the interpretation less accurate especially in assignment of attributes like landslide activity that required pre-disaster imagery.
- There was limited good quality, readily usable thematic data for Haiti especially with data like drainage lines, lithology, rivers and land use most in appropriate formats. This made the data preparation process more laborious and time consuming than expected.
- This study depended a lot on data available online from various sources. No field investigations were carried out. Lack of field knowledge was a major limitation experienced in this study. A number of deductions were made based on knowledge obtained from image interpretation which may not be necessarily accurate on ground.

5.4.2. Language barrier

- Important publications and maps like the geological map were in French, being the official language of Haiti. This made the utilization of such products inefficient as it was time consuming to translate. Also, there were possibilities of direct and mistranslations that undermine the correct understanding and usability of such data/information.

5.4.3. Limitations associated with creation of Landslide inventories

- Due to the trial and error nature of threshold determination coupled with data inaccuracies, the resultant landslide inventories from the OOA process could not have been a replica of what is on ground. Thus with use of the already inaccurate inventory from visual image interpretation to assess the accuracy of an already inaccurate inventory from OOA could have resulted in accumulation of errors in the results.
- The landslide inventory for pattern analysis was prepared by stereo image interpretation. Though efforts were made to ensure identification of all possible landslides, possible omissions and inclusions of non-landslides couldn't have been avoided totally. This can be due to a number of reasons like erosion, human interference and vegetation cover that may have obscured the landslide signatures in the imagery used.
- Also, during digitizing, errors are usually introduced due to lack of very accurate delineations of the spatial extent of landslides, making this a limitation. This could have even been made worse by both subjectivity of the image interpretation in deciding landslide and non-landslide areas and the lack of field validation to confirm the actual presence of these landslides.

5.5. Chapter summary

This chapter has highlighted some of the major observations and conclusions made from the understanding of the results obtained on of transferability of the studied algorithm and pattern analysis. It has highlighted the major contributions made by this study to the science body. A number of recommendations and research prospects have been pointed out. This chapter has also highlighted the major limitations experienced that could have had a significant impact on the progress of the study and the accuracy of the results obtained.

LIST OF REFERENCES

1. Martha, T.R., et al., *Characterising spectral, spatial and morphometric properties of landslides for semi-automatic detection using object-oriented methods.* Geomorphology, 2010. **116**(1-2): p. 24-36.
2. Ellen, R., et al., *Geotechnical Engineering Reconnaissance of the 2010 Haiti Earthquake.* 2010.
3. Martha, T.R., et al., *Segment Optimisation and Data-Driven Thresholding for Knowledge-Based Landslide Detection by Object-Oriented Image Analysis.* 2010.
4. Gallousi, C. and I.K. Koukouvelas, *Quantifying geomorphic evolution of earthquake-triggered landslides and their relation to active normal faults. An example from the Gulf of Corinth, Greece.* Tectonophysics, 2007. **440**(1-4): p. 85-104.
5. Kamp, U., et al., *GIS-based landslide susceptibility mapping for the 2005 Kashmir earthquake region.* Geomorphology, 2008. **101**(4): p. 631-642.
6. Tung-Ju Hsieh, N.T.U.o.T., *Understanding earthquakes with advanced visualization.* ACM SIGGRAPH Computer Graphics 2010 **44**(1).
7. Pareek, N., M. Sharma, and M. Arora, *Impact of seismic factors on landslide susceptibility zonation: a case study in part of Indian Himalayas.* Landslides, 2010. **7**(2): p. 191-201.
8. O'Rourke, T.D., *The Loma Prieta, California, Earthquake of October 17, 1989-Marina District.* Washington 1992, Washington United States Government Printing Office.
9. Scheidegger, A.E., *A review of recent work on mass movements on slopes and on rock falls.* Earth-Science Reviews, 1984. **21**(4): p. 225-249.
10. Olson, D.L. and D.S.D. Wu, *Earthquakes and Risk Management in China.* Human and Ecological Risk Assessment, 2010. **16**(3): p. 478-493.
11. United States Geological Survey (USGS). *Earthquake Hazards programme: Magnitude 7.0 - Haiti region.* 2010 [cited 2010 18th May]; Available from: http://earthquake.usgs.gov/earthquakes/recenteqsww/Quakes/us2010rja6.php.
12. van Westen, C.J. and T. Gorum, *Preliminary results on earthquake triggered landslides for the Haiti earthquake + poster.* In: Geophysical Research Abstracts, 12(2010) EGU2010-11153, EGU general assembly 2010. 1 p. + 1 slide., 2010.
13. Santacana, N., et al., *A GIS-Based Multivariate Statistical Analysis for Shallow Landslide Susceptibility Mapping in La Pobla de Lillet Area (Eastern Pyrenees, Spain).* Natural Hazards, 2003. **30**(3): p. 281-295.
14. Abdallah, C., et al., *Comparative use of processed satellite images in remote sensing of mass movements: Lebanon as a case study.* International Journal of Remote Sensing, 2007. **28**(19): p. 4409 - 4427.
15. Pacheco, J.A.N., *Digital Stereo Image Interpretation for Natural Hazard Assessment*, in *Thesis*. 2003, International Institute for Geo-information Science and Earth Observation: Enschede.
16. Akcay, H.G. and S. Aksoy, *Automatic detection of geospatial objects using multiple hierarchical segmentations.* Ieee Transactions on Geoscience and Remote Sensing, 2008. **46**(7): p. 2097-2111.
17. Holt, A.C., et al., *Object-based Detection and Classification of Vehicles from High-resolution Aerial Photography.* Photogrammetric Engineering and Remote Sensing, 2009. **75**(7): p. 871-880.
18. Gamanya, R., P. De Maeyer, and M. De Dapper, *Object-oriented change detection for the city of Harare, Zimbabwe.* Expert Systems with Applications, 2009. **36**(1): p. 571-588.
19. Yalcin, A., *GIS-based landslide susceptibility mapping using analytical hierarchy process and bivariate statistics in Ardesen (Turkey): Comparisons of results and confirmations.* Catena, 2008. **72**(1): p. 1-12.
20. Spillmann, T., et al., *Microseismic investigation of an unstable mountain slope in the Swiss Alps.* Journal of Geophysical Research-Solid Earth, 2007. **112**(B7).
21. Babirye, G.P., *Analysing changes in landslide vulnerability using GIS and local spatial knowledge.* 2010, University of Twente Faculty of Geo-Information and Earth Observation ITC: Enschede. p. 125.
22. The Economics and Econometrics Research Institute (EERI). *Learning from Earthquakes: The Mw 7.0 Haiti Earthquake of January 12, 2010: Report #2.* 2010, Economics and Econometrics Research Institute Brussels.
23. Wang, H.B., K. Sassa, and W.Y. Xu, *Assessment of landslide susceptibility using multivariate logistic regression: A case study in Southern Japan.* Environmental & Engineering Geoscience, 2007. **13**(2): p. 183-192.

24. Soil-Conservation-Society-of-America., *Soil conservation in Haiti.* Journal of soil and water conservation, 1946 - present. **45** p. 4 457-459.
25. Chang, K.-T., S. Wan, and T.-C. Lei, *Development of a spatial decision support system for monitoring earthquake-induced landslides based on aerial photographs and the finite element method.* International Journal of Applied Earth Observation and Geoinformation, 2010.
26. Kuriakose, S.L., G. Sankar, and C. Muraleedharan, *History of landslide susceptibility and a chorology of landslide-prone areas in the Western Ghats of Kerala, India.* Environmental Geology, 2009. **57**(7): p. 1553-1568.
27. Barlow, J., Y. Martin, and S. Franklin, *Detecting translational landslide scars using segmentation of Landsat ETM+ and DEM data in the northern Cascade Mountains, British Columbia.* Canadian journal of remote sensing, 2003. **29**(4): p. 510-517.
28. Rib, H. and T. Liang, *Recognition and identification.* Landslide Analysis and Control, 1978: p. 34–80.
29. Turner, A., G. Jayaprakash, and R. Schuster, *Landslides: Investigation and mitigation. Chapter 1-Introduction.* Vol. 247. 1996: Transportation Research Board.
30. Jin-King, L., et al., *Landslide-Enhancement images for the study of torrental-rainfall landslides.*
31. Nichol, J. and M.S. Wong, *Detection and interpretation of landslides using satellite images.* Land Degradation & Development, 2005. **16**(3): p. 243-255.
32. Ramli, M., et al., *Lineament mapping and its application in landslide hazard assessment: a review.* Bulletin of Engineering Geology and the Environment, 2010. **69**(2): p. 215-233.
33. Malamud, B., et al., *Landslide inventories and their statistical properties.* Earth Surface Processes and Landforms, 2004. **29**(6): p. 687-711.
34. Dikau, R., *Landslide recognition: identification, movement, and clauses.* 1996: Wiley.
35. Soeters, R. and C.J. van Westen, *Slope instability recognition, analysis, and zonation.* In: Landslides, investigation and mitigation / ed. by. A.K. Turner and R.L. Schuster. Washington, D.C. National Academy Press, 1996. ISBN 0-309-06151-2. (Transportation Research Board, National Research Council, Special Report ; 247) pp. 129 - 177, 1996.
36. Gómez, H. and T. Kavzoglu, *Assessment of shallow landslide susceptibility using artificial neural networks in Jabonosa River Basin, Venezuela.* Engineering Geology, 2005. **78**(1-2): p. 11-27.
37. Guzzetti, F., et al., *Comparing landslide maps: A case study in the upper Tiber River Basin, central Italy.* Environmental Management, 2000. **25**(3): p. 247-263.
38. van Westen, C.J., T.W.J. van Asch, and R. Soeters, *Landslide hazard and risk zonation - Why is it still so difficult?* Bulletin of Engineering Geology and the Environment, 2006. **65**(2): p. 167-184.
39. Harris, M.T.M., *Object - oriented method for post - event landslide mapping : the utility of texture.* 2010, University of Twente Faculty of Geo-Information and Earth Observation ITC: Enschede. p. 84.
40. Ibsen, M.L. and D. Brunsden, *The nature, use and problems of historical archives for the temporal occurrence of landslides, with specific reference to the south coast of Britain, Ventnor, Isle of Wight.* Geomorphology, 1996. **15**(3-4 SPEC. ISS.): p. 241-258.
41. Lang, A., et al., *Classic and new dating methods for assessing the temporal occurrence of mass movements.* Geomorphology, 1999. **30**(1-2): p. 33-52.
42. Glade, T., P. Albini, and F. Francés, *The use of historical data in Natural Hazard Assessments.* 2001: Springer Netherlands.
43. ICOS, *Geohazards Theme Report* S. Marsh, M. Paganini, and R. Missotten, Editors. 2003.
44. Mantovani, F., R. Soeters, and C.J. Van Westen, *Remote sensing techniques for landslide studies and hazard zonation in Europe.* Geomorphology, 1996. **15**(3-4 SPEC. ISS.): p. 213-225.
45. Metternicht, G., L. Hurni, and R. Gogu, *Remote sensing of landslides: An analysis of the potential contribution to geo-spatial systems for hazard assessment in mountainous environments.* Remote Sensing of Environment, 2005. **98**(2-3): p. 284-303.
46. van Westen, C.J., E. Castellanos, and S.L. Kuriakose, *Spatial data for landslide susceptibility, hazard, and vulnerability assessment: An overview.* Engineering Geology, 2008. **102**(3-4): p. 112-131.
47. van Westen, C.J., *Geo - information tools for landslide risk assessment : an overview of recent developments.* In: Landslides : evaluation and stabilization - glissement de terrain: Evaluation et Stabilisation : proceedings of the 9th international symposium on landslides, June 28 -July 2, 2004 Rio de Janeiro, Brazil / ed. by W. Lacerda, M. Erlich, S.A.B. Fontoura and A.S.F. Sayao. London : Balkema, 2004. ISBN: 978-0-415-35665-7. pp. 39-56, 2004.

48. Carlotto, M., *Detection and analysis of change in remotely sensed imagery with application to wide area surveillance.* Image Processing, IEEE Transactions on, 2002. **6**(1): p. 189-202.
49. Bruzzone, L. and S. Serpico, *An iterative technique for the detection of land-cover transitions in multitemporal remote-sensing images.* Geoscience and Remote Sensing, IEEE Transactions on, 2002. **35**(4): p. 858-867.
50. Wiemker, R. *An iterative spectral-spatial Bayesian labeling approach for unsupervised robust change detection on remotely sensed multispectral imagery*. 1997: Springer.
51. Bruzzone, L. and S. Serpico, *Detection of changes in remotely-sensed images by the selective use of multi-spectral information.* International Journal of Remote Sensing, 1997. **18**(18): p. 3883-3888.
52. Bruzzone, L. and D. Prieto, *An adaptive semiparametric and context-based approach to unsupervised change detection in multitemporal remote-sensing images.* Image Processing, IEEE Transactions on, 2002. **11**(4): p. 452-466.
53. Cheng, K.S., C. Wei, and S.C. Chang, *Locating landslides using multi-temporal satellite images.* Advances in Space Research, 2004. **33**(3): p. 296-301.
54. Nichol, J. and M.S. Wong, *Satellite remote sensing for detailed landslide inventories using change detection and image fusion.* International Journal of Remote Sensing, 2005. **26**(9): p. 1913-1926.
55. Liu, Y. and ... *Review of remotely sensed imagery classification patterns based on object oriented image analysis.* In: Chinese geographical science, 16(2006)3, pp. 282-288, 2006.
56. Borghuis, A., K. Chang, and H. Lee, *Comparison between automated and manual mapping of typhoon-triggered landslides from SPOT-5 imagery.* International Journal of Remote Sensing, 2007. **28**(8): p. 1843-1856.
57. Martha, T.R. and N. Kerle, *Object - oriented and cognitive detection and characterisation of landslides : abstract.* Presented at the 8th International Workshop on Remote Sensing for Disaster Management, 30 September-1 October 2010, Tokyo, Japan. 2 p., 2010.
58. Yan, G., *Pixel based and Object oriented image analysis for coal fire researcha*, in *Thesis*. 2003, International Institute for Geo-information Science and Earth Observation Enschede.
59. Esch, T., et al., *Improvement of Image Segmentation Accuracy Based on Multiscale Optimization Procedure.* Geoscience and Remote Sensing Letters, IEEE, 2008. **5**(3): p. 463-467.
60. Dragut, L., D. Tiede, and S.R. Levick, *ESP: a tool to estimate scale parameter for multiresolution image segmentation of remotely sensed data.* International Journal of Geographical Information Science, 2010. **24**(6): p. 859-871.
61. Lu, P., et al., *Object-oriented change detection for landslide rapid mapping*, in *IEEE Geoscience and remote sensing letters*.
62. Barlow, J., S. Franklin, and Y. Martin, *High spatial resolution satellite imagery, DEM derivatives, and image segmentation for the detection of mass wasting processes.* Photogrammetric Engineering and Remote Sensing, 2006. **72**(6): p. 687-692.
63. Schneevoigt, N.J., et al., *Detecting Alpine landforms from remotely sensed imagery. A pilot study in the Bavarian Alps.* Geomorphology, 2008. **93**(1-2): p. 104-119.
64. Tarantino, C., P. Blonda, and G. Pasquariello, *Remote sensed data for automatic detection of land-use changes due to human activity in support to landslide studies.* Natural Hazards, 2007. **41**(1): p. 245-267.
65. Barlow, J.a., S.b. Franklin, and Y. Martin, *High spatial resolution satellite imagery, DEM derivatives, and image segmentation for the detection of mass wasting processes.* Photogrammetric Engineering and Remote Sensing 2006. **72**(6): p. 687-692
66. Porfido, S., et al., *Areal distribution of ground effects induced by strong earthquakes in the Southern Apennines (Italy).* Surveys in Geophysics, 2002. **23**(6): p. 529-562.
67. Calais, E., et al., *Strain partitioning and fault slip rates in the northeastern Caribbean from GPS measurements.* Geophysical Research Letters, 2002. **29**(18).
68. Manaker, D.M., et al., *Interseismic Plate coupling and strain partitioning in the Northeastern Caribbean.* Geophysical Journal International, 2008. **174**(3): p. 889-903.
69. Jibson, R.W., *Predicting earthquake-induced landslide displacements using Newmark's sliding block analysis.* Transportation Research Record, 1993. **1411**: p. 9-17.
70. Ren, Z.K. and A.M. Lin, *Co-seismic landslides induced by the 2008 Wenchuan magnitude 8.0 Earthquake, as revealed by ALOS PRISM and AVNIR2 imagery data.* International Journal of Remote Sensing, 2010. **31**(13): p. 3479-3493.
71. Eberhard, M., et al., *The M W 7.0 Haiti Earthquake of January 12, 2010: USGS/EERI Advance Reconnaissance Team Report.* US Geological Survey Open-File Report, 2010: p. 1048.

72. Yagi, H., et al., *Distribution and characteristics of landslides induced by the Iwate-Miyagi Nairiku Earthquake in 2008 in Tohoku District, Northeast Japan.* Landslides, 2009. **6**(4): p. 335-344.
73. Wu, C.H. and S.C. Chen, *Determining landslide susceptibility in Central Taiwan from rainfall and six site factors using the analytical hierarchy process method.* Geomorphology, 2009. **112**(3-4): p. 190-204.
74. Malamud, B.D., et al., *Landslides, earthquakes, and erosion.* Earth and Planetary Science Letters, 2004. **229**(1-2): p. 45-59.
75. Keefer, D.K., *Investigating landslides caused by earthquakes–A historical review.* Surveys in Geophysics, 2002. **23**(6): p. 473-510.
76. Keefer, D.K., *The importance of earthquake-induced landslides to long-term slope erosion and slope-failure hazards in seismically active regions.* Geomorphology, 1994. **10**(1-4): p. 265-284.
77. The Institute of Sport and Recreation Management (ISRM). *Rock characterization testing and monitoring (ISRM suggested methods).* 1981.
78. Chigira, M., *Gravitational mass rock creep and landslides: From structural geology to hazard geology.* Memoirs of the Geological Society of Japan, 1998. **50**: p. 241-250.
79. Runqiu, H. and L. Weile, *Research on development and distribution rules of geohazards induced by Wenchuan earthquake on 12th May, 2008.* Chinese Journal of Rock Mechanics and Engineering, 2008. **27**(12): p. 2585-2592.
80. Gorum, T., et al., *Analyzing the control of the dynamic rupture processes on landslide distribution for the Wenchuan earthquake.* Presented at the expert workshop on assessing the state of art of landslide hazard and risk assessment in China, 13-14 April 2010, Chengdu, China. 14 slides., 2010.
81. van Westen, C.J., T. Gorum, and X.M. Fan, *Distribution pattern of earthquake - induced landslides triggered by the 12 May 2008 Wenchuan earthquake : abstract.* In: Geophysical Research Abstracts, 12(2010) : European Geosciences Union General Assembly 2010, 2-7 May 2010, Vienna, Austria. 1 p., 2010.
82. Norini, G., et al., *Large scale landslides triggered by Quaternary tectonics in the Acambay graben, Mexico.* Earth Surface Processes and Landforms, 2010. **35**(12): p. 1445-1455.
83. Zhou, C.H., et al., *On the spatial relationship between landslides and causative factors on Lantau Island, Hong Kong.* Geomorphology, 2002. **43**(3-4): p. 197-207.
84. Bednarik, M., et al., *Landslide susceptibility assessment of the Kralovany-Liptovský Mikulás railway case study.* Physics and Chemistry of the Earth, Parts A/B/C, 2010. **35**(3-5): p. 162-171.
85. Dahal, R.K., et al., *Predictive modelling of rainfall-induced landslide hazard in the Lesser Himalaya of Nepal based on weights-of-evidence.* Geomorphology, 2008. **102**(3-4): p. 496-510.
86. Franks, C.A.M., *Characteristics of some rainfall-induced landslides on natural slopes, Lantau Island, Hong Kong.* Quarterly Journal of Engineering Geology and Hydrogeology, 1999. **32**(3): p. 247-259.
87. Neaupane, K.M. and M. Piantanakulchai, *Analytic network process model for landslide hazard zonation.* Engineering Geology, 2006. **85**(3-4): p. 281-294.
88. Nilaweera, N. and P. Nutalaya, *Role of tree roots in slope stabilization.* Bulletin of Engineering Geology and the Environment 2004. **57**(4): p. 337-342.
89. Pradhan, B. and S. Lee, *Landslide susceptibility assessment and factor effect analysis: backpropagation artificial neural networks and their comparison with frequency ratio and bivariate logistic regression modelling.* Environmental Modelling & Software, 2010. **25**(6): p. 747-759.
90. Akgun, A., S. Dag, and F. Bulut, *Landslide susceptibility mapping for a landslide-prone area (Findikli, NE of Turkey) by likelihood-frequency ratio and weighted linear combination models.* Environmental Geology, 2008. **54**(6): p. 1127-1143.
91. Roth, R., *Factors affecting landslide-susceptibility in San Mateo county, California.* Bulletine of the Association of Engineering Geologists, 1983. **20**(4): p. 353-372.
92. Çevik, E. and T. Topal, *GIS-based landslide susceptibility mapping for a problematic segment of the natural gas pipeline, Hendek (Turkey).* Environmental Geology, 2003. **44**(8): p. 949-962.
93. Nandi, A. and A. Shakoor, *A GIS-based landslide susceptibility evaluation using bivariate and multivariate statistical analyses.* Engineering Geology, 2010. **110**(1-2): p. 11-20.
94. Regmi, N.R., J.R. Giardino, and J.D. Vitek, *Assessing susceptibility to landslides: Using models to understand observed changes in slopes.* Geomorphology, 2010. **122**(1-2): p. 25-38.
95. Barredo, J., et al., *Comparing heuristic landslide hazard assessment techniques using GIS in the Tirajana basin, Gran Canaria Island, Spain.* International Journal of Applied Earth Observation and Geoinformation, 2000. **2**(1): p. 9-23.

96. Soeters, R. and C. Van Westen, *Slope instability recognition, analysis, and zonation.* Landslides Investigation and Mitigation, 1996: p. 129–177.
97. Dwi Wahono, B.F., *Applications of statistical and heuristic methods for landslide susceptibility assessments : a case study in Wadas Lintang sub district, Wonosobo regency, central Java province, Indonesia.* 2010, University of Twente Faculty of Geo-Information and Earth Observation ITC: Enschede. p. 106.
98. Quinn, P.E., et al., *Regional-scale landslide susceptibility mapping using the weights of evidence method: an example applied to linear infrastructure.* Canadian Geotechnical Journal, 2010. **47**(8): p. 905-927.
99. Nichol, J.E., A. Shaker, and M.-S. Wong, *Application of high-resolution stereo satellite images to detailed landslide hazard assessment.* Geomorphology, 2006. **76**(1-2): p. 68-75.
100. Castellanos Abella, E.A., et al., *Multi - scale landslide risk assessment in Cuba*, in *ITC Dissertation;154*. 2008, ITC
University of Utrecht: Enschede
Utrecht. p. 272.
101. Westen, C.J.V., N. Rengers, and R. Soeter, *Use of Geomorphological Information in Indirect Landslide Susceptibility Assessment.* Natural Hazards, 2003. **volume 30**(3): p. 399-419.
102. van Westen, C.J., N. Rengers, and R. Soeters, *Use of geomorphological information in indirect landslide susceptibility assessment.* Natural hazards : journal of the international society for the prevention and mitigation of natural hazards, 2003. **30**(3): p. + one map.
103. Impact Forecasting LLC., *Event Recap Report:1/12/10 Haiti Earthquake.* 2010: Chicago.
104. Hadden, R.L. and S.G. Minson. *The Geology of Haiti: An Annotated Bibliography of Haiti's Geology, Geography and Earth Science.* 2010 [cited 2010 17th November 2010]; Available from: http://www.dtic.mil/cgi-bin/GetTRDoc?AD=ADA528274&Location=U2&doc=GetTRDoc.pdf.
105. ASTER GDEM Validation Team., et al., *ASTER Global DEM Validation Summary Report.* 2009.
106. Giles, P.T. and S.E. Franklin, *Comparison of derivative topographic surfaces of a DEM generated from stereoscopic SPOT images with field measurements.* Photogrammetric Engineering and Remote Sensing, 1996. **62**(10): p. 1165-1170.
107. Tokunaga, M., et al., *Overview of DEM product generated by using ASTER data.* International Archives of Photogrammetry and Remote Sensing, 1996. **31**: p. 874-878.
108. Hirano, A., R. Welch, and H. Lang, *Mapping from ASTER stereo image data: DEM validation and accuracy assessment.* ISPRS Journal of Photogrammetry and Remote Sensing, 2003. **57**(5-6): p. 356-370.
109. Fugro EarthData. *Lidar mapping.* 2010 [cited 2011 15th February 2011]; Available from: http://www.fugroearthdata.com/servicessubcat.php?subcat=lidar-mapping.
110. Moore-Cooks, K., *Accuracy Assessment of LIDAR Data.*
111. Flood, M. and J. Satalich, *LiDAR 101.* Point of Beginning, 2001
112. Evansa, G.A., et al., *An Accuracy Assessment of Cartosat-1 Stereo Image Data-Derived Digital Elevation Models: A Case Study of the Drum Mountains, Utah.* the International Archives of the Photogrammetry, Remote Sensing and Spatial Information Sciences, Beijing, 2008.
113. Hovius, N., C. Stark, and P. Allen, *Sediment flux from a mountain belt derived by landslide mapping.* Geology, 1997. **25**(3): p. 231.
114. van Westen, C.J., *Application of geographic information systems to landslide hazard zonation*, in *ITC Dissertation;13*. 1993, ITC: Enschede. p. 245.
115. Espindola, G., et al., *Parameter selection for region-growing image segmentation algorithms using spatial autocorrelation.* International Journal of Remote Sensing, 2006. **27**(14): p. 3035-3040.
116. Congalton, R.G., *A review of assessing the accuracy of classifications of remotely sensed data.* Remote Sensing of Environment, 1991. **37**(1): p. 35-46.
117. Bonham-Carter, G., *Geographic information systems for geoscientists: modelling with GIS.* 1994: Pergamon Pr.
118. Guzzetti, F., et al., *Power-law correlations of landslide areas in central Italy.* Earth and Planetary Science Letters, 2002. **195**(3-4): p. 169-183.
119. Dussauge-Peisser, C., et al., *Probabilistic approach to rock fall hazard assessment: potential of historical data analysis.* 2002.
120. Dussauge, C., J. Grasso, and A. Helmstetter, *Statistical analysis of rockfall volume distributions: implications for rockfall dynamics.* 2003.
121. Dai, F.C. and C.F. Lee, *Frequency-volume relation and prediction of rainfall-induced landslides.* Engineering Geology, 2001. **59**(3-4): p. 253-266.

122. Guzzetti, F., et al., *Probabilistic landslide hazard assessment at the basin scale.* Geomorphology, 2005. **72**(1-4): p. 272-299.
123. Pelletier, J.D., et al., *Scale-invariance of soil moisture variability and its implications for the frequency-size distribution of landslides.* Engineering Geology, 1997. **48**(3-4): p. 255-268.
124. Corominas, J. and J. Moya, *A review of assessing landslide frequency for hazard zoning purposes.* Engineering Geology, 2008. **102**(3-4): p. 193-213.
125. Liu, D. and F. Xia, *Assessing object-based classification: advantages and limitations.* Remote Sensing Letters, 2010. **1**(4): p. 187-194.
126. Haralick, R., K. Shanmugam, and I. Dinstein, *Textural features for image classification.* IEEE Transactions on systems, man and cybernetics, 1973. **3**(6): p. 610-621.
127. Maurrasse, F., *Survey of the geology of Haiti.* Miami Geol. Sot., Miami, 1982.
128. Thomas, N., C. Hendrix, and R. Congalton, *A comparison of urban mapping methods using high-resolution digital imagery.* Photogrammetric Engineering and Remote Sensing, 2003. **69**(9): p. 963-972.
129. Zhang, Y., *Texture-integrated classification of urban treed areas in high-resolution color-infrared imagery.* Photogrammetric Engineering and Remote Sensing, 2001. **67**(12): p. 1359-1366.
130. Carleer, A., O. Debeir, and E. Wolff, *Assessment of very high spatial resolution satellite image segmentations.* Photogrammetric Engineering and Remote Sensing, 2005. **71**(11): p. 1285-1294.
131. Lisle, R.J., *Google Earth: a new geological resource.* Geology Today, 2006. **22**(1): p. 29-32.
132. Bardossy, G. and J. Fodor, *Uncertanities and risk in geological activities and new ways of their handling.* Mining-Geological-Petroleum Engineering Bulletin, 2001. **13**(1): p. 15-24.
133. Fodor, J. and G. Bárdossy, *Uncertainty and Risk: Mathematical Concepts and some Geological Applications.*
134. Beck, A., *Google Earth and World Wind: remote sensing for the masses.* Antiquity, 2006. **80**: p. 308.
135. Cheng, Q., F.P. Agterberg, and S.B. Ballantyne, *The separation of geochemical anomalies from background by fractal methods.* Journal of Geochemical Exploration, 1994. **51**(2): p. 109-130.
136. Dai, F.C., et al., *Assessment of landslide susceptibility on the natural terrain of Lantau Island, Hong Kong.* Environmental Geology, 2001. **40**(3): p. 381-391.
137. Süzen, M.L. and V. Doyuran, *Data driven bivariate landslide susceptibility assessment using geographical information systems: A method and application to Asarsuyu catchment, Turkey.* Engineering Geology, 2004. **71**(3-4): p. 303-321.
138. Dai, F.C. and C.F. Lee, *Landslide characteristics and slope instability modeling using GIS, Lantau Island, Hong Kong.* Geomorphology, 2002. **42**(3-4): p. 213-228.
139. Prentice, C.S., et al., *Seismic hazard of the Enriquillo-Plantain Garden fault in Haiti inferred from palaeoseismology.* Nature Geosci, 2010. **3**(11): p. 789-793.
140. Hayes, G., et al., *Complex rupture during the 12 January 2010 Haiti earthquake.* Nature Geoscience, 2010. **3**(11): p. 800-805.
141. Calais, E., et al., *Transpressional rupture of an unmapped fault during the 2010 Haiti earthquake.* Nature Geoscience, 2010. **3**(11): p. 794-799.
142. Dahal, R., et al., *GIS-based weights-of-evidence modelling of rainfall-induced landslides in small catchments for landslide susceptibility mapping.* Environmental Geology, 2008. **54**(2): p. 311-324.

APPENDICES

APPENDIX A: Image characteristics of mass movement types and subtypes

Morphological, vegetational and drainage diagnostics used			
	Morphology	**Vegetation**	**Drainage**
Translational slides	Joint controlled crown in rockslides, smooth planar surface, relatively shallow, run-out hummocky rather than chaotic relief with block size decreasing with larger distance	Source and transport path denudated often with lineations in transport direction, differential vegetation in body	Absence of ponding below the crown, disordered or absence of surface drainage on the body, Deflected or blocked by frontal lobe
Rotational slides	Abrupt changes in slope morphology, concave niches and concave run-out lobe forms, back tilting slope facets, scarps and hummocky morphology on depositional parts	Clear vegetation contrast with surroundings, absence of landuses indicative of activity, differential vegetation according to drainage	Bad surface drainage or ponding in back tilting slopes niches, seepage in frontal part of run-out lobe
Debris avalanches	Relatively small, shallow niches on steep slopes($>35^{o}$) with clear linear path, body frequently absent	Niche and path are denudated or covered by secondary vegetation.	Shallow linear gully can originate on the path of the debris avalanche
Lateral spread	Irregular arrangement of large blocks which are tilting in various directions, large cracks and linear depressions are separating the blocks, movement cant originate on gentle slopes($<10^{o}$)	Differential vegetation is enhancing the separation of blocks. Considerable contrast with unaffected areas	Disrupted surface drainage, front part of movement is closing off a valley, causing obstruction and asymmetrical valley profile
Debris Flow	Complete destruction along path, depositional levees, fattish desolated plain, exhibiting vague flow structures, large amount of small concavities	Absence of vegetation everywhere	Deranged on body while original streams are blocked or deflected by the body

Table 23: Image characteristics of mass movement types and subtypes

Adapted from van Westen et al. [114]

APPENDIX B: Original Factor parameter maps

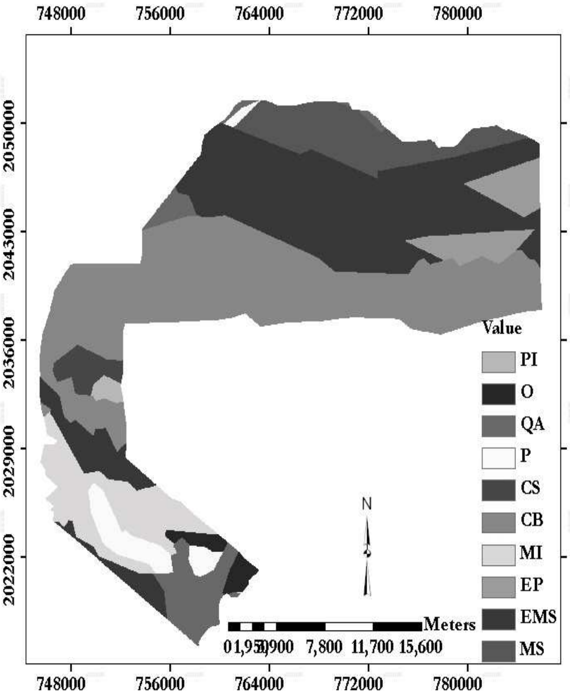

Figure 37: Lithology Map

The codes used in Figure 37 are explained in Table 27

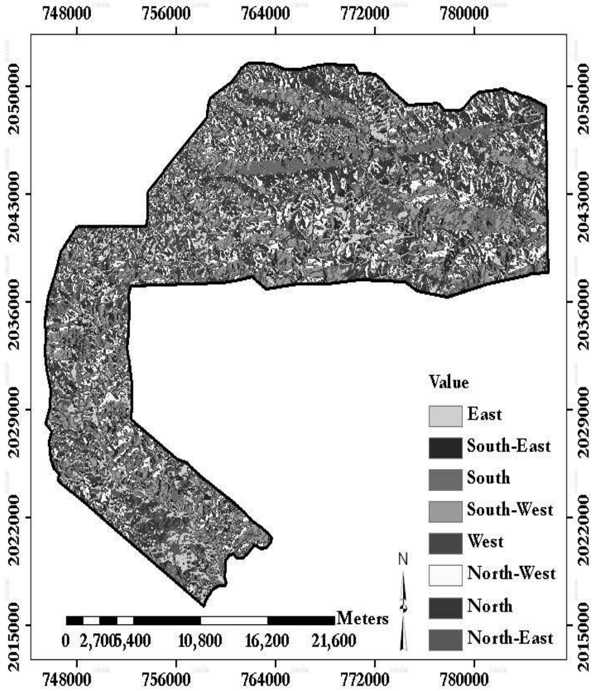

Figure 38: Flow direction map

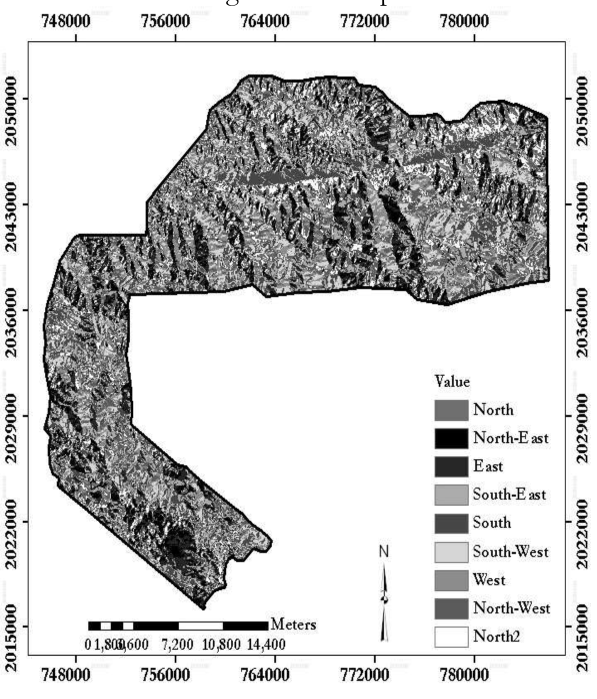

Figure 39: Aspect Map

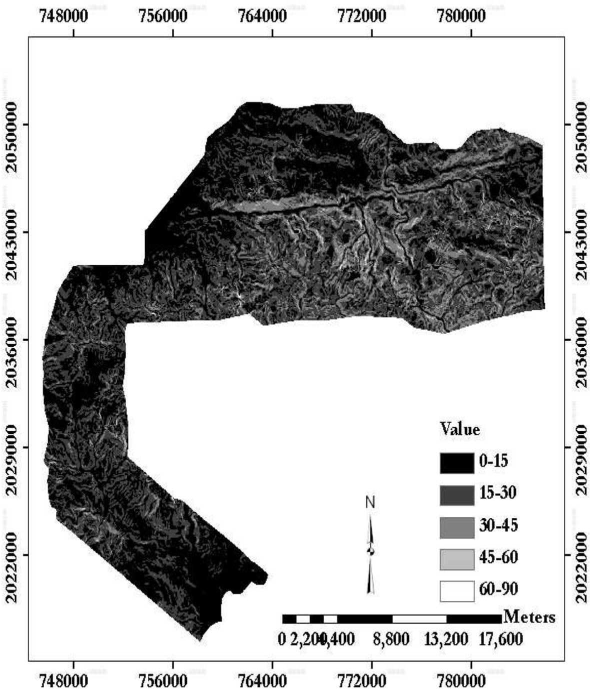

Figure 40: Slope map

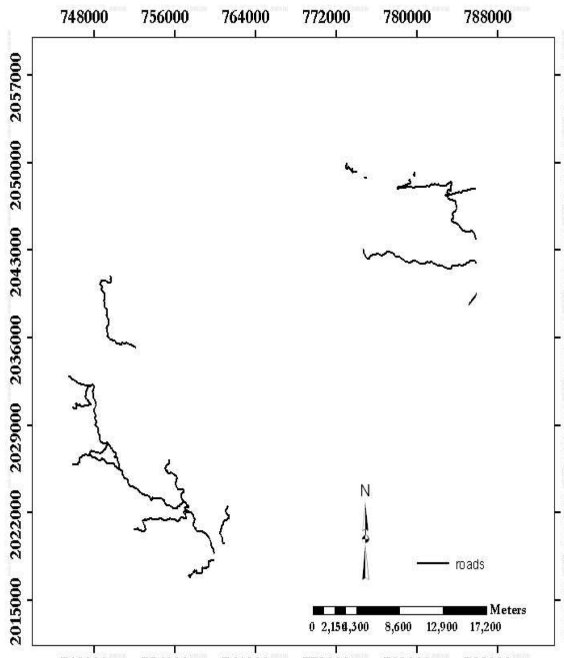

Figure 41: Roads Map

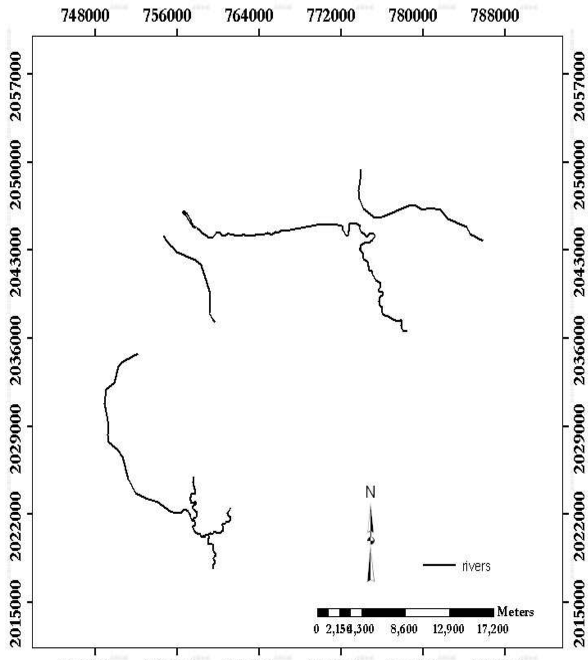

Figure 42: Rivers Map

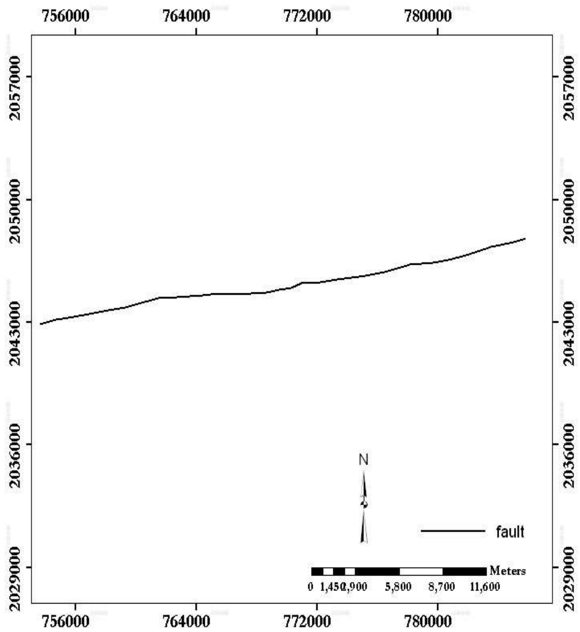

Figure 43: Enriquillo-Plantain Fault Map

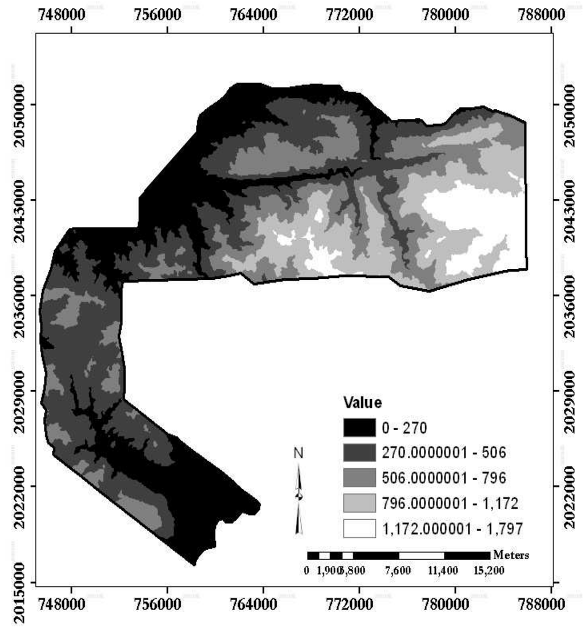

Figure 44: Elevation Map

APPENDIX C: Scripts for susceptibility analysis

// Script for weights
// make cross table
del %1_active*.* -force
Del W%1*.* -force
Del %1.tbt -force
crtbl %1 %1
%1_active.tbt = TableCross(%1,active,IgnoreUndefs)
calc %1_active.tbt
//calculation in cross table
Tabcalc %1_active.tbt npixact:=iff(active=1,npix,0)
tabcalc %1 nclass = ColumnJoinSum(%1_active.tbt,NPix,%1,1)
tabcalc %1 nslclass := ColumnJoinSum(%1_active.tbt,npixact, %1,1)
tabcalc %1 nmap := ColumnJoinSum(%1_active.tbt,NPix,,1)
tabcalc %1 nslide := ColumnJoinSum(%1_active.tbt,npixact,,1)
//calculate Npix1 to Npix 4
Tabcalc %1 Npix1 = iff(nslclass=0,1,nslclass)
Tabcalc %1 Npix2 = iff((nslide - nslclass)=0,1,nslide-nslclass)
Tabcalc %1 Npix3 = nclass - nslclass
Tabcalc %1 Npix4 = nmap - nslide - nclass + nslclass
// calculate weights
Tabcalc %1 Wplus=ln((npix1*(npix3+npix4))/((npix1+npix2)*npix3))
Tabcalc %1 Wmin=ln((npix2*(npix3+npix4))/((npix1+npix2)*npix4))
Tabcalc %1 wmintotal = ColumnAggregateSum(Wmin,,1)
Tabcalc %1 Wfinal:=Wplus+Wmintotal-Wmin
//create the attribute map
W1%1.mpr := MapAttribute(%1,%1.tbt.Wfinal)
W%1.mpr := iff(isundef(outline),?,W1%1.mpr)
del W1%1*.* -force
Show W%1.mpr
	// Cross Weight Map with Map: active
	//%1 is weighted factor maps
	del success*.* -force
	crtbl %1 %1
	%1_active.tbt = TableCross(%1,active,IgnoreUndefs)
	calc %1_active.tbt
	//In the cross table, calculate
	tabcalc %1_active npixact:=iff(active=1,npix,0)
	tabcalc %1_active Npcumactive = ColumnCumulative(npixact)
	//determine the maximum value with landslide pixels.
	tabcalc %1_active Maxlandslide =
	ColumnAggregateMax(Npcumactive,,1)
	calculate percentage of landslides
	tabcalc %1_active percentage:=100*(Npcumactive /maxlandslide)
	tabcalc %1_active Percentlandslide:=100-percentage
	tabcalc %1_active Npixcum:=ColumnCumulative(NPix)
	tabcalc %1_active NpixCumMax := ColumnAggregateMax(Npixcum,,1)
	tabcalc %1_active reverse := NpixCumMax-npixcum
	tabcalc %1_active percentmap := 100*(reverse/NpixCumMax)
	//calc %1_active.tbt
	open %1_active.tbt
	//graph
	open %1_active.grh

Script for weighting of the factor maps	**Script for success rating.**

Table 24: Scripts for weighting and success rating of factor maps

APPENDIX D: Statistics derived from WoE modeling for each factor class

Factor	Factor classes	Final weights	Contrast	Factor	Factor classes	Final weights	Contrast
Lithology	PI	-3.12	-2.74	South of Enriquillo Plantain Fault	>6750-7000	-3.62	-3.58
	QA	-1.61	-1.23		>7000-7250	-3.51	-3.47
	CB	-2.90	-2.52		>7250-7500	-3.31	-3.28
	EMS	1.29	1.67		>7500-7750	-3.19	-3.16
	MI	-1.05	-0.67		>7750-8000	-1.77	-1.73
	MS	-0.22	0.16		>8000-8250	-2.42	-2.39
	O	-2.97	-2.59		>8250-8500	-3.06	-3.02
	EP	0.24	0.62		>8500-8750	-3.08	-3.05
	P	-1.66	-1.27		>8750-9000	-3.01	-2.98
	CS	-4.32	-3.94		>9000-9250	-2.96	-2.93
Flow direction	E	0.59	0.60		>9250-9500	-2.55	-2.52
	N	0.30	0.31		>9500-9750	-2.16	-2.13
	NE	-0.23	-0.22		>9750-10000	-2.14	-2.10
	NW	-0.05	-0.05		>10000-10250	-2.14	-2.10
	S	0.04	0.05		>10250-10500	-2.14	-2.11
	SE	-0.30	-0.29		>10500-10750	-2.14	-2.11
	SW	-0.71	-0.71		>10750-11000	-2.16	-2.13
	W	-0.11	-0.10		>11000-11500	-2.82	-2.79
Distance from roads	0-10	-0.12	0.18		>11500-12000	-2.82	-2.78
	>10-20	-	-		>12000-12500	-2.83	-2.79
	>20-30	-0.37	-0.07		>12500-13000	-0.75	-0.72
	>30-50	-0.70	-0.41		>13000-13500	-2.84	-2.80
	>50-100	-0.75	-0.46		>13500-14000	-2.83	-2.79
	>100-200	-0.72	-0.43		>14000-14500	-2.80	-2.77
	>200-11000	0.04	0.33		>14500-15000	-1.51	-1.48
Slope	0-15	-1.18	-1.26		>15000-15500	-3.00	-2.96
	>15-30	-0.26	-0.34		>15500-16000	-2.37	-2.34
	>30-45	1.56	1.48		>16000-16500	-1.53	-1.49
	>45-60	2.54	2.46		>16500-17000	0.59	0.63
	>60-75	2.55	2.47		>17000-17500	0.25	0.28
	>75-90	-	-		>17500-18000	-0.77	-0.73
Aspect	N	-0.09	-0.08		>18000-18500	-2.01	-1.98
	NE	0.12	0.13		>18500-19000	-1.35	-1.32
	E	0.24	0.25		>19000-20000	-0.90	-0.87
	SE	0.03	0.04		>20000-21000	-2.05	-2.02
	S	0.58	0.59		>21000-22000	-4.11	-4.07
	SW	-0.12	-0.11		>22000-23000	-2.83	-2.80
	W	-0.06	-0.06		>23000-24000	-2.30	-2.26
	NW	-0.78	-0.77		>24000-25000	-3.03	-2.99
	N2	-0.42	-0.41		>25000-26000	-2.49	-2.45
Distance from drainage	0-10	0.41	-0.12		>26000-26515	-0.16	-0.13
	>10-20	-	-		0-250	1.12	1.16

lines/rivers	**>20-30**	0.50	-0.02		**North of Enriquillo Plantain Fault**	**>250-500**	1.73	1.77
	>30-50	0.37	-0.16			**>500-750**	1.82	1.85
	>50-100	1.02	0.50			**>750-1000**	1.27	1.31
	>100-200	1.42	0.90			**>1000-1250**	0.47	0.51
	>200	-0.11	-0.63			**>1250-1500**	1.26	1.30
Elevation	**0-200**	-0.19	-0.18			**>1500-1750**	0.89	0.92
	>200-400	0.34	0.36			**>1750-2000**	1.13	1.16
	>400-600	-0.25	-0.24			**>2000-2500**	0.65	0.68
	>600-800	0.11	0.12			**>2500-3000**	1.10	1.14
	>800-1000	-0.17	-0.16			**>3000-3250**	-1.07	-1.03
	>1000-1200	-0.51	-0.49			**>3250-3500**	-3.30	-3.26
	>1200-1400	0.50	0.51			**>3500-3750**	0.15	0.20
	>11400-600	0.00	0.02			**>3750-4000**	0.28	0.33
	>1600-1800	-3.03	-3.02			**>4000-4250**	-0.97	-0.92
	>1800-2000	-	-			**>4250-4500**	0.96	1.01
South of Enriquillo Plantain Fault	**0-250**	1.12	1.16			**>4500-4750**	0.50	0.55
	>250-500	1.73	1.77			**>4750-5000**	-1.50	-1.45
	>500-750	1.82	1.85			**>5000-5250**	-0.42	-0.37
	>750-1000	1.27	1.31			**>5250-5500**	-2.33	-2.28
	>1000-1250	0.47	0.51			**>5500-5750**	0.13	0.18
	>1250-1500	1.26	1.30			**>5750-6000**	0.02	0.06
	>1500-1750	0.89	0.92			**>6000-6250**	-2.74	-2.70
	>1750-2000	1.13	1.16			**>6250-6500**	-2.39	-2.34
	>2000-2500	0.65	0.68			**>6500-6750**	-1.64	-1.60
	>2500-3000	1.10	1.14			**>6750-7000**	-0.37	-0.32
	>3000-3250	0.03	0.07					
	>3250-3500	0.28	0.31					
	>3500-3750	-0.29	-0.26					
	>3750-4000	0.15	0.19					
	>4000-4250	-0.38	-0.34					
	>4250-4500	0.34	0.38					
	>4500-4750	-0.54	-0.51					
	>4750-5000	-2.76	-2.73					
	>5000-5250	0.48	0.52					
	>5250-5500	-0.37	-0.33					
	>5500-5750	-2.49	-2.46					
	>5750-6000	-3.77	-3.74					
	>6000-6250	-3.77	-3.74					
	>6250-6500	-3.67	-3.63					
	>6500-6750	-3.63	-3.60					

Table 25: Statistics derived from WoE modelling for each factor class

APPENDIX E: Lithology map translation done in Google translate

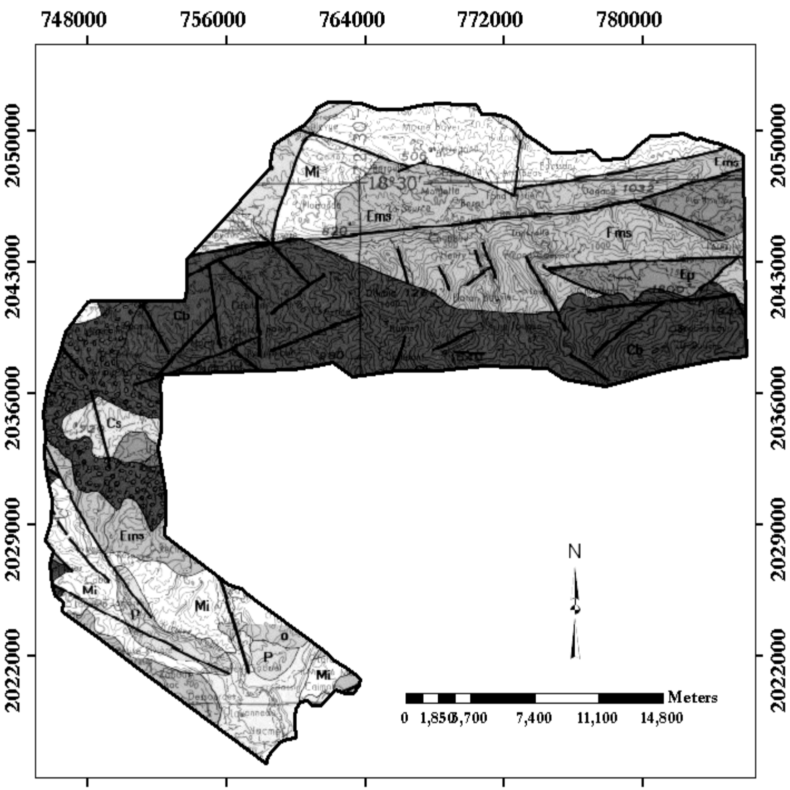

:t al

French legend descriptions		
Sedimentary rocks		
QA	Quaternary	Alluvial,cones depandages fluviates, eboulis, mangroves
P	Tertiary	Marnes et sables, vieux cones d epandages: marnes et sables du plateau central et du gros morne.
MS		Marnes a orbulines: marnes et sables du plateau central et du Bassin de Gros Morne
EMS		Biomicrites pelagiques de la presqu ile du Sud et du versant Sud du Massif du Nord: ailleurs, calcaires de plate-forme du Massif du Nord
O		Craies et calcaires marneux de la presqu ile du Sud et de la Chaine des Matheux; argiles et gres du Bassin de Gros Morne; calcaires grossiers et conglomerates
EP		Conglomerates et gres volcanogenes du massif de la Selle ; marnes, gres et calcaires marneux des Montagnes Noires;ailleurs, calcaires de plate-forme et calcaires pelagiques
MI		Flysch greso-pelitique du Plateau Central(fm. Madame Joie); gres calcareux du Bassin de Gros Morne(fm. La Crete); calcaires de la plate-forme du chainon de Paincroix et de la presqu ile du Sud
CS		Calcaires pelagiques de la presqu ile du Sud(fm. Macaya) et du Massif de Terre Neuve(fm. Miguinda), et autres calcaires du meme age
PI	Cretaceous and Tertiary	Marnes et calcaires marneux du massif de la selle(fm.Beloc); argiles et roches volcano detritiques du Massif de la Hotte(fm. Riviere Glace); ailleurs, calcaires pelagiques de la Presqu'ile du Sud
Magmatic rocks		
CB	Cretaceous	Complex tholeitique et sedimentaire de presqu ile du Sud(fm. Demisseau) et autres coulees massives, avec ou sans intercalations sedimentaires

Table 26: French Legend of the original lithology map

Abbreviation		English Interpretation of the descriptions	Lithology identified
Sedimentary rocks			
QA	Quaternary	Alluvial cones of Spraying fluviates, scree, mangroves	Quaternary alluviums
P	Tertiary	**Pliocene:** Marls and sands, old cones of spreading: marls and sands of the central plateau and the big hill.	Pliocene weakly cemented clastic deposits in fans and low hills
MS		**Upper Miocene:** marls orbulines: marls and sands of the Central Plateau and Basin "Gros Morne"	Upper Miocene age limestone, marls and sandstone
EMS		**Middle to Upper Eocene:** Biomicrites pelagic of the peninsula South Island and southern slopes of the Massif du Nord also limestone platform of the Massif du Nord	Middle to Upper Eocene limestone: (cracked and porous carbonate aquifers highly permeable)
O		**Oligocene:** Chalk and marly limestone of the peninsula South Island and the "Chaine des Matheux", clays and sandstones Basin Gros Morne, coarse limestone and conglomerates	Oligocene chalk and marly limestone(cracked and uneven carbonate aquifers partition)
EP		**Upper Paleocene - Lower to Middle Eocene:** conglomerates and sandstones of volcanic massif de la Selle, marl, sandstone and calcareous marl of the Black Mountains, elsewhere platform lime stones and calcareous pelagic	Upper Paleocene - Lower to Middle Eocene volcaniclastic rocks
MI		**Lower Miocene:** Sandstone-pelitic flysch Central Plateau (fm. Ms. Joy) calcareous sandstone Basin "Gros Morne" (fm. La Crete) lime stones of the platform chainon Paincroix of the peninsula and South Island	Lower Miocene flysch lime stones (marly limestone aquifers)
CS		**Senonian:** pelagic lime stones of the peninsula South Island (fm. Macaya) and the Massif de Terre Neuve (fm. Miguinda), and other lime stones of the same age	Senonian pelagic limestone
PI	Cretaceous and Tertiary	Marls and marly limestone massif of the saddle (fm.Beloc) clays and detrital volcano of the Massif de la Hotte (fm. Riviere Glace) also pelagic limestone of the southern peninsula	Maastrichtian Pelagic limestone
Magmatic rocks			
CB	Cretaceous	**Tholeiitic and sedimentary complex:** Tholeiitic and sedimentary complex of the South Island peninsula (fm. Demisseau) and other massive flows, with or without interbedded sedimentary	Cretaceous metamorphosed basalt, ultramafic rocks(igneous & basaltic) volcano-sedimentary metamorphic rocks

Table 27: Lithological map translation and interpretation to usable Lithology map units

APPENDIX F: Methodological set up used by Martha et al. [1]

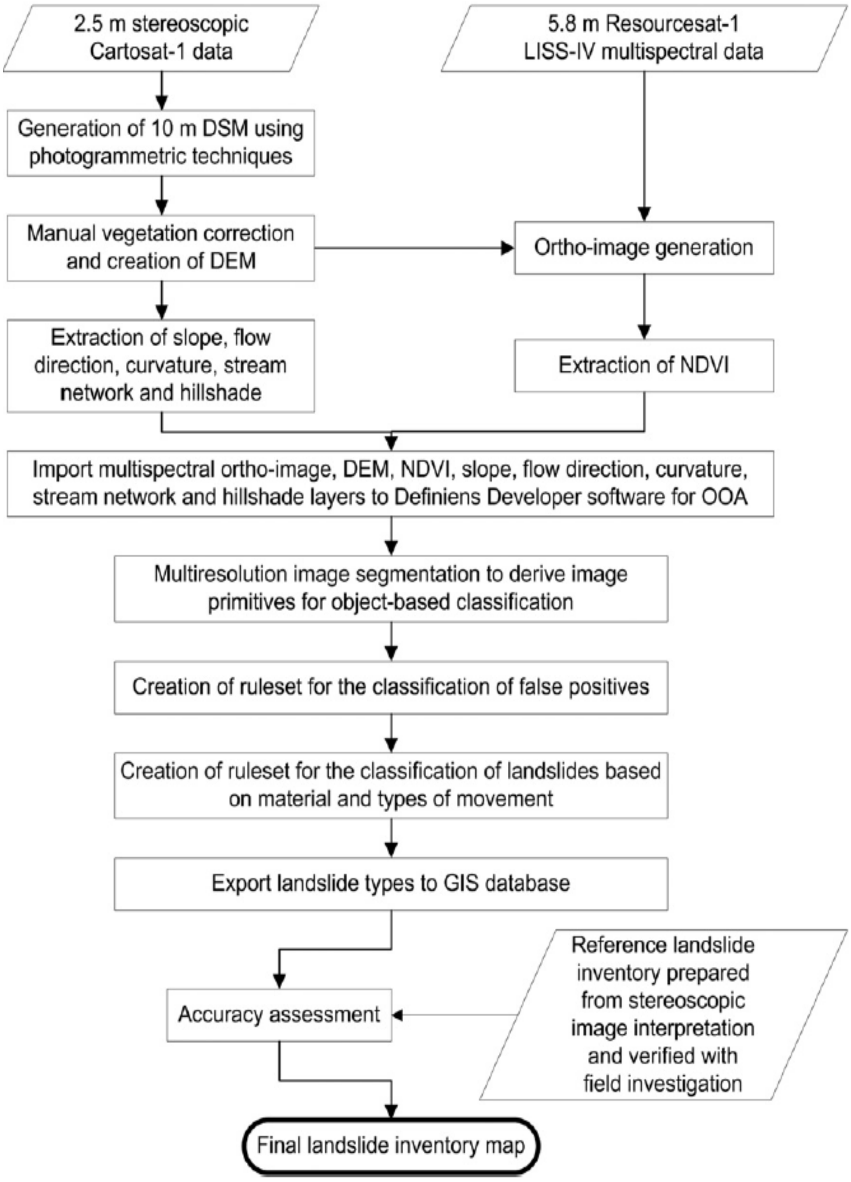

Figure 46: Methodological set up used by Martha et al. [1]

APPENDIX G: Quantitative classification criteria for landslide types.

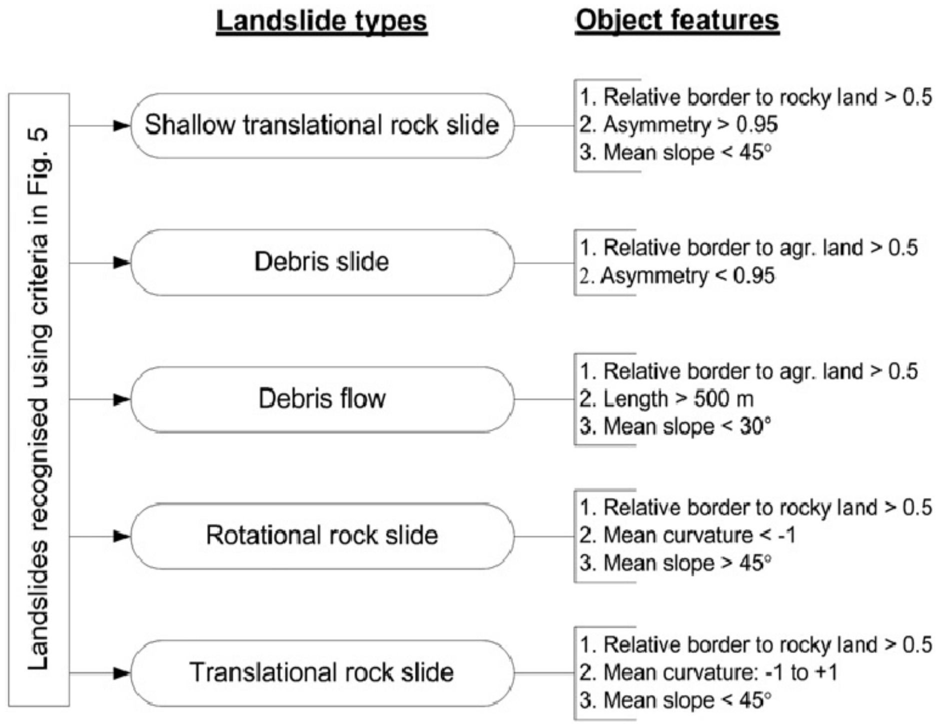

Figure 47: Quantitative classification criteria for landslide types.

Adopted from Martha et al [1]